Spin Seebeck Effect Experiments

Niklas Roschewsky

Master Thesis

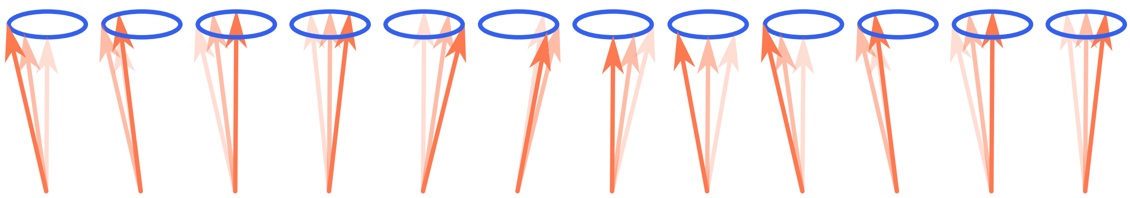

Technical University Munich

Walther-Meißner-Institute for Low Temperature Research
Bavarian Academy of Sciences and Humanities

Spin Seebeck Effect Experiments

Niklas Roschewsky

Master Thesis

First referee:	PD. Dr. Sebastian T. B. Goennenwein
Second referee:	Prof. Dr. Martin S. Brandt
Thesis period:	18^{th} March 2013 until 18^{th} March 2014

Contents

List of Figures

Immer, immer wieder, für immer, für immer & dich.

Jümmers

1 Introduction

Thermoelectric effects describe the interplay of heat- and charge currents [9]. One example is the (conventional) Seebeck effect [86]. Here, a temperature difference is converted into an electric potential [32]. However, heat currents can also interact with the intrinsic angular momentum ("spin") of electrons [42, 87]. These phenomena are investigated in the research field of spin caloritonics [9, 31]. The spin Seebeck effect is the spin analogy to the conventional Seebeck effect. It describes the generation of an electromotive force in a paramagnetic metal, attached to a ferromagnet, by a temperature gradient [9, 106].
The spin Seebeck effect attracted a lot of attention due to possible applications, allowing to convert thermal energy into electric energy with high efficiency. A suggested application of the spin Seebeck effect is the so called spin-thermoelectric coating [50]. This is a thin film structure, which utilizes the spin Seebeck effect for power generation. The spin-thermoelecrtic coating has significant advantage over the conventional Seebeck effect, since it provides easy scaling possibilities.
Nevertheless, the spin Seebeck effect is still a highly controversial topic. In literature, many contradicting results have been published [81, 83, 94, 96, 98, 106]. In the following we will outline some key discoveries that constitute our understanding of the spin Seebeck effect today. In addition, a number of recent publications on the SSE will be presented.

In 2008 Uchida *et al.* [96] observed a magnetization orientation dependent thermovoltage in platinum stripes, which had been deposited on the ferromagnetic metal permalloy. For the measurements, the so called transversal configuration was used, in which the applied thermal gradient is parallel to the interface between the platinum and the permalloy (*cf.* Fig. 1.1).
This was called "spin Seebeck effect" by Uchida *et al.* as it was assumed that, in close analogy to the well known "conventional Seebeck effect", the observed voltage

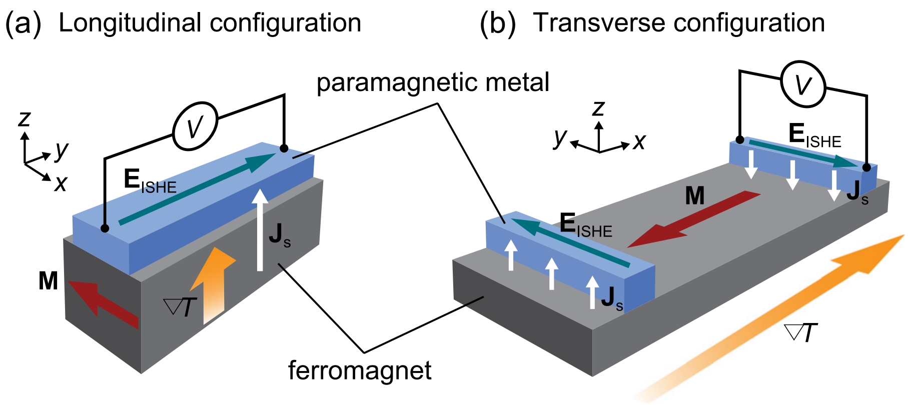

Figure 1.1: Picture from Ref. [100]. Visualization of the longitudinal (a) and transverse (b) spin Seebeck effect geometry. In the longitudinal configuration, the spin current is measured parallel to the temperature gradient, while the spin current is measured perpendicular to the temperature gradient in the transverse configuration. Nowadays most spin Seebeck effect measurements are carried out in the longitudinal configuration.

was caused by a separation of the two spin species in the ferromagnet due to the thermal gradient.

In 2010 the spin Seebeck effect was observed in ferromagnetic insulators [98] and magnetic semiconductors [40] suggesting that spin waves play an important role in the SSE due to the absence of free charge carriers in insulators.

In the same year Xiao *et al.* [106] published a theory of the spin Seebeck effect, where the spin Seebeck effect was explained in terms of thermal spin pumping [95] of thermally generated magnons. Xiao *et al.* predicted, that the spin Seeebck effect is proportional to the temperature difference between the electrons in the normal metal, used for spin detection, and the magnons in the ferromagnet, used for spin pumping.

So far, all measurements, reported in literature had been carried out in the transverse spin Seebeck effect geometry. However, in the same year Uchida *et al.* [97] showed that a thermovoltage could also be observed in the so called longitudinal configuration, where the temperature gradient is perpendicular to the interface between the spin detector and the magnetic material(*c. f.* fig. 1.1).

While contributions of magnons and electrons to the spin Seebeck effect were already discussed in literature, Adachi *et al.* [1] suggested an enhancement of the spin Seebeck effect due to the so called phonon drag mechanism. Temperature de-

pendent measurements by Jaworski *et al.* [41] confirmed that phonons can indeed drive a redistribution of spins.
In 2011, Uchida *et al.* [99] could show, that it is even possible to drive a spin current by direct excitation of phonons with a piezo electronic actuator. This technique was called acoustic spin pumping [22].
As mentioned at the beginning of this introduction, the spin Seebeck effect is a controversial topic. It has been argued that the observed thermovoltages in the longitudinal configuration could also be explained be the anomalous Nernst effect [38, 58, 81], even if magnetic insulators are used as the spin current source.
To separate the contribution from the spin Seebeck effect and the anomalous Nernst effect, Ramos *et al.* [72] performed temperature dependent measurements on magnetite which posseses an metal/insulator transition at $T = 115\,\mathrm{K}$. At this so called Verwey transition point of magnetite, the resistance of magnetite increases significantly, which should supress the Nernst contributions to the measured voltage, while not affecting the spin Seebeck part. From their measurement Ramos *et al.* concluded, that the contribution to the observed thermovoltage of the anomalous Nernst effect is less than 3% at room temperature.
Huang *et al.* [38] pointed out, that even in experiments using magnetic insulators the platinum, used for detection of the spin current in most experiments, can become magnetic due to the magnetic proximity effect [58]. They suggested to use gold instead of platinum as spin detector, with the former being diamagnetic and thus essentially nonmagnetic even in the presence of a magnetic interface [71].
XMCD measurements, performed by Geprägs *et al.* [29], did not show proximity induced magnetic moments at room temperature in samples, similar to the samples used in this thesis.
To distinguish between contributions from the spin Seebeck effect and the anomalous Nernst effect in ferromagnetic insulator/platinum samples, Kikkawa *et al.* [47, 48] performed spin Seebeck measurement in different magnetization/ temperature gradient configurations. They found, that the anomalous Nernst effect is small, if not experimentally insignificant, in YIG/Pt samples.

As mentioned above, the first observations of the spin Seebeck effect were made in the transverse configuration [40, 41, 96, 98]. So far however, only two research groups succeeded measuring the transverse spin Seebeck effect leading to an ongo-

ing debate about the validity of these first experiments. Simulations of the spin Seebeck effect further indicate, that the achieved temperature differences in the transverse configuration might not be large enough to explain the measured voltages [83]. Schmid *et al.* [81] explained the results of [96] with contributions from the anisotropic magnetothermo power and the anomalous Nernst effect due to a small out of plane temperature gradient. The tranverse SSE, as reported in 2008 by Uchida *et al.*., may thus be below the detection limit of today's electronics.
In conclusion, the spin Seebeck effect is a very contested topic. While the first measurements of the spin Seebeck effect were performed in the transverse configuration, only the longitudinal configuration is employed nowadays as these first results could not be reproduced. While spin Seebeck effect measurements in metals and semiconductors can be found in literature, current research mainly focuses on magnetic insulators which circumvent most but not all issues present in the discussion above.
Finally, the contribution of the anomalous Nernst effect due to proximity induced magnetization in the platinum layer is still under discussion [29, 30, 38, 58].

The transient spin Seebeck experiments, which will be presented in this thesis, contribute to the ongoing discussion outlined above. Since anomalous Nernst and spin Seebeck effect hinge on fundamentally different microscopic processes, both effects could be distinguished by time resolved measurements. Further, dynamic measurements will help to understand the microscopic mechanisms of the spin Seebeck effect.
Further, a new experimental setup for spin Seebeck effect measurements will be presented, which simplifies measurements which previously required sophisticated experiment setups. Thus this technique can accelerate the development in the field of spin caloritronics.

2 Theory of the spin Seebeck effect

This chapter outlines some key theoretical concepts relevant for the understanding of the spin Seebeck effect. First, spin currents are introduced. Afterwards, the spin Hall effect [36, 89], which converts spin currents into charge currents, will be discussed. Next, the model given by Xiao *et al.* [106] for the spin Seebeck effect will be presented, to give an intuitive understanding of this effect. Finally, the transient response on an external (thermal) perturbation of coupled systems is discussed, with a focus on time constants, relevant to the spin Seebeck effect.

2.1 Electron charge and spin currents

Electrons do not only carry a charge of $-e$, but also an intrinsic magnetic moment ("spin"). The spin of an electron is characterized by the spin angular momentum operator $\hat{\mathbf{S}} = \hbar/2(\sigma_x, \sigma_y, \sigma_z)^T$, with σ_i representing the Pauli matrices [10]. For the electron spin pointing along the z-direction, the eigenvalues of the spin operator are given as $m_s = \pm\hbar/2$ [10], where m_s is the spin magnetic moment.
It is possible, to define spin currents, carried by electrons in analogy to conventional charge currents. However, the definition of such a spin current is not straightforward, since the electron spin is not a conserved quantity due to spin orbit coupling [110].Consequently, it is not possible to set up a continuity equation for the spin current.
In literature, different approaches are found for the definition of a spin current [7, 73, 88, 92, 93, 107, 110], however, most of these approaches contain involved mathematical formalisms and will therefore not be discussed in detail in this thesis. In order to still give an intuitively understandable picture of spin currents, the situation in systems without spin orbit coupling will be described in a two spin channel model [17]. Here, the particle currents of spin-up electron $I_\uparrow$ and spin-down elec-

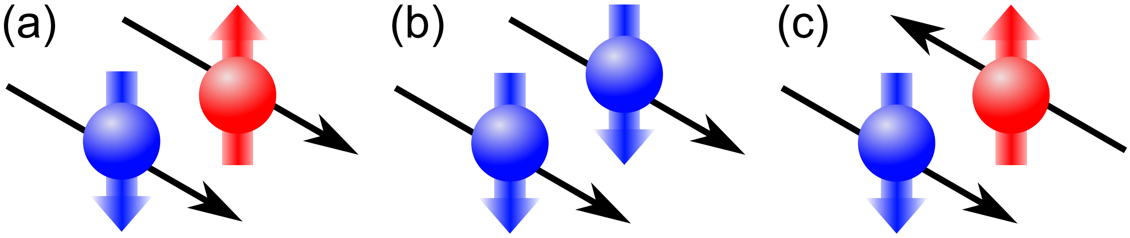

Figure 2.1: Sketch of spin (polarized) and charge currents. The intrinsic angular momentum ("spin") orientation of the electrons is color coded, as well as represented as an arrow. Panel (a) shows a pure charge current. Since both electrons carry different spin, the total spin angular momentum is zero and no spin information is carried. The charge current in panel (b) has the same magnitude as in panel (a), however, the total spin angular momentum is not zero. Therefore both spin angular momentum and electric charge are transported. This is called a spin polarized current. Panel (c) shows a pure spin current without charge transport, since the current directions for both spin species are opposed.

trons $I_\downarrow$ are considered separately. Since spin-up and spin-down electrons carry the same charge $-e$, the total charge current is given as:

$$I_\mathrm{c} = -e(I_\uparrow + I_\downarrow)\ . \tag{2.1}$$

With a spin magnetic moment of $m_s = \pm\hbar/2$, carried by one electron, a spin current can be written as:

$$I_\mathrm{s} = \frac{\hbar}{2}(I_\uparrow - I_\downarrow)\ . \tag{2.2}$$

The different signs for $I_\uparrow$ and $I_\downarrow$ are caused by the different directions of the spin magnetic moment for spin-up and spin-down electrons. Figure 2.1 gives an intuitive picture for spin and charge currents. In Fig. 2.1(a), $I_\uparrow$ and $I_\downarrow$ have the same direction and magnitude. Therefore the total charge current [Eq.(2.1)] is finite while the spin current [Eq.(2.2)] is zero.

In Fig.2.1(b), $I_\uparrow = 0$, therefore the charge current as well as the spin current is non vanishing. A pure spin current is depicted in Fig. 2.1(c), since $I_\uparrow$ and $I_\downarrow$ have different sign but same magnitude ($I_\uparrow = -I_\downarrow$). Consequently I_c will cancel out but I_s remains finite.

2.2 Magnonic spin currents

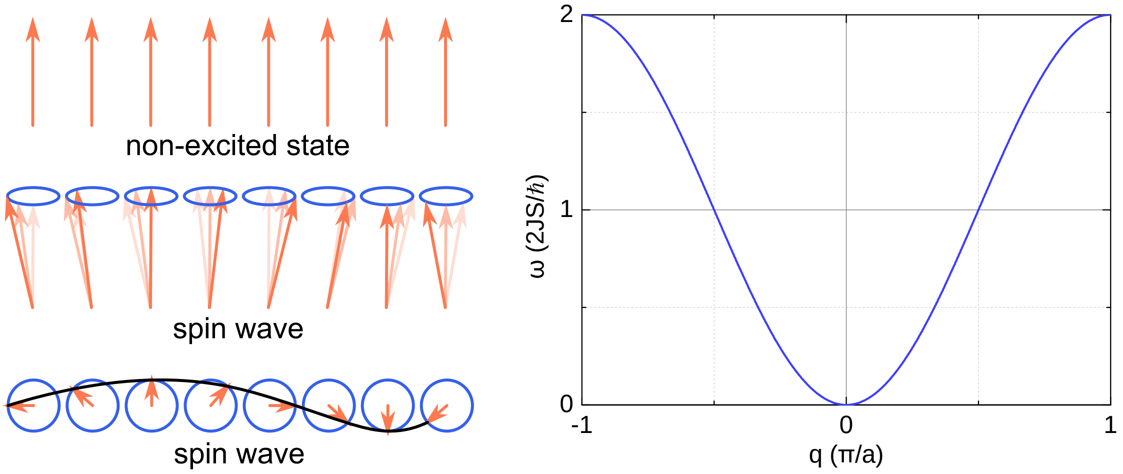

(a) Visualization of a spin wave.

(b) Dispersion relation of the spin waves in a linear chain of spins.

Figure 2.2: Panel (a) shows the ground state of a one dimensional chain of magnetic moments as well as two perspective views of an excited state. The excited state comprises a spin wave with $q \neq 0$. In panel (b), the dispersion relation of the spin waves in the one dimensional chain is depicted.

So far, spin current, carried by electrons were discussed. However, spin information can be carried by spin waves (magnons) as well [60]. In ferromagnetic insulators, no conduction electrons are available. In such systems the spin current is carried solely by spin waves [43, 44, 63].

The physics of spin waves will be illustrated with the examples of a one dimensional Heisenberg model[1] (a chain of magnetic moments with nearest neighbor interaction) [10, 32, 39]. The Hamiltonian of the system is given as

$$\mathcal{H} = -\frac{J}{\hbar^2} \sum_{m=1}^{N} \mathbf{S}_m \cdot (\mathbf{S}_{m-1} + \mathbf{S}_{m+1}) \tag{2.3}$$

where J is the exchange coefficient. The magnetic moment, associated with a spin is given as $\mu_m = -g\mu_\mathrm{B}/\hbar \cdot \mathbf{S}_m$, where g is the g-factor and μ_B is the Bohr magneton. It is assumed, that all magnetic moments point in the z-direction if the system is in

[1]The model is semi-classical. Therefore, the spin angular momentum operator $\hat{\mathbf{S}}$ will be replaces by a vector $\mathbf{S}$ of length $S = |\mathbf{S}|$.

its ground state. If a magnetic moment μ_m is deflected from the ground state, it will experience a torque due to the molecular field B_{M}, associated with the magnetic chain, and an external magnetic field B_{Ex}. This torque equals the time derivative of the spin angular momentum S_m [39]:

$$\frac{\mathrm{d}\mathbf{S}_m}{\mathrm{d}t} = -\frac{g\mu_{\mathrm{B}}}{\hbar}\,\mathbf{S}_m \times (\mathbf{B}_{\mathrm{M}} + \mathbf{B}_{\mathrm{Ex}}) \tag{2.4}$$

The molecular field $\mathbf{B}_{\mathrm{M}}$, seen by the spin $\mathbf{S}_m$ is given as [32]:

$$\mathbf{B}_{\mathrm{M}} = -\frac{J}{g\mu_{\mathrm{B}}\hbar}\,(\mathbf{S}_{m-1} + \mathbf{S}_{m+1}) \tag{2.5}$$

Substituting this expression into Eq. (2.4) gives an equation of motion for $\mathbf{S}_m$. Since the deflection of $\mathbf{S}$ in x- and y-direction is assumed to be small, higher order terms in S^x and S^y are neglected. Further $S^z \approx |\mathbf{S}| = S$. With the external field oriented in z-direction ($B_{\mathrm{Ex}} = B^z$), one obtains:

$$\frac{\mathrm{d}S^x_m}{\mathrm{d}t} = -\frac{g\mu_B B^z}{\hbar}\,S^y_m - \frac{JS}{\hbar^2}\,(2S^y_m - S^y_{m-1} - S^y_{mx1})\;, \tag{2.6}$$

$$\frac{\mathrm{d}S^y_m}{\mathrm{d}t} = -\frac{g\mu_B B^z}{\hbar}\,S^x_m - \frac{JS}{\hbar^2}\,(2S^x_m - S^x_{m-1} - S^x_{mx1})\;, \tag{2.7}$$

$$\frac{\mathrm{d}S^z_m}{\mathrm{d}t} = 0\;. \tag{2.8}$$

This equations can be solved with an exponential ansatz [32]:

$$S^x_m = S^x \cdot e^{i(qma-\omega t)}\;,\qquad S^y_m = S^y \cdot e^{i(qma-\omega t)}. \tag{2.9}$$

Here, a is the distance between two interacting magnetic moments (lattice constant). The solution, obtaind with the aforementioned ansatz is the dispersion relation for spin waves [32]:

$$\omega = \frac{g\mu_B B^z}{\hbar} + \frac{2JS}{\hbar}\,(1-\cos(qa))\;. \tag{2.10}$$

This dispersion relation is plotted in Fig. 2.2(b). Further it is found, that S^x and S^y have the same magnitude but differ by a phase of 90°: $S^y = iS^x$. The physical meaning of this relation is, that the magnetic moments precess in a circular motion around their ground state position.

Especially interesting is the uniform magnetic precession mode for $q = 0$. If an external magnetic field is applied, all moments will precess in phase with the frequency

$$\omega = \frac{g\mu_B}{\hbar} B^z = \gamma B^z . \tag{2.11}$$

This is the Lamor frequency proportional to the gyromagnetic ratio γ. It is possible to excite the uniform magnetic precession mode with microwave excitations in so called ferromagnetic resonance experiments.
Naturally, the spin wave dispersion in a real system such as the ferrimagnetic insulator yttrium iron garnet (YIG, $Y_3Al_5O_{12}$) is much more complex than in the simple model presented here (*cf.* Ch. 3). Fundamentally, however, spin waves can always be understood in a semi-classical picture as a precession of magnetic moments.

2.3 Spin Hall effect

The spin Hall effect and the inverse spin Hall effect provide a bridge between conventional electronics and spin electronics because they allows to convert charge currents to spin currents and vice versa [36, 89]. Spin currents, for example generated by the spin Seebeck effect or spin pumping, are usually measured by utilizing the spin Hall effect [67, 84, 97, 104]. The spin Hall effect converts spin currents in charge currents which can be detected with conventional measurement electronics.
A microscopic picture for the understanding of the spin Hall effect was provided by Dyakonov *et al.* [24] and later by Hirsch [36]. While electrons move through a paramagnetic metal, they are scattered at e.g. charged impurities. Since skew scattering and side jump scattering is asymmetric with respect to the spin orientation, the probability of a certain electron path depends on the spin orientation [101]. This situation is depicted in Fig. 2.3. Here electrons with different spin orientation are scattered in different directions, giving rise to a spin current perpendicular to the charge current. In addition to scattering at impurities, the spin Hall effect can also be caused by intrinsic mechanisms [66, 89].
So far, the spin Hall effect has been discussed, which describes the generation of a spin current due to the flow of a charge current. However, the inverse process is possible as well due to Onsager reciprocal relations [49]. This is called inverse spin

Hall effect. The charge current $\mathbf{I}_c$, generated by a spin current $\mathbf{I}_s$ is given by [106]:

$$\mathbf{I}_c = +\theta_H \frac{2|e|}{\hbar} \mathbf{I}_s \times \boldsymbol{\sigma} \tag{2.12}$$

Here, e is the elementary charge, $\boldsymbol{\sigma}$ is the spin polarization vector of the spin current, I_s the spin current, I_c the charge current and θ_H is the spin Hall angle, which is a measure for the conversion efficiency.

Experimental evidence for the spin Hall effect was found with different measurement approaches. In semiconductors, the spin Hall effect was measured using Kerr microscopy [45]. Valenzuela *et al.* [101] injected a spin polarized current into a normal metal via tunneling from a ferromagnetic electrode and detected the inverse spin Hall voltage in the former. Finally Saitoh *et al.* [78] used the technique of spin pumping to inject a spin current into platinum. Also this spin current was detected via the inverse spin Hall effect.

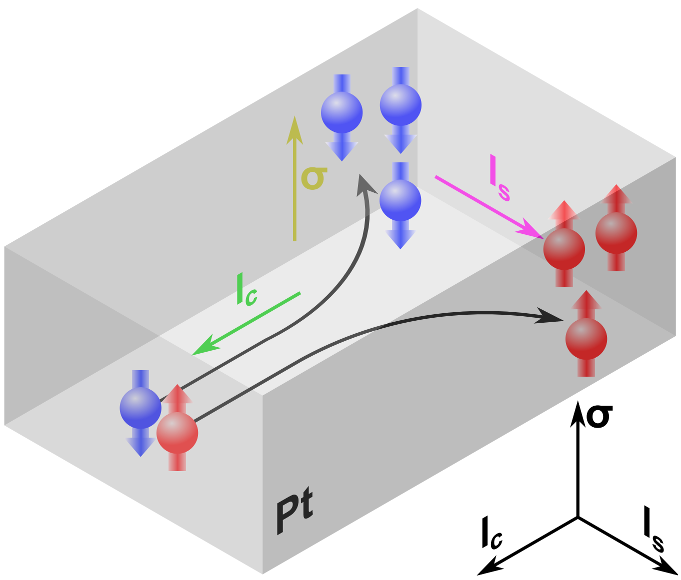

Figure 2.3: Visualization of the spin Hall effect in a paramagnetic metal. Due to spin dependent scattering rates, both spin species are scattered in different directions. This causes a conversion of an unpolarized charge current j_c into a pure spin current j_s. Spin current, charge current and the spin polarization are perpendicular to each other.

2.4 Spin Seebeck effect

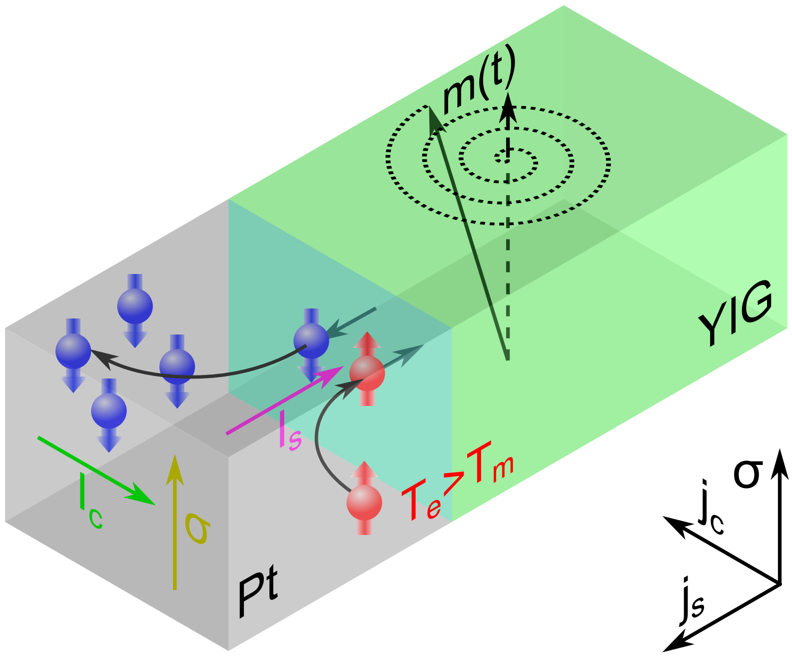

Figure 2.4: Spin Seebeck effect in YIG/Pt bilayer according to the theory by Xiao *et al.* [106]. Thermal energy leads to a precession of the magnetization in the YIG layer. This gives rise to a spin current in the platinum via the mechanism of spin pumping. The spin current in the platinum gets converted into a charge current due to the inverse spin Hall effect.

In a ferromagnetic insulator/normal metal bilayer, a spin current between the ferromagnetic insulator and the normal metal can be excited under application of a temperature gradient. Via the inverse spin Hall effect, this spin current can be converted into a charge current. It is then possible to measure a voltage under open circuit conditions. This is called spin Seebeck effect [9]. An intuitive picture of the spin Seebeck effect is provided in the theory of Xiao *et al.* [106]. Thermal energy leads to the precession of magnetic moments in a ferromagnetic insulator which is characterized by the magnon temperature T_m. By the mechanism of spin pumping [95], the precessing magnetization excites a spin current into the normal metal. This situation is depicted in Fig. 2.4.

However, thermal noise in the normal metal layer leads to a spin current from the normal metal into the ferromagnetic insulator. The electron temperature T_e is a

measure for the thermal energy of the electrons and thus for the spin current from the normal metal into the ferromagnet.
In conclusion, the total spin current is a superposition of the spin pumping current, depending on T_m and the fluctuating spin current, depending on T_e. The corresponding expectation value for the spin current is found to be [106]:

$$\langle j_s \rangle = L_\mathrm{s}(T_\mathrm{m} - T_\mathrm{e}) \tag{2.13}$$

Thus the spin current is proportional to the temperature different between magnons in the ferromagnetic insulator T_m and the electrons in the normal metal T_e. L_s is the interfacial spin Seebeck coefficient. The direction of the spin current is perpendicular to the normal metal/ ferromagnetic insulator interface. If the electron temperature in the normal metal T_e is higher as the magnon temperature in the ferromagnet T_m, the direction of the spin current will be from the normal metal into the ferromagnet and vice versa. The origin of such a temperature difference will be discussed in the next section.
The theory by Xiao *et al.* [106] presented here is based on the macro-spin approximation. Thus, the collective mode dominates the dynamics and the spin current generation in their model. It was explained in Sec. 2.2, that the wavenumber is zero for these excitations. Newer theories are based on thermal magnon excitations [74, 94]. As explained in Sec. 2.5, dfferent time constants are associated with these different theoretical approaches. The objective of transient spin Seebeck effect measurements, performed in Ch. 4 of this thesis, is to distinguish between the different theoretical approaches.

2.5 Temperature profiles in ferromagnetic insulator/ normal metal bilayers

As discussed in the previous section, the spin Seebeck effect is driven by a difference of the magnon temperature T_m in the ferromagnetic insulator and the electron temperature T_e in the normal metal according to Xiao *et al.* [106]. This section will address the question, how the temperature difference $\Delta T_\mathrm{me} = T_\mathrm{m} - T_\mathrm{e}$ hinges on the magnon-phonon interaction time.

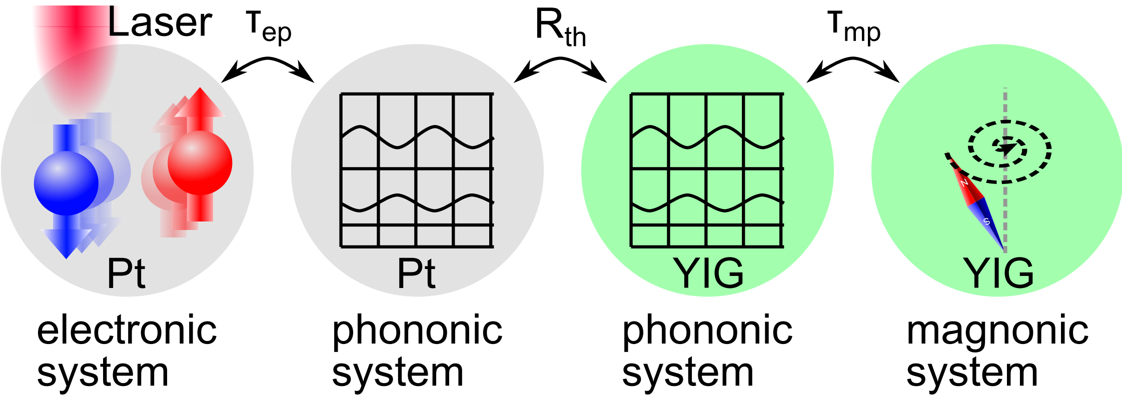

Figure 2.5: Dynamics of the spin Seebeck effect according to the theory by Xiao *et al.* [106]. A temperature gradient is induced (e.g. via electromagnetic irradiation). Excited, hot electrons in the platinum transfer heat via electron-phonon interaction, into the platinum phononic system. The phononic systems of the platinum and the YIG are coupled through the Pt/YIG interface with the thermal resistance R_{th}. In the YIG, energy is transfered to the magnonic system due to magnon-phonon interaction. The heat transport due to the spin current across the YIG/Pt interface as well as heat transport to the substrate are neglected.

In normal insulators, heat is carried by lattice excitations (phonons). However in ferromagnetic insulators, heat can also be carried by magnetic excitations (magnons). Experimental evidence for this phenomena was found in transport measurements on YIG at low temperatures and in high magnetic fields [21]. It was reported, that magnons contribute up to 66 % to the total heat capacity of YIG at low temperatures [76].

To understand the dynamic processes leading to a temperature difference of electrons in the platinum and magnons in the YIG under the application of a thermal gradient, a simple model is introduced in Fig. 2.5 [83, 106]. In this model, the temperature imbalance is generated via electromagnetic irradiation e.g. with a laser. This electromagnetic irradiation couples strongly to the electronic system in the platinum. Excited electrons will equilibrate with the phononic system [57]. This process is associated with the elecron-phonon interaction time τ_{ep}. Since the platinum film is grown on YIG, the phonon system in the platinum is coupled to the phonon system in the YIG via the YIG/platinum interface. A thermal resistance R_{th} is associated with the interface [83].

Coupling between the phonons and the magnons in the YIG gives rise to a heat current between both systems [83]. The coupling is characterized by the magnon-phonon interaction time τ_{mp} [106]. In addition, the phononic system of the YIG is also coupled to the phononic system of the substrate, which can be assumed as a very large heat reservoir[2].

In the model by Xiao *et al.*, the heat flux carried by the spin current from the electron system to the magnon system, caused by thermal spin pumping, is neglected. It is assumed that the interface magnetic heat conductance K'_{m} is negligibly small. Later studies [27, 37, 83], however, found this contribution to significantly impact the magnon temperature.

Summing up, the electron temperature is changed directly via laser irradiation, while the magnon temperature is altered via magnon-phonon interaction. Time constants are associated with the electron-phonon equilibration process (τ_{ep}) as well as with the magnon-phonon interaction (τ_{mp}). Under constant laser irradiation, a steady state will be establish with constant temperature difference $\Delta T_{\mathrm{me}} = T_{\mathrm{m}} - T_{\mathrm{e}}$. However, it can be expected that the temperature difference ΔT_{me} will change, if the laser intensity is modulated on time scales, close to or shorter as the time constants mentioned above. Therefore transient spin Seebeck effect measurements can be utilized to probe these time constants.

[2]For the experiments, insulating substrates were chosen. Thus the substrate acts as a heat sink but has no further contribution to the experiments [82].

3 Samples for spin Seebeck effect measurements

This chapter discusses of the properties and fabrication of the YIG/Pt thin film samples on which the measurements discussed in this thesis were performed. All samples, investigated in this thesis, were grown by Sibylle Meyer, Matthias Althammer and Felix Schade at the Walther-Meißner-Institute. The lithography process was conducted by Michael Schreier, Sibylle Meyer, Matthias Althammer and the author of this thesis, also at the Walther-Meißner-Institute. At the end of this chapter, an overview of the sample geometry will be given.

3.1 Yttrium Iron Garnet

Yttrium iron garnet is a synthetic garnet [12]. It is often used for spin Seebeck effect measurements as a spin sink or source [84, 97, 103] because it is not only ferrimagnetic at room temperature but also insulating. This special property allows to perform spin Seebeck effect measurements without spurious contributions from other thermo-magneto-electric effects such as the anomalous Nernst effect.
Reference [12] provides a good overview of the magnetic properties of YIG. The structural formula of YIG is $Y_3Fe_5O_{12}$. It crystallizes in a bcc structure with a lattice constant of $a = 12.4\,\text{Å}$. This large lattice constant implies already, that YIG has a very complex unit cell, which consists of 80 atoms out of which 20 are magnetic.
At $T = 0\,\text{K}$ the 20 magnetic ions lead to 20 different magnon branches in the magnon dispersion relation of YIG, as shown in Fig. 3.1. The arrow in Fig. 3.1 indicates the uniform magnetic precession mode which is commonly excited in ferromagnetic resonance experiments. The Curie temperature of YIG ($T_\text{C} = 560\,\text{K}$) is well above room temperature.

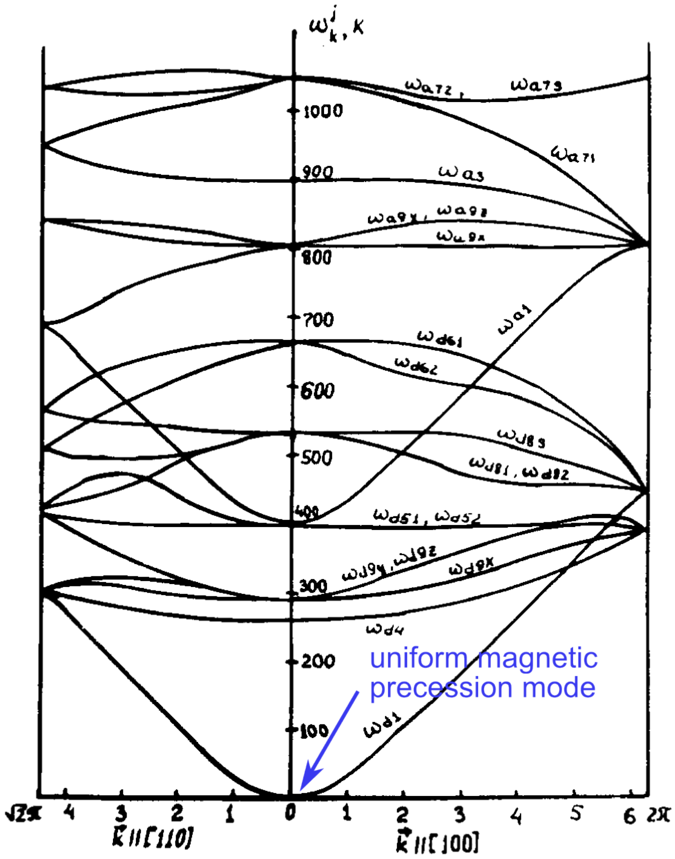

Figure 3.1: Picture from [12]. The magnon spectrum of YIG for the directions $k||[110]$ and $k||[100]$ at $T = 0\,\mathrm{K}$. The 20 magnetic ions per unit cell lead to 20 different magnon branches. The uniform magnetic precession mode, which can be excited in ferromagnetic resonance experiments, is indicated with an arrow.

3.2 Sample fabrication

The fabrication process of the YIG/Pt samples is described in detail in Refs. [6, 29]. Single crystalline $Y_3Al_5O_{12}$ (yttrium aluminium garnet, YAG) or $Gd_3Ga_5O_{12}$ (gadolinium gallium garnet, GGG) substrates with (111) orientation were used for epitaxial YIG growth[1]. YIG was deposited with pulsed laser deposition from a polycrystalline stoichiometric target. A KrF laser with $\lambda = 248\,\mathrm{nm}$ was used for the deposition.

[1]It was found that both substrates do not influence the spin Seebeck effect measurements [82].

On top of the YIG film, a platinum layer is deposited in situ, without breaking the vacuum, by electron beam evaporation. Due to the lattice mismatch between platinum and YIG, platinum grows polycrystalline. The platinum layer is used as a spin current detector, by means of the inverse spin Hall effect (*cf.* Sec. 2.3).
In order to perform spin Seebeck effect measurements on the YIG/Pt samples, the samples were patterned with optical lithography. After the lithography process, reactive ion etching was used to etch the platinum and YIG.

3.3 Sample geometry

All measurements, in Ch. 5 were performed on YIG/Pt samples, patterned with a Hall bar structure, as shown in Fig. 3.2(b). The Hall bar consists of 10 bond pads allowing to measure voltages along, both, the long and the short stripes. The size of the long stripe is $1\,\mathrm{mm} \times 80\,\mu\mathrm{m}$.

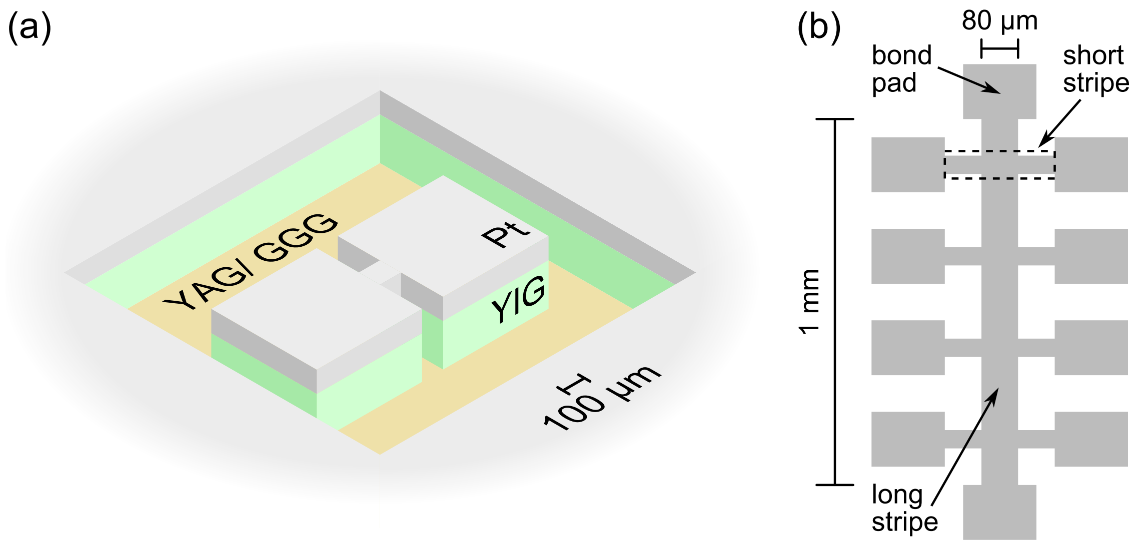

Figure 3.2: Schematic of the sample layouts, used for spin Seebeck effect measurements. The dimensions in the figure are not to scale. Panel (a) shows the sample geometry used in Sec. 4.3.2 for high frequency spin Seebeck effect measurements. Here, two bond pads are connected via a $100\,\mu\mathrm{m} \times 100\,\mu\mathrm{m}$ bridge. In panel (b), the Hall bar structure, used for most measurements in this thesis is shown. Twp bond pads are connected by a $80\,\mu\mathrm{m}$ wide, $1\,\mathrm{mm}$ long stripe, with four additional pairs of bond pads giving access to transverse voltages via the short stripes.

sample #	lab name	d_{YIG} [nm]	d_{Pt} [nm]	R (Ohm)	Substrate
1	YY21	61	19.5	309	YAG
2	YY43	48	4.9	876	YAG
3	YY63	55	16.8	47	YAG
4	YIG59	61	11	217	GGG
5	YIG105	16.3	2.8	1430	GGG

Table 3.1: This tables gives an overview over the different YIG/Pt samples used for measurements in this thesis. d_{YIG} and d_{Pt} denote the thickness of the YIG and platinum layer respectively.

In Ch. 4, a second structure was used for high frequency spin Seebeck effect measurements. This structure is shown in Fig. 3.2(a). It consists of two bond pads, connected by a $100\,\mu\mathrm{m} \times 100\,\mu\mathrm{m}$ small bridge. Table 3.1 provides an overview over the YIG samples used for measurements, performed within the framework of this thesis.

4 Time resolved spin Seebeck effect experiments

In this chapter, the time resolved measurements of the spin Seebeck effect will be discussed. For these experiments, a transient temperature gradient along a normal metal/ ferrimagnetic insulator interface is established with laser heating. After a motivation for time resolved spin Seebeck effect experiments, the chapter will begin with a description of the experimental setup. Spatially resolved measurements of the spin Seebeck voltage are discussed subsequently to illustrate the sample geometry and the function of the setup. The time resolved measurements were performed with a lock-in amplifier and with a digitizing card. Results, obtained with both measurement techniques will be discussed and compared. From these measurements it is concluded, that the spin Seebeck effect is not dominated by small wavenumber magnons. Rather, the complete magnon spectrum has to be considered.

4.1 Motivation: Time resolved spin Seebeck effect experiments as a probe of magnon phonon thermalization time

We investigate the spin Seebeck effect in YIG/Pt structures [77]. YIG is a ferrimagnetic insulator, while Pt is a normal metal, used for the detection of a spin current via the inverse spin Hall effect. In section 2.4 it was argued, that the spin Seebeck effect is caused by a thermal non-equilibrium in the magnetic system. This assumption is supported by recent spin Seebeck effect theories [2, 3, 14, 37, 94].

A thermal non-equilibrium situation is usually generated externally, e.g. by electromagnetic irradiation. In order to relax back to thermal equilibrium, heat currents will emerge in the system. The heat current in YIG is carried by magnons and phonons, while the heat current in Pt is carried by electrons and phonons. In addition, a heat current across the interface, carried by phonons and the spin current will emerge. Thermal interaction times between the heat reservoirs determine the dynamics of the spin Seebeck effect. A roll off in the spin Seebeck effect can be expected, if the non-equilibrium will be generated on time scales, shorter as the aforementioned interaction times.
The electron-phonon interaction time in the platinum layer is known to be in the picosecond regime [57]. Experimental data of the time constant associated with heat transport across the YIG/Pt interface was not reported in literature. However, in theory this time constant is assumed to be very small [106]. Therefore, the dynamics of the spin Seebeck effect is ultimately limited by the magnon-phonon interaction time τ_{mp} in the YIG [106]. Transient measurements of the spin Seebeck effect could thus enable an estimation of τ_{mp} and give insights in the dynamics of the spin Seebeck effect.
Getting a better understanding of the dynamics of the spin Seebeck effect is especially important since recent spin Seebeck effect theories use very different assumptions concerning the magnon-phonon interaction. Rezende *et al.* [74] as well as Hoffman *et al.* [37] assume strong coupling between the magnetic system (magnons) and the lattice (phonons) and as a consequence, equal magnon- and phonon temperatures in the ferrimagnetic insulator, eg. $\tau_{\mathrm{mp}} \ll 1\,\mu\mathrm{s}$. In the theory of Xiao *et al.*, it is assumed that $k = 0$ magnons (uniform magnetization precession mode) are relevant for the spin Seebeck effect [106]. The magnon-phonon interaction time for the uniform precession mode in bulk YIG crystals was measured in ferromagnetic resonance experiments and is on the time scale of $\tau_{\mathrm{mp}} \approx 1\,\mu\mathrm{s}$ [80]. Tikhonov *et al.* [94] and Schreier *et al.* [83] consider a thermally distributed magnon spectrum with much smaller interaction times to be relevant for the spin Seebeck effect ($\tau_{\mathrm{mp}} \approx 255\,\mathrm{ps}$).
Agrawal *et al.* [4] attempted to measure the magnon- and phonon temperatures in YIG, using an infrared camera and Brillouin light scattering from which one can infer τ_{mp}. However, theoretical calculations suggest, that the resolution of this method may not be sufficient in order to obtain the desired information [83]. In this

chapter, transient measurements of the spin Seebeck effect will be presented, which allow to distinguish between the different theoretical approaches mentioned in the previous paragraph. An intensity modulated laser is used to establish a temperature imbalance on short timescales. For laser intensity modulation frequencies in the range of $2\pi f_{\mathrm{mod}} \approx 1/\tau_{\mathrm{mp}}$, we expect a change in the spin Seebeck voltage, since magnons and phonons can not equilibrate with each other. As mentioned above, τ_{mp} is of the order of 1 µs for small wavenumber magnons [80], which corresponds to a cutoff frequency f_{mod} of a few megahertz. Measurements will be presented in this chapter, which show that no change in the spin Seebeck voltage is experimentally observed up to laser intensity modulation frequencies of $f_{\mathrm{mod}} = 50\,\mathrm{MHz}$. Consequently, the contribution of large k magnons must be important for the spin Seebeck effect.

4.2 Experimental setup

All measurements discussed in this chapter were carried out in the longitudinal spin Seebeck effect geometry [97]. This means that the temperature gradient is applied perpendicular to the normal metal/ ferromagnet interface and the spin current is parallel to temperature gradient.
Laser heating is used in this chapter to create a temperature gradient [5, 77, 102, 103]. Since a laser beam can be focused down to a few µm and thus the temperature gradient is created only locally, this technique allows position dependent measurements. Further, a laser suits well to probe the dynamics of the spin Seebeck effect, since it allows to change the temperature gradient on short timescales by modulating the laser intensity.
The samples, used for the time resolved measurements are YIG(d_1)/Pt(d_2) structures on YAG substrates. Here, $d_{1/2}$ denotes the corresponding film thickness in nm. The fabrication process of the samples is described in Sec. 3.2. Two samples, studied in this chapter are patterned with Hall bar mesa structures. Different film thicknesses were investigated in order confirm the RC-lowpass model introduced in Ch. 4.3. A different mesa structure design (*cf.* Sec. 3.3) was used for a third sample, to avoid cutoffs, due to lowpass circuitry.

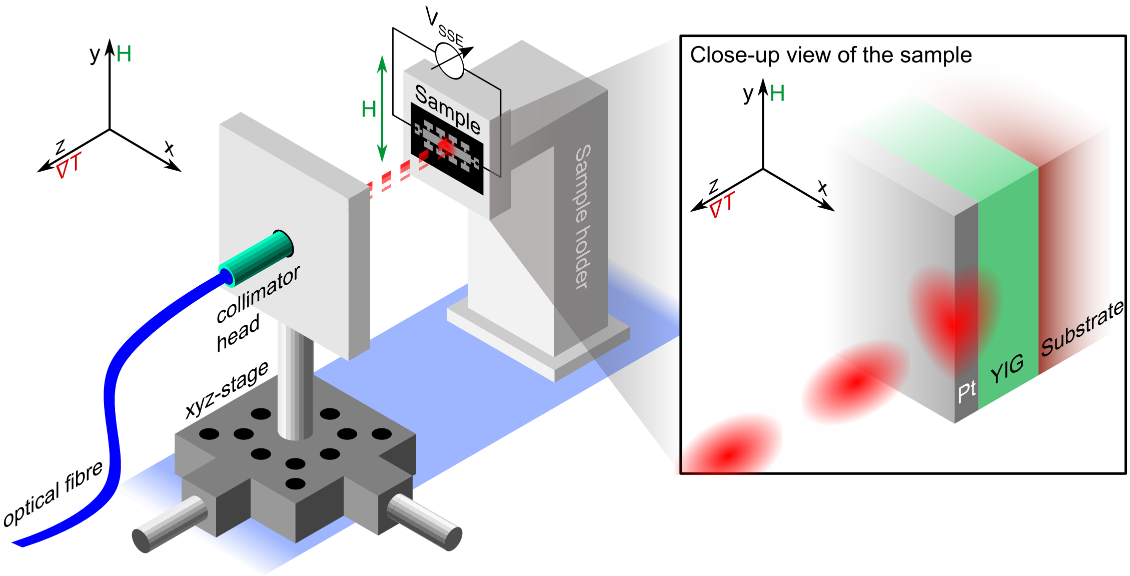

Figure 4.1: Sketch of the experimental setup for spatially resolved spin Seebeck effect measurements [103]: The laser beam is coupled into an optical fiber and focused by a collimator pack at the end of the fiber. This collimator pack is mounted on a xyz-stage, allowing to move the laser spot on the sample surface and to adjust the focus. In order to measure the spin Seebeck voltage along x, a magnetic field has to be applied in the y-direction, while the temperature gradient is along z. The close-up view shows the YIG/Pt layer stack from the side. Note, that the temperature gradient, induced by the laser is radially symmetric in the film plane.

The experimental setup to measure a spin Seebeck voltage with a laser is sketched in Fig. 4.1. The laser (*Toptica iBeam smart*, $\lambda_{\text{Laser}} = 645\,\text{nm}$) is coupled into an optical fiber. A collimation pack, mounted on a xyz-stage, is used to focus the laser beam and allows to position the laser spot on the sample. To obtain spatially resolution, the laser is moved in the x- and y-direction, while the z-direction is changed in order to control the focus.
Additionally, a magnetic field can be applied in y-direction. For all following measurements, magnetic fields of $\mu_0 H = 70\,\text{mT}$ were applied in order to align the magnetization of the YIG film along the external field ($70\,\text{mT} \gg \mu_0 H_c$, *cf.* Sec. 5.3.2). The spin Seebeck voltage is measured in the x-direction, perpendicular to the temperature gradient and the magnetic field. All experiments are carried out at room temperature. Figure 4.2 shows a block diagram of the electronics, used in this setup. The samples are contacted with Al bonds and glued on a chip carrier with

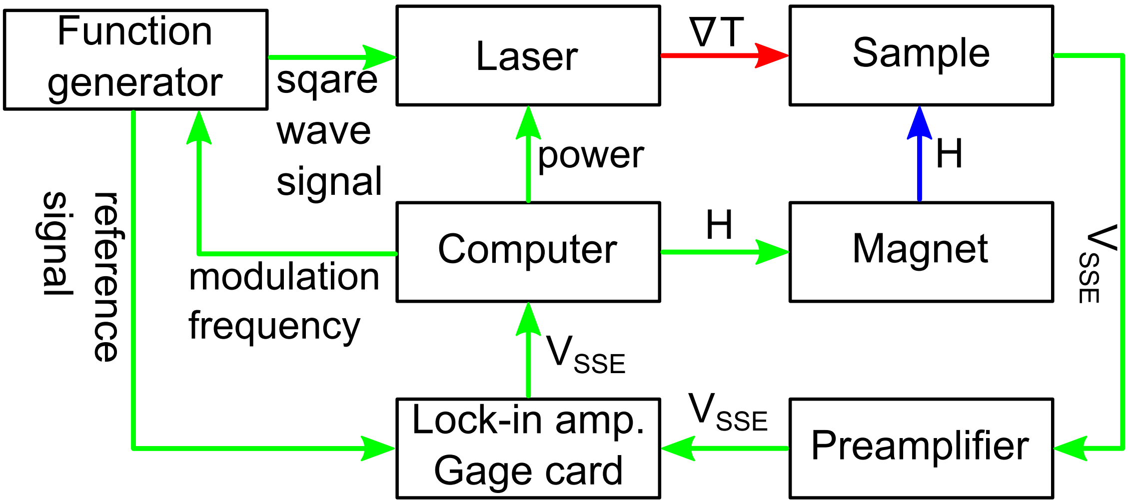

Figure 4.2: Block diagram of the experimental setup for spin Seebeck effect measurements. The computer is used to control the magnetic field, the laser intensity and the modulation frequency of the function generator. The function generator modulates the laser intensity with a square wave function and provides a reference signal for the lock-in amplifier or the Gage card. With the laser, a temperature gradient ∇T is applied to the sample. The spin Seebeck voltage is preamplified and detected by the lock-in amplifier or the Gage card.

silver paste. Coaxial cables are used to connect the sample carrier to a preamplifier (*FEMTO HVA-200M-40-F* for YIG(48)/Pt(4.9)[1] and YIG(61)/Pt(19.5) or *FEMTO DHPVA-200* for YIG(55)/Pt(16.5), depending on the sample resistance). After amplification, the signal is either recorded with a lock-in amplifier (*Zurich Instruments HF2LI*) or a digitizing card (*GaGe Razor*). The modulation signal for the laser amplitude is provided by a function generator which also feeds the detection electronics with a reference signal.

4.2.1 Spatial resolved spin Seebeck voltage

In section 2.4, it was argued, that the spin Seebeck effect is driven by an imbalance between the electron temperature T_e in the Pt, and the magnon temperature T_m in the YIG [106]. This temperature imbalance is induced by laser heating in the sample stack of YAG/YIG/Pt. The absorption coefficient of YIG is small for light in

[1]The numbers in brackets denote the film thickness in nm

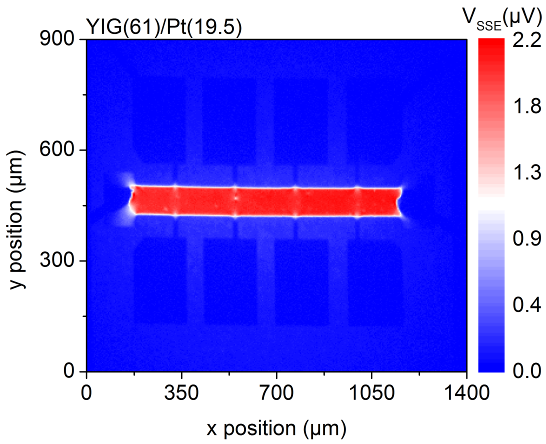

(a) Full voltage range image

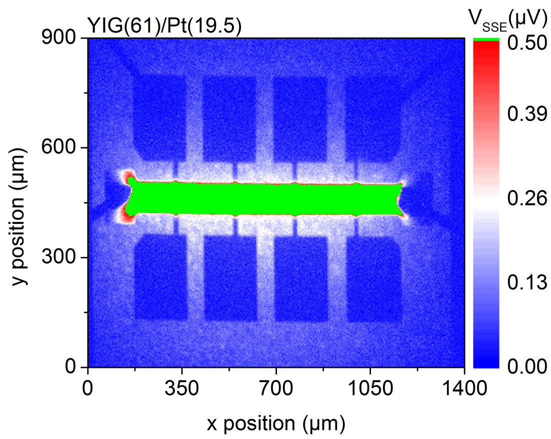

(b) Smaller voltage range image

Figure 4.3: Spatially resolved spin Seebeck voltage in false color representation. In the full voltage range image (panel (a)), the Hall bar body appears as a red bar. However, in the smaller voltage range image (panel (b)), the contact pads can be seen as well. This effect is caused by the backreflection of laser light from the sample's bottom side which is then absorbed in the Pt layer. Since the transverse contact pads are essentially intransparent to the laser light no signal is observed here.

the visible spectrum [85], so the laser light is mostly absorbed in the Pt. Therefore the Pt is always warmer than the YIG and the spin current is flowing out of the Pt into the YIG (*cf.* Sec. 2.4). By means of the inverse spin Hall effect in the Pt layer, the spin current $\mathbf{j}_\mathrm{s}$ gets converted into a charge current $\mathbf{j}_\mathrm{c}$ (*cf.* Sec. 2.3). Under open circuit conditions for $\mathbf{j}_\mathrm{c}$ this leads to a charge accumulation at the ends of the sample and thus a potential difference V_ISH between the measurement contacts. This voltage is preamplified and detected with a lock-in amplifier.
To avoid voltage pickup of parasitic signals V_para, e.g. caused by the conventional Seebeck effect, the symmetry of the spin Hall voltage V_ISH with respect to the magnetic field (Sec. 2.3) is used:

$$V_\mathrm{ISH}(+B) + V_\mathrm{para}(+B) = -V_\mathrm{ISH}(-B) + V_\mathrm{para}(-B). \tag{4.1}$$

Inversion of the magnetic field will lead to an inversion of the spin Hall voltage, while parasitic signals are not affected by the magnetic field direction. Thus, after subtraction of signals measured for both directions of the magnetic field, only the spin Seebeck voltage will remain. Since the measurements are performed with a lock-in amplifier, both voltage channels V_x and V_y have to be considered[2]:

$$V_\mathrm{x} = (V_\mathrm{ISH} + V_\mathrm{para}) \cdot \cos(\alpha), \quad V_\mathrm{y} = (V_\mathrm{ISH} + V_\mathrm{para}) \cdot \sin(\alpha) \tag{4.2}$$

The phase α can be adjusted, such that all signal is contained in one channel. Finally, the spin Seebeck voltage V_SSE is defined as the difference in voltage after inversion of the magnetic field. Assuming that the signal is contained in the x-channel only we thus have:

$$V_\mathrm{SSE} := V_\mathrm{x}(-B) - V_\mathrm{x}(+B) \tag{4.3}$$

$$= 2V_\mathrm{ISH} \tag{4.4}$$

It is necessary, that the phase α does not change during measurements because otherwise the signal will not be contained in the x-channel only. This is usually true for measurements with a fixed modulation frequency, such as position dependent measurements. However, for measurements where the modulation frequency will be changed (*cf.* Sec. 4.3), the discussed procedure will not be possible anymore.
Since the sample is only heated locally one can discriminate measurements at different laser spot positions. This allows to record a spin Seebeck voltage map $V_\mathrm{SSE}(x,y)$. Such a map is plotted in Fig. 4.3 for the sample YIG(48)/Pt(4.9). Here, the voltage was measured between the two contacts $(x,y) = (100\,\mu\mathrm{m}, 450\,\mu\mathrm{m})$ and $(1200\,\mu\mathrm{m}, 450\,\mu\mathrm{m})$. For this measurement, the laser was modulated at a frequency of $f_\mathrm{mod} = 200\,\mathrm{kHz}$. This allows short integration times for the lock-in amplifier. Therefore the time limiting factor of the measurement was the positioning of the collimator pack with the *xyz*-stage ($\approx 0.5\,\mathrm{s}$ per data point). The number of data points of the voltage map is approx. 0.5 MPixel.
The red bar in Fig. 4.3(a) correlates exactly with the size and shape of the Hall bar body. This means, that a large voltage signal is measured whenever the laser spot illuminates the Hall bar body. The size of the Hall bar body is $1000\,\mu\mathrm{m} \times 80\,\mu\mathrm{m}$. The blue color next to the Hall bar indicates smaller voltages, when the laser does not heat the Hall bar body.

[2] Please notice that V_x and V_y denote the x- and y- voltage channel of the lock-in amplifier respectively, while $V(x,y)$ denotes a position dependent voltage.

In fig. 4.3(b) the same data are presented but with a different voltage scale. The image shows, that a voltage signal can still be measured, when the laser hits the YIG layer in proximity to the Pt Hall bar body. This voltage is one order of magnitude smaller and can be explained with back reflections of the light from the back of the substrate,since the laser light can pass the YIG and substrate layers without being absorbed [85]. The reflected light can again heat the Pt layer of the Hall bar body.

Further, no voltage is measured, when the laser is scanned across the contact pads of the Hall bar. Here, the majority of the light is absorbed upon initial incidence. While a spin Seebeck voltage is generated here as well, the geometry of the Hall bar prevents any sizeable voltage difference to built up between the measurement contacts [82, 103].

4.2.2 High frequency characterization of the setup

To understand the high frequency behavior of the lock-in amplifier, the output of a frequency generator is connected directly to the lock-in amplifier via a coaxial cable [*cf.* inset of Fig. 4.4(a)]. For different frequencies in the range of 100 kHz up to 50 MHz, the magnitude V_{pp} and the phase of a sine wave with a peak to peak amplitude of $V_{\mathrm{pp}} = 100\,\mathrm{mV}$ was recorded with the *Zurich Instruments HF2LI* lock-in amplifier. Up to frequencies of about 20 MHz, the full peak amplitude V_{pp} of the signal is recorded. The phase shift at 20 MHz is 60°. In the amplitude-frequency response diagram [Fig. 4.4(a)], a maximum at 13 MHz indicates a resonance. For frequencies above 30 MHz, the signal is attenuated. At 50 MHz, 60% of the unattenuated signal is measured. The large phase shift of 180° at a frequency of 30 MHz [*cf.* Fig. 4.4(b)] can be explained by the finite velocity of the electromagnetic signal in the coaxial cable. The phase φ of an electromagnetic wave is given by [34]:

$$\varphi = \vec{k} \cdot \vec{r} - \omega \cdot t.$$

$\vec{k}$ is the wave vector, $\vec{r}$ is a position vector and ω is the wave number. During a time $t = L/v$ (L is a distance and v the speed of the wave) from the sample to the

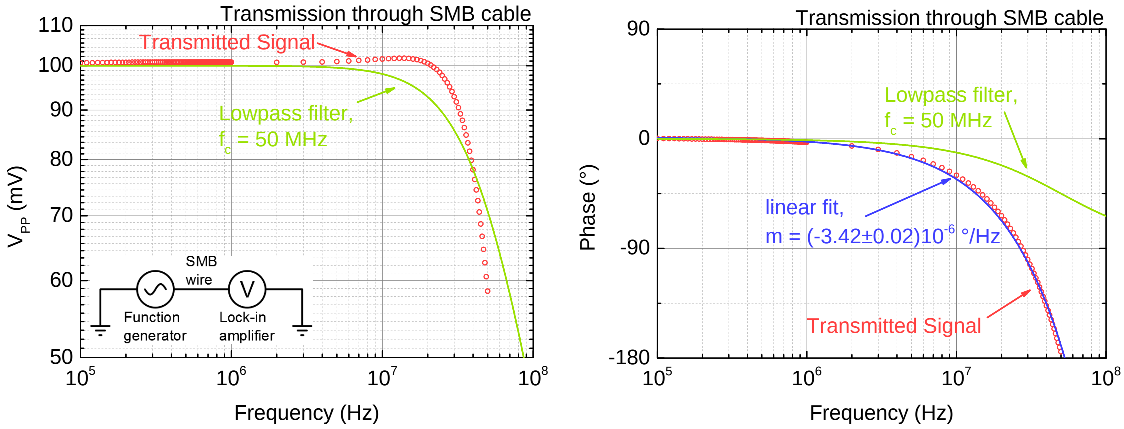

(a) Magnitude of the transmitted voltage signal (b) Phase of the transmitted voltage

Figure 4.4: (a) Bode diagram for the transmission of a peak to peak voltage of $100\,\mathrm{mV}$ through a coaxial cable. The equivalent circuit is drawn in the inset. This measurement provides information about the high frequency characteristics of the measurement setup. For frequencies up to $20\,\mathrm{MHz}$ the transmitted signal is almost unattenuated. At higher frequencies, the voltage is attenuated and a phase shift can be observed. The phase shift (panel (b)) is caused by the finite signal speed. For comparison, the Bode diagram for a low pass filter of first order is drawn as well.

detection electronics a phase of

$$\Delta\varphi = \Delta\omega \cdot t = 2\pi \cdot \Delta f \cdot t$$

builds up. Thus, by changing the modulation frequency f, the phase of the recorded voltage signal is affected. The transmission time t of the signal through the cable is independent of the modulation frequency[3]. To confirm this dependence, a linear function was fitted to the data in Fig. 4.4(b). The theoretical curve (blue) is in good agreement with the measured data.
In addition to the measured data, the frequency response of a low pass filter of first order with a cutoff frequency of $f_c = 50\,\mathrm{MHz}$ is plotted in Fig. 4.4, since $50\,\mathrm{MHz}$ is the maximum operation frequency of the Lock-in amplifier. At frequencies close to or higher than f_c there is a notable disagreement between the signal response expected for such a filter and the actually recoded data. This indicates, that a simple low pass filter is not a good model to describe the high frequency behavior

[3]The frequency of the laser light f_{Laser} will not be changed for the experiments.

of the lock-in amplifier. In addition, the phase shift of a low pass filter is is a constant for $f \gg f_\mathrm{c}$ ($\Delta\phi = 90°$), while only the linear shift due to the finite signal velocity is observed here.
In conclusion, the lock-in amplifier works well for frequencies smaller than 30 MHz. For higher frequencies, the voltage magnitude is attenuated, however, a simple low pass filter can not accurately describe the observed behavior. The phase on the other hand is still constant. A phase shift could only be observed due to the finite speed of the electromagnetic waves in the cable. In measurements of the spin Seebeck effect, it will be important to correct for this phase shift by subtracting a linear function.

4.3 Time resolved measurements

In this section, time dependent measurements of the spin Seebeck effect will be discussed. The setup is sketched in Fig. 4.5. It is different from the setup discussed in Fig. 4.1, since now the modulation frequency f_mod of the laser is changed in addition to the position of the laser spot on the sample surface. Still a lock-in amplifier is used for the detection of the ac spin Seebeck voltage.
The transmission characteristic of the experimental setup is drawn as an equivalent circuit diagram in Fig. 4.5. Due to the resistance R and shunt capacitance C introduced by the sample and the wiring, respectively, the circuit can be modeled as an RC low pass filter. Applying Kirchhoff's laws, the differential equation, describing the low pass filter is found as

$$RC\frac{\mathrm{d}V_\mathrm{SSE}}{\mathrm{d}t} + V_\mathrm{SSE} = V_{0,\,\mathrm{SSE}}. \tag{4.5}$$

$V_{0,\,\mathrm{SSE}}$ is the generated spin Seebeck voltage, while V_SSE is the voltage, which can be measured, due to low pass filtering.

4.3.1 Frequency map

Figure 4.6 shows false color plots of transient spin Seebeck effect measurement. The data were recoded by scanning the laser spot across the Hall bar in the y-direction (*cf.* Fig. 4.5) at fixed laser modulation frequencies f_mod. The Hall bar is located

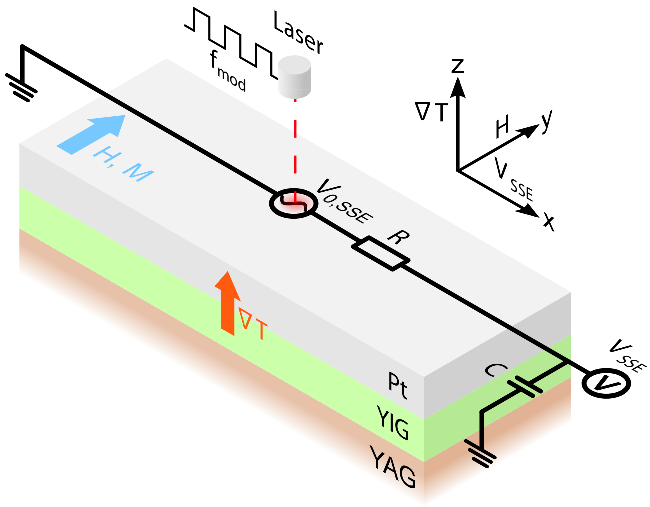

Figure 4.5: For the transient spin Seebeck effect measurements, an intensity modulated laser is used in order to induce a time dependent temperature gradient ∇T across the YIG/Pt interface. An external magnetic field is applied perpendicular to the measurement direction and the temperature gradient ∇T. The generated spin current is converted into a charge current in the Pt layer. This charge current causes a potential difference at both ends of the Hall bar due to the open circuit geometry. After preamplification, the voltage is detected with a lock-in amplifier. In addition an equivalent circuit diagram for the measurement circuit is sketched. This circuit diagram indicates, that the measurements are limited by RC lowpass behavior.

between $y = 50\,\mu\mathrm{m}$ and $y = 130\,\mu\mathrm{m}$. After each scan, the frequency was increased and the same line (along y) was scanned again. The frequency range is $10\,\mathrm{kHz}$ to $50\,\mathrm{MHz}$. In order to visualize the data processing, the raw data for one field direction ($B = 70\,\mathrm{mT}$) and both voltage channels of the lock-in amplifier is plotted in Fig. 4.6(a) and Fig. 4.6(b).
In the low frequency range ($\lesssim 1\,\mathrm{MHz}$) a clear spin-Seebeck signal can be seen in the x-channel voltage, indicated by a blue rectangle, which has the y dimension of the Pt-bar (Fig. 4.6(a)). The signal decays for frequencies $\gtrsim 1\,\mathrm{MHz}$. This can be explained by a phase shift, since a spin Seebeck voltage is measured in the y-channel for frequencies $1\,\mathrm{MHz} \lesssim f_{\mathrm{mod}} \lesssim 8\,\mathrm{MHz}$ (red patch in Fig. 4.6(b)). For even higher frequencies ($\gtrsim 5\,\mathrm{MHz}$), this voltage signal is superimposed by resonances in both channels.

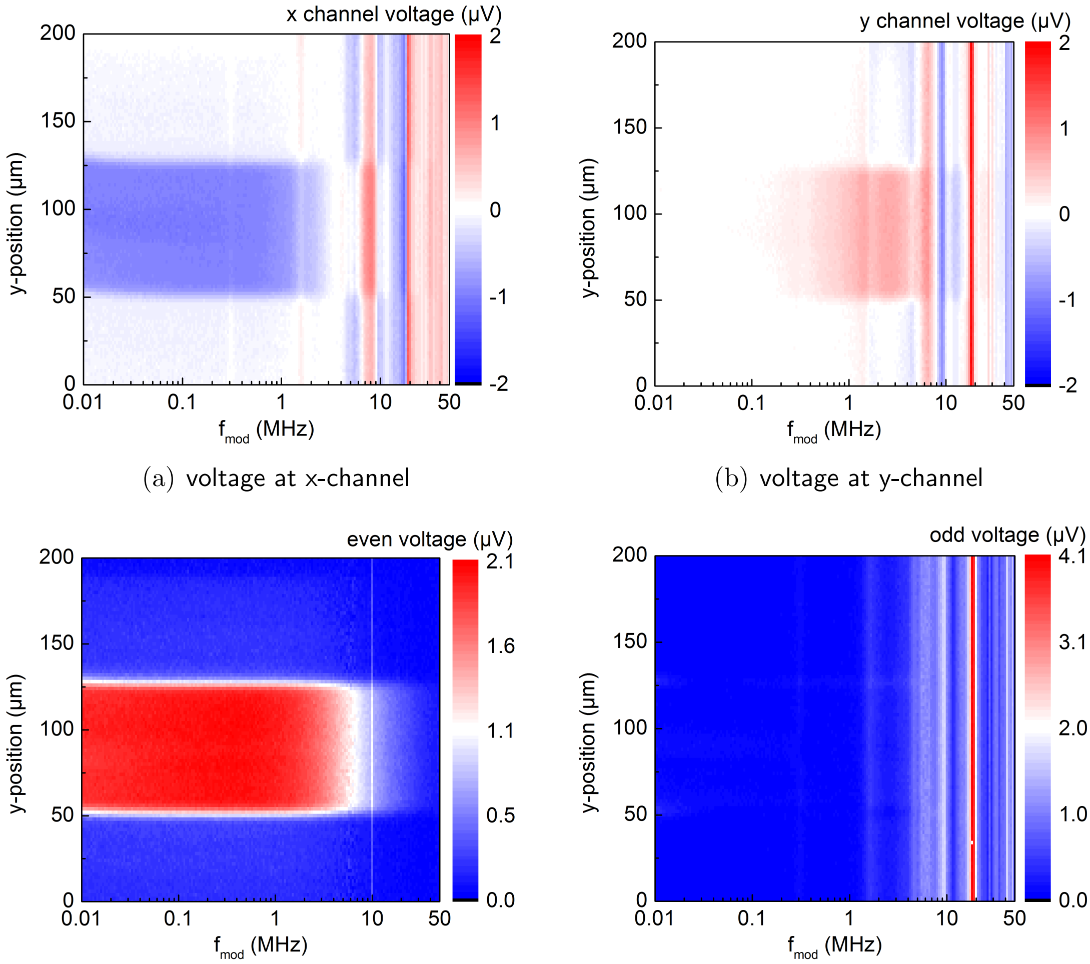

(a) voltage at x-channel

(b) voltage at y-channel

(c) even voltage signal

(d) odd voltage signal

Figure 4.6: Frequency dependent measurements of the spin Seebeck voltage on the sample YIG(61)/Pt(19.5). At a fixed modulation frequency f_{mod} the sample was scanned along a $200\,\mu\mathrm{m}$ long line in y-direction. After each line scan, the frequency was increased and the procedure repeated. The Pt layer is located between $y = 50\,\mu\mathrm{m}$ and $y = 130\,\mu\mathrm{m}$. In panel (a) and (b), the raw signal of the lock-in amplifier is plotted (x-channel voltage and y-channel voltage respectively). The even voltage (panel (c)) on the Pt stripe stays constant up to $f_{\mathrm{mod}} \approx 1\,\mathrm{MHz}$ and decays for higher frequencies due to the RC low pass behavior of the measurement circuit. In the odd voltage, only resonances are evident.

In order to get rid of the resonances, the even and the odd part of the signal have to be calculates. Here, we use a modified version of Eq. (4.4) to account for the frequency dependent phase of the measured signal:

$$V_{\text{even}} := \sqrt{(V_x(-B) - V_x(+B))^2 + (V_y(-B) - V_y(+B))^2}. \tag{4.6}$$

By using Eq. (4.2) and (4.1), this expression can be simplified and identified with the spin Seebeck voltage, defined in Eq. (4.4):

$$V_{\text{SSE}} = \sqrt{(2V_{\text{ISH}})^2 \cdot \cos^2(x) + (2V_{\text{ISH}})^2 \cdot \sin^2(x)} \tag{4.7}$$

$$= 2|V_{\text{ISH}}|. \tag{4.8}$$

V_{even} thus only contains the spin Seebeck voltage after this operation. The resonances do not depend on the magnetic field and thus cancel out. Consequently, V_{even}, plotted in Fig. 4.6(c) does not show resonances. Instead, one can see a high voltage of about 2 µV, when the laser spot hits the Pt layer. Next to the Pt, the generated voltage is at least one order of magnitude smaller. This voltage is constant for frequencies $\lesssim$ 3 MHz. For higher frequencies, the voltage signal decays. This decay is attributed to the lowpass behavior of the measurement circuit, as discussed in Sec. 4.3.2.

On the other hand, it is also possible to calculate the odd voltage signal:

$$\begin{aligned} V_{\text{odd}} &= \sqrt{(V_x(-B) + V_x(+B))^2 + (V_y(-B) + V_y(+B))^2} \\ &= 2|V_{\text{para}}| \,. \end{aligned}$$

After performing this operation, the spin Seebeck voltage will cancel out, while signals which do not depend on the magnetic field remain. Figure 4.6(d) confirms that only the resonances, which were already seen in the raw signal, appear in the odd signal.

4.3.2 Spin Seebeck effect in the frequency domain

To gain a better understanding of the voltage attenuation as a function of f_{mod}, observed in Fig. 4.6, the frequency dependence is measured at one fixed position at the center of the Hall bar for different samples. The results are plotted in Fig. 4.7. For the samples YIG(48)/Pt(4.9) and YIG(61)/Pt(19.5), the even voltage V_{SSE} is constant up to a certain cutoff frequency f_{c} and attenuated for higher frequencies. In addition, a phase shift of $-90°$ can be observed for high frequencies.
As mentioned above, this behavior can be explained with a low pass filter model as given by Eq. (4.5). This equation can be solved by performing a Laplace transformation ($V(t) = 0 \; \forall \; t \leq 0$):

$$RC\frac{\mathrm{d}V_{\mathrm{SSE}}(t)}{\mathrm{d}t} + V_{\mathrm{SSE}}(t) = V_{0,\,\mathrm{SSE}}(t) \quad \circ\!\!-\!\!\bullet \quad RC(sV_{\mathrm{SSE}}(s)) + V_{\mathrm{SSE}}(s) = V_{0,\,\mathrm{SSE}}(s),$$

The transfer function is given by:

$$\mathrm{H}(s) = \frac{V_{\mathrm{SSE}}(s)}{V_{0,\,\mathrm{SSE}}(s)} = \frac{1}{1 + RCs}.$$

This transfer function has a pole at $s = -1/RC$. The cutoff frequency is defined as the frequency, where half of the unfiltered voltage signal is attenuated. For a low pass filter, the following cutoff frequency is obtained:

$$f_{\mathrm{c}} = \frac{\omega_{\mathrm{c}}}{2\pi} = \frac{1}{2\pi RC}. \tag{4.9}$$

The gain of a low pass filter is given by the absolute value of the transfer function. Using $s = \mathrm{j}\omega$ and $f = 2\pi \cdot \omega$, it follows:

$$G(\omega) = |\,\mathrm{H}(\mathrm{j}\omega)| = \frac{1}{\sqrt{1 + (RC\omega)^2}} = \frac{1}{\sqrt{1 + (f/f_{\mathrm{c}})^2}}. \tag{4.10}$$

Finally, the phase can be calculated [59]:

$$\varphi = \arctan\left(\frac{\mathrm{Im(H)}}{\mathrm{Re(H)}}\right) = \arctan(-RC\omega) = -\arctan\left(\frac{f}{f_{\mathrm{c}}}\right). \tag{4.11}$$

In the following, the even voltages as calculated with Eq. (4.6), containing only the spin Seebeck signal V_{SSE}, are discussed. The odd voltages are artifacts from the

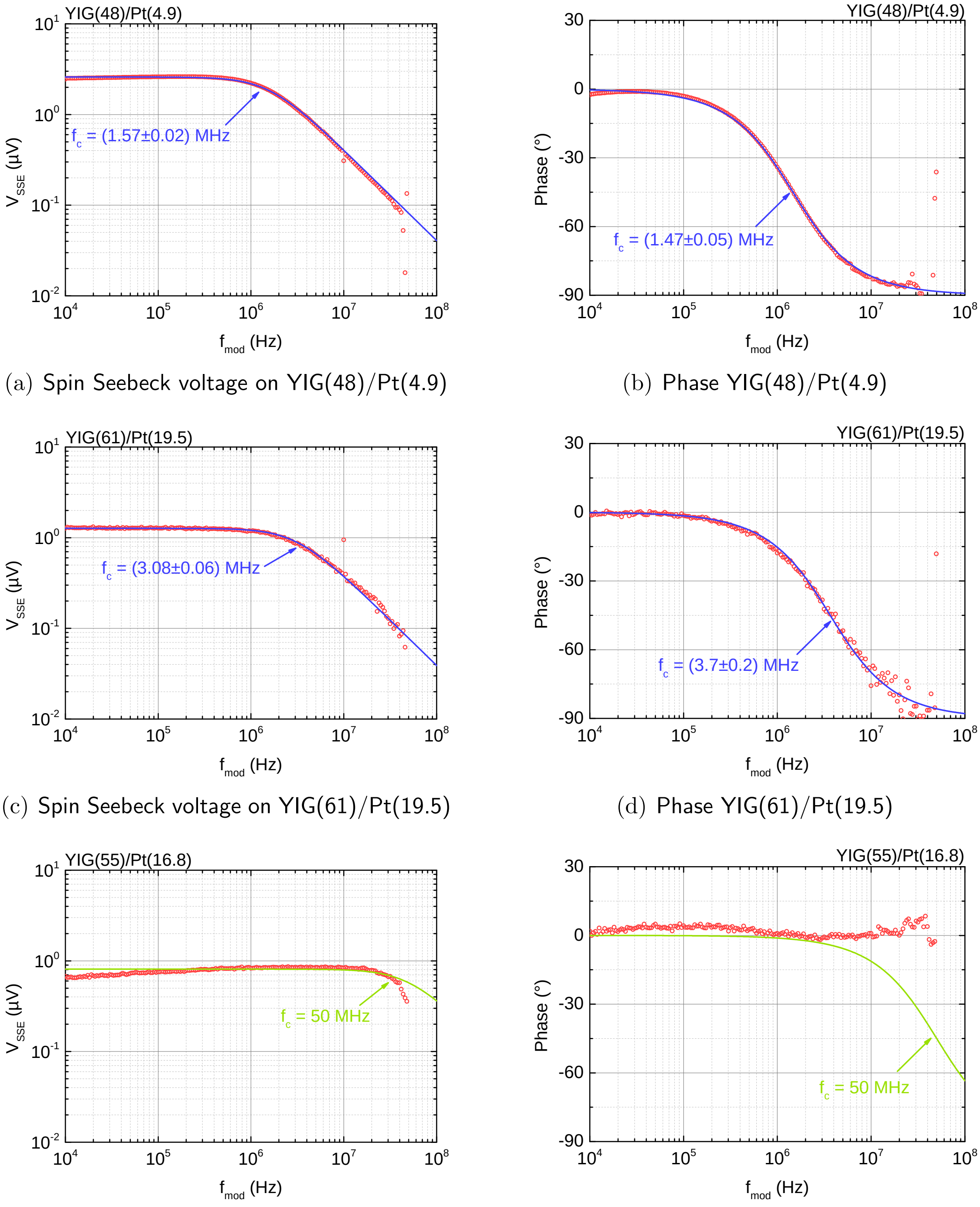

(a) Spin Seebeck voltage on YIG(48)/Pt(4.9)

(b) Phase YIG(48)/Pt(4.9)

(c) Spin Seebeck voltage on YIG(61)/Pt(19.5)

(d) Phase YIG(61)/Pt(19.5)

(e) Spin Seebeck voltage on YIG(55)/Pt(16.8)

(f) Phase YIG(55)/Pt(16.8)

Figure 4.7: Bode diagramms for the spin Seebeck voltage as a function of the modulation frequency f_{mod}, measured at a fixed position of the laser spot on the Pt layer. For the samples YIG(49)/Pt(4.9) and YIG(61)/Pt(19.5), the frequency characteristics can be explained with a lowpass filter model. On the sample YIG(55)/Pt(16.8), no characteristic cutoff is identifiable. The red circles represent the measured data while the solid lines are a fit to the lowpass model.

Sample	$f_c^{\mathrm{Magnitude}}$ (MHz)	f_c^{Phase} (MHz)	R (Ohm)	C_{exp} (pF)
YIG(48)/Pt(4.9)	1.57 ± 0.02	1.47 ± 0.05	876.4	119 ± 3
YIG(61)/Pt(19.5)	3.08 ± 0.06	3.7 ± 0.2	308.8	152 ± 6

Table 4.1: Summary of the cutoff frequencies for both RC limited samples. The cutoff frequency of the sample YIG(55)/Pt(16.8) can not be estimated, since it is above the frequency range of the lock-in amplifier (50 MHz). In addition, the resistances of the samples are given. This allows to calculate the capacitance of the equivalent RC circuit.

circuitry and do not provide any insight to τ_{mp}. Figure 4.7(a) and 4.7(c) show the frequency-amplitude characteristic (V_{SSE} vs. f_{mod}) of the samples YIG(48)/Pt(4.9) and YIG(48)/Pt(19.5) respectively. In both cases, the voltage is constant for low frequencies ($\lesssim 1\,\mathrm{MHz}$), but attenuated with a roll off of $-20\,\mathrm{dB/dec}$ at higher frequencies. This roll off is characteristic for a low pass filter of first order [59]. Fitting the model in Eq. (4.10) to the aforementioned experimental data [solid line in Fig. 4.7(a) and Fig. 4.7(c)] yields an excellent agreement with the observed behavior. Note that the fit contains the cut off frequency f_{c} as the only fitting parameter. The phase response of the spin Seebeck effect plotted in Fig. 4.7(b) and 4.7(d) is corrected for the phase shift due to the finite propagation speed of light in the cables. To this end, a linear function was fitted to the data in a range, where the low pass induced phase shift (*cf.* Eq. (4.11)) is almost constant ($f \gg f_{\mathrm{c}}$). The linear function was then subtracted from the original data to get the result presented in Figs. 4.7(b), 4.7(d) and 4.7(f). The phase response of a low pass filter (*cf.* Eq. (4.11)) was fitted to the data and plotted as well (once again, f_{c} being the only fitting parameter). As in the discussion of the frequency-amplitude characteristics, the results of theory and experiment match well for the frequency-phase response. The results for the different samples are summarized in Tab. 4.1. Using Eq. (4.9), it is possible to calculate the corresponding capacitance of the detection circuit, since the sample resistance is known. We obtain a common capacitance of $C = (136 \pm 5)\mathrm{pF}$, consistent with typical shunt capacitances of SMB and BNC cables [8, 79].

The conclusion drawn from the experiments depicted in Fig. 4.7(a) to 4.7(d) is that the cutoff is caused by electric circuitry (the resistance of the sample and the capacitance of the wiring act as a low pass filter) alone. In other words, the cutoff is not intrinsic to the spin Seebeck effect. This means that the relevant timescale

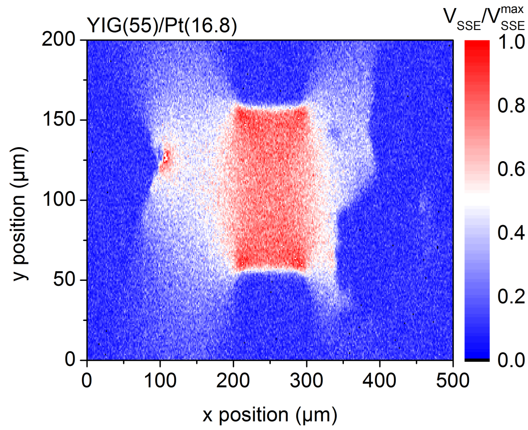

Figure 4.8: Spatially resolved false color V_{SSE} image of a YIG/Pt pattern with $47\,\Omega$ resistance. The pattern is composed of two contact pads for bonding, connected with a small bridge of $100\,\mu\mathrm{m} \times 100\,\mu\mathrm{m}$. The red areas in the image indicate this bridge. When the bridge is hit by the laser, a voltage is measured. Only a low voltage is measured on the contact pads due to geometric factors and short circuiting, as discussed in [82].

for the interaction between e.g. magnons and phonons in the spin Seebeck effect is shorter than $\approx 3\,\mathrm{MHz}$.

In order to probe the dynamics of the spin Seebeck effect in a higher frequency range, a new sample pattern was designed, in collaboration with Michael Schreier. to reduce the sample resistance and thus obtain a higher electrical cutoff (*cf.* Eq. (4.9)). The new design is composed of two contact pads for bonding and a small bridge of $100\,\mu\mathrm{m} \times 100\,\mu\mathrm{m}$ lateral dimension, connecting both contact pads. Figure 4.8 shows a spatially resolved V_{SSE} false color image of the structure. The red bar in this image corresponds to the bridge. By decreasing the effective length and increasing its width, the new Pt bar's resistance is decreased to $47\,\Omega$. With $C = 140\,\mathrm{pF}$, this yields a cutoff frequency of $f_{\mathrm{c}} = 24\,\mathrm{MHz}$. However it has to be mentioned, that also the capacitance of the measurement setup changed, since a different preamplifier and different cables were used.

Figure 4.7(e) shows the amplitude frequency response of this sample. While a comparison with the expected signal attenuation of a low pass filter with $f_{\mathrm{c}} = 50\,\mathrm{MHz}$ (the -3dB frequency of the lock-in amplifier) yields reasonable agreement up to $f_{\mathrm{mod}} \approx 40\,\mathrm{MHz}$, the phase [Fig. 4.7(f)] behaves notably different. More precisely, the measured phase is flat throughout the entire measurement range and thus ex-

cludes a low pass based origin of the amplitude attenuation. Since furthermore, an attenuation of the recorded voltage above 40 MHz was already observed in previous transmission experiments [Fig. 4.4(a)], the attenuation is most likely caused by the lock-in amplifier. Of course the low pass model still holds for the measurements in Fig. 4.7(a) to Fig. 4.7(d), since the sample resistance was significantly higher here and thus a cutoff was observed at much lower frequencies, where no features could be observed in the aforementioned transmission measurements [Fig. 4.4(a)].
No cutoff was observed at the frequency $f_{\text{mod}} = 24\,\text{MHz}$, calculated above, because a different preamplifier was used as well as different cables. This changes the capacitance of the measurement circuit.
In conclusion, no intrinsic spin Seebeck effect cutoff could be observed in the experimentally accessible measurement range of 50 MHz. This means that the magnon-phonon interaction time relevant for the SSE in our samples must be shorter than $\tau_{\text{mp}} = 1/(2\pi 50\,\text{MHz}) = 3.2\,\text{ns}$.

4.3.3 Resonances in the setup

As discussed in Sec. 4.3.1, resonances can be observed in the measured signals for large frequencies f_{mod}. To identify the source of these resonances, a comparison between the measured signal with and without laser illumination was performed. Figure 4.9(a) shows the even and odd signal of a spin Seebeck effect measurement under laser illumination. For the measurement, the position of the laser spot on the Hall bar was kept constant, while the frequency was swept from $f = 10\,\text{kHz}$ to $f = 50\,\text{MHz}$. Again, the even signal shows spin Seebeck voltage with the typical low pass behavior, related to the sample resistance and the capacitance of the cables. The odd signal on the other hand does show resonances. The amplitude of these resonances increases with increasing frequency.
For the measurements in Fig. 4.9(b), all conditions were kept the same, only the laser beam was blocked with a piece of paper, such that the laser light does not reach the sample. The result is, that the spin Seebeck effect voltage vanished (even signal). The noise in the even signal is two orders of magnitude smaller than the spin Seebeck signal with the laser light illuminating the sample. However, the odd signal did not changed owing to the blocked laser. Thus, the resonances are not induced by the laser light, but are due to some electrical feedback or cross-talk in the experimental setup.

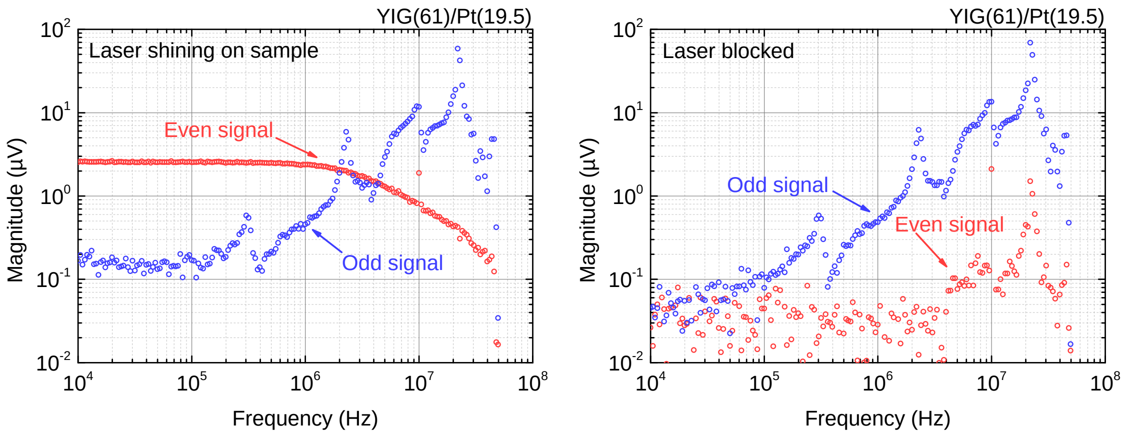

(a) Laser shining on sample.

(b) Laser blocked.

Figure 4.9: Frequency dependence of the even and odd parts of the recorded voltage with (a) and without (b) laser illumination. For the measurements the laser spot was kept at one fixed position of the Hall bar, while the modulation frequency of the laser was changed. Under laser illumination, low pass behavior can be seen in the even signal. In the odd signal, resonances appear, as discussed earlier. By physically blocking the laser beam the experimental conditions remain identical to the previous measurement, however, now only the resonances can be observed in the odd signal while the spin Seebeck signal in the even part vanishes.

4.3.4 Spin Seebeck effect in the time domain

The measurements discussed so far were performed using a lock-in amplifier. The lock-in technique is an integrating technique and yields the averaged signal over several periods. The disadvantage of this approach is that the information about the exact shape of the recorded signal is lost. For this reasons, measurements in the time domain were performed, using a high speed digitizing card (*Gage Razor*). As shown earlier, the characteristic voltage response recorded in the experiments can be described with a low pass filter model. Assuming a perfect, square wave like response of the spin Seebeck voltage to the laser heating Eq. (4.5) can be written as

$$RC\frac{\mathrm{d}V_{\mathrm{SSE}}(t)}{\mathrm{d}t} + V_{\mathrm{SSE}}(t) = V_0 \cdot \sum_{n=0}^{\infty}(-1)^n \, \Theta\left(t - \frac{n}{2f_{\mathrm{mod}}}\right). \tag{4.12}$$

Here $\Theta(t)$ is the Heaviside step function and f_{mod} is the modulation frequency of the laser. Note that the representation of the square wave via a sum of Heaviside functions simplifies the calculations as compared to a representation via a Fourier series. To solve Eq. (4.12), a Laplace transformation is applied ($V(t) = 0 \; \forall \; t \leq 0$):

$$RCs \cdot V_{\text{SSE}}(s) + V_{\text{SSE}}(s) = V_0 \cdot \sum_{n=0}^{\infty} (-1)^n \frac{e^{-\frac{ns}{2f_{\text{mod}}}}}{s} \tag{4.13}$$

$$\Rightarrow V_{\text{SSE}}(s) = V_0 \cdot \sum_{n=0}^{\infty} (-1)^n \frac{e^{-\frac{ns}{2f_{\text{mod}}}}}{s(RCs+1)}. \tag{4.14}$$

The solution in the time domain can now be obtained by applying a Laplace back transformation to Eq. (4.14):

$$V_{\text{SSE}}(t) = V_0 \cdot \sum_{n=0}^{\infty} (-1)^n \left(1 - e^{-\frac{1}{RC}\left(t - \frac{n}{2f_{\text{mod}}}\right)}\right) \theta\left(t - \frac{n}{2f_{\text{mod}}}\right). \tag{4.15}$$

Since f_{mod} is known, the solution (Eq. 4.15), contains only two free parameters for fitting, namely RC and V_0. Therefore, by using Eq. (4.9), f_{c} can be calculated from the RC value obtained via a measurement in the time domain as well. The advantage of this solution is that a full period is described analytically by only two summands as compared to a Fourier based solution which is always an approximation.

The measurement results are plotted in Fig. 4.10. For the measurement, the laser spot position was kept constant in the middle of the Hall bar. However, in contrast to the previous measurements, also the frequency was kept constant, while the voltage was recorded as a function of the time with a *Gage Razor* digitizing card. The digitizer card records the voltage with a sampling of 200 MSample/s. Due to this high data acquisition rate, the signal could be averaged heavily ($\approx 10^6$) to reduce the noise level.

The time traces for a modulation frequency of $f_{\text{mod}} = 200\,\text{kHz}$ on the 3 different samples (Fig. 4.10(a), Fig. 4.10(c) and Fig. 4.10(e)) are well described by a square wave, as expected for a square wave excitation (laser switched on/off). Equation 4.15 is fitted to the data in order to determine the cutoff frequency. The agreement between fit and measured data is excellent.

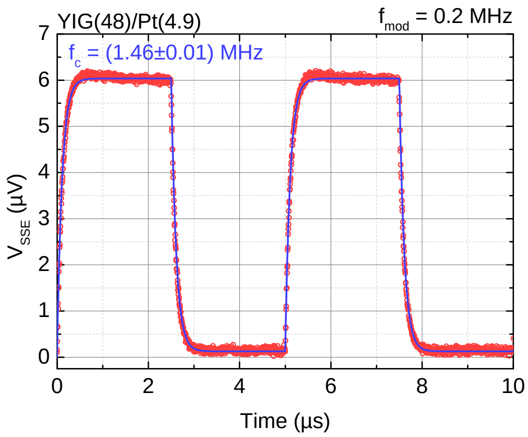

(a) YIG(48)/Pt(4.9), $f_{\text{mod}} = 200\,\text{kHz}$

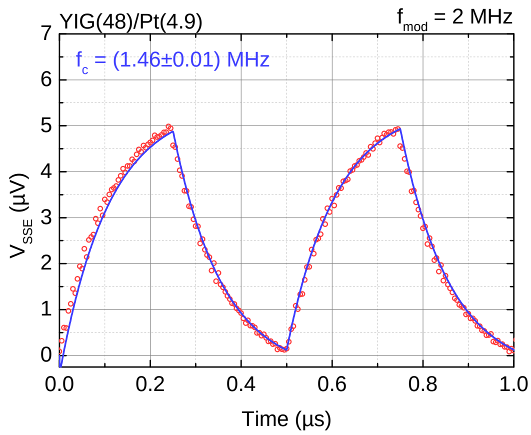

(b) YIG(48)/Pt(4.9), $f_{\text{mod}} = 2\,\text{MHz}$

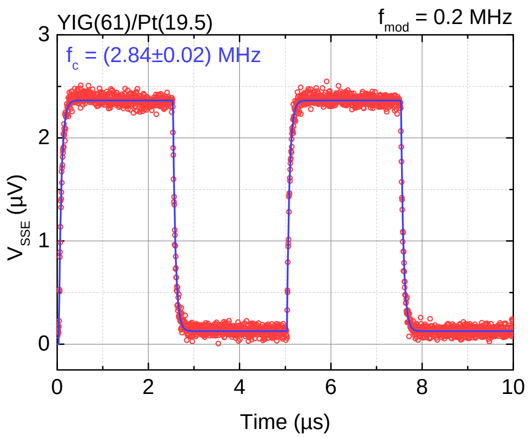

(c) YIG(61)/Pt(19.5), $f_{\text{mod}} = 200\,\text{kHz}$

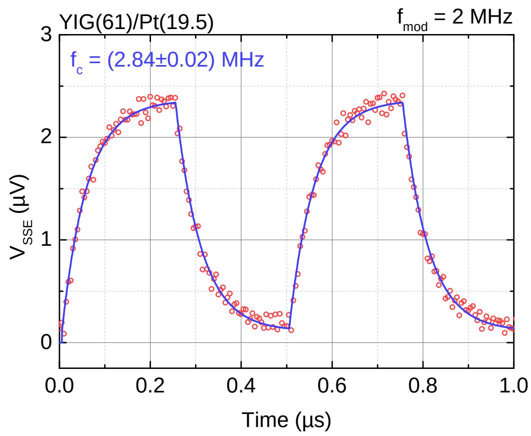

(d) YIG(61)/Pt(19.5), $f_{\text{mod}} = 2\,\text{MHz}$

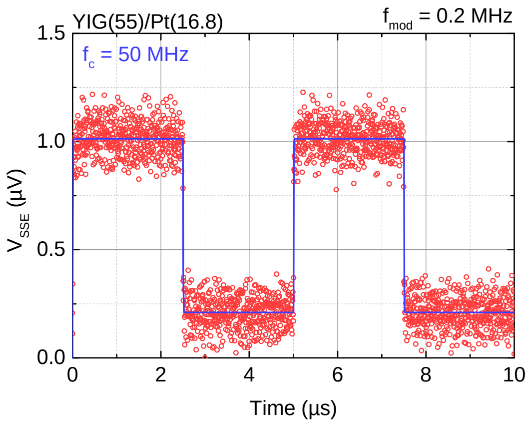

(e) YIG(55)/Pt(16.8), $f_{\text{mod}} = 200\,\text{kHz}$

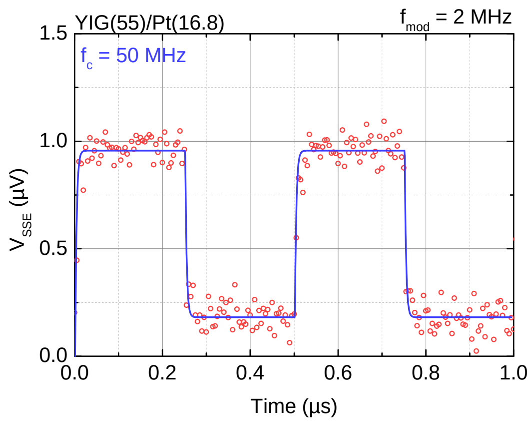

(f) YIG(55)/Pt(16.8), $f_{\text{mod}} = 2\,\text{MHz}$

Figure 4.10: Spin Seebeck voltage measured as a function of the time for laser intensity modulation frequencies of $200\,\text{kHz}$ and $2\,\text{MHz}$ in the three different sample structures. The laser spot was kept at one fixed position during the measurement. Additionally the voltage response of a low pass filter was fitted to the data. This allows to determine the $-3\,\text{dB}$ cutoff frequency f_{c}.

For a laser intensity modulation frequency of $f_{\mathrm{mod}} = 2\,\mathrm{MHz}$ the measured voltage response looks shark fin like on the samples YIG(48)/Pt(4.9) (Fig. 4.10(b)) and YIG(61)/pt(19.5) (Fig. 4.10(d)). This behavior is well explained by the low pass behavior of the measurement circuit. The slow rise in signal can be compared to the process of a charging capacitor, while the decrease in signal corresponds to a discharging one.
As shown in Sec. 4.3.2, the sample YIG(55)/Pt(16.8) is not RC limited in the investigated frequency range. Consequently, the time trace at $f_{\mathrm{mod}} = 2\,\mathrm{MHz}$ (Fig. 4.10(f)) is still square wave like. As a guide for the eye, the time trace of a low pass filter with a cutoff of $f_{\mathrm{c}} = 50\,\mathrm{MHz}$ was plotted. With the given sampling rate of the digitizing card, it is not possible to determine an exact value of the cutoff frequency. However, the statement, that the cutoff is above 50 MHz agrees with the data of this experiment.

4.4 Conclusions

As discussed in Sec. 4.1, the dynamics of the spin Seebeck effect is presumably limited by the magnon-phonon interaction time. The magnon-phonon interaction time for the uniform precession mode ($k = 0$) in bulk YIG samples at room temperature has been measured in ferromagnetic resonance experiments. *Spencer et al.* determined an interaction time of the order of a few 100 ns [90]. If the spin Seebeck effect is driven at frequencies exceeding $f_{\mathrm{mod}} = 1/(2\pi\tau_{\mathrm{mp}}) \approx 1\,\mathrm{MHz}$, a characteristic change in the spin Seebeck voltage should be measured, provided that small wavenumber magnons are dominant for the spin Seebeck effect. The reason for this change is, that the magnons can not equilibrate with the phonons on this short time scales and thus the temperature difference ΔT_{me} between electrons in the normal metal and magnons in the ferrimagnetic insulator will be affected.
In this chapter, time dependent measurements were discussed, performed with a lock-in amplifier (Sec. 4.3.2) and a high speed digitizing card (Sec. 4.3.4). Neither of these measurements showed any intrinsic spin Seebeck effect cutoff below $f_{\mathrm{mod}} = 50\,\mathrm{MHz}$. The observed features could be attributed to RC low pass behavior of the measurement circuit. This suggests, that the spin Seebeck effect is robust in the investigated frequency range. Consequently, the magnon-

phonon interaction time relevant for the spin Seebeck effect must be shorter than $\tau_{\mathrm{mp}} = 1/(2\pi f_{\mathrm{mod}}) = 3\,\mathrm{ns}$ in our samples.
This experimentally obtained interaction time is by two orders of magnitude smaller than conventionally assumed in the corresponding spin Seebeck effect literature [18, 106]. Therefore it is concluded, that small wavenumber magnons do not play an important role for the spin Seebeck effect. Rather the full magnon spectrum has to be considered in which "hot", thermal magnons with much smaller τ_{mp} dominate the angular momentum transport. Hereby it is assumed that τ_{mp} in thin film samples is comparable to the value in bulk samples. Nevertheless, similar conclusions were recently suggested in theoretical publications. [74, 83, 94].
While τ_{mp} is certainly the limiting experimental time constant for the SSE, the magnon-magnon interaction time τ_{mm} could be relevant as well. Most notably, recent SSE theories assume τ_{mm} *to be smaller than* τ_{mp} [14, 37, 74, 94, 106]. In literature, values for the magnon-magnon interaction time are widely spread from 10 µs to 1 ns [19, 51, 108, 109]. Since the spin Seebeck voltage was constant up to $\tau = 3\,\mathrm{ns}$ in the experiments described in this section, the magnon-magnon interaction time is likely to be towards to short end of this range.
Lately, *Agrawal et al.* reported time dependent spin-Seebeck effect measurements as well [5]. Similar to the experiment discussed in this section, they use an intensity modulated laser to apply a transient temperature gradient to YIG/Pt samples. However they found a time constant of $\tau = 343\,\mathrm{ns}$, which they claim, is intrinsic to the spin Seebeck effect.
It has to be noted that their experiments were carried out on a much thicker YIG film of 6.7 µm. This could be the reason for a different time constant, because the spin Seebeck effect might depend on the YIG film thickness due to a finite magnon propagation length [46]. Only magnons within a certain distance away from the YIG/Pt interface, can contribute to the spin Seebeck effect. For faster modulation frequencies, this distance becomes smaller, which leads to a cutoff, since less magnons can contribute to the spin Seebeck effect. On the other hand, if the YIG film is thinner than the aforementioned traveling distance, a cutoff due the bulk dependence of the spin Seebeck effect can not be observed.
However, within the model proposed by Agrawal *et al.*, a cutoff at $f_{\mathrm{c}} < 3\,\mathrm{MHz}$, corresponding to a time constant of $\tau > 50\,\mathrm{ns}$, would be expected for the samples used in this thesis with a YIG thickness of 50 nm. This is in contrast to results,

presented in this chapter, which show a constant voltage signal on much shorter timescales. Nevertheless, it might be worth to perform the measurements presented in this section with samples of different YIG thickness in order to test, whether the dynamics of to spin Seebeck effect depends on the YIG thickness.

5 Current driven spin Seebeck effect

While transient spin Seebeck measurements, as presented in the previous chapter, provide valuable insight into the dynamics of spin caloric processes, the steady state spin Seebeck effect is still not fully understood. One major challenge for all spin Seebeck experiments is a quantitative control or knowledge over the temperature gradient and the sample (base) temperature. To this end a very simple measurement scheme was developed at the WMI [20], which not only allows good control over and direct access to the thermal gradient but is also easy to integrate into standard magneto-transport cryostats.
In the beginning of this chapter, the experimental setup, where the temperature gradient in YIG/Pt is generated and probed on-chip by a current through the normal metal layer, will be introduced.
The current driven spin Seebeck effect setup was used to measure the spin Seebeck effect as a function of the magnetic field and the temperature in YIG/Pt hybrid structures. All results, obtained with this new measurement technique will be compared to results, where the temperature gradient was established with laser heating.
Finally, the evolution of the spin Seebeck effect as a function of magnetic fields orientation will be discussed. Here, special features are observed, which can be attributed to the Oersted field, generated by the current through the platinum layer.

5.1 Motivation

As mentioned before, it is essential to create a temperature gradient across a metal/ ferrimagnetic insulator interface for measurements of the spin Seebeck effect. In literature different approaches can be found to create the temperature gradient. One approach uses heat reservoirs (for example Peltier elements or resistive heaters attached to Cu blocks) of different temperature at both sides of the sample [4, 40, 48, 62, 71, 96–98]. Good thermal coupling between the Cu blocks and the sample is necessary for large temperature gradients at the normal metal/ ferromagnetic insulator interface. On the other hand, the heat reservoir has to be electrically insulated from the normal metal layer to avoid short circuiting of the spin Seebeck voltage. For that reason, a small sapphire sheet [62] or thin silicone rubber [100] is inserted between the heat reservoir and the sample, which causes an additional drop in temperature and thus directly affects the actual gradient across the normal metal/ ferromagnet interface. Another possibility to establish a temperature gradient across the normal metal/ ferromagnetic insulator interface is laser heating [5, 77, 102, 103]. This technique is described in detail in Sec. 4.2. While laser heating suits well for dynamic and spatially resolved measurements of the spin Seebeck effect, it has also some disadvantages. The temperature gradient caused by laser heating is only accessible via numerical simulations [83][1], and optics are generally challenging to integrate into cryostats. However, only a magnet cryostat provides the environment for measurements at low temperatures or measurements in high fields.

In this chapter, a third setup for spin Seebeck experiments will be discussed: The current driven spin Seebeck effect [84]. A current is sourced through the normal metal layer, inducing Joule heat [16, 69]. At the same time, the resistance of the normal metal is monitored for on chip thermometry [75]. The setup is simple, since no additional heater (Peltier elements or laser) is needed in order to establish the temperature gradient. Most conventional magneto-transport setups can therefore be used without any modifications for spin Seebeck effect measurements at low temperatures or in high fields.

[1] In experiments, where heat reservoirs are used for creation of the temperature gradient, the temperature gradient can be estimated, at least roughly, from the temperatures of the heat reservoirs.

5.2 Experimental setup

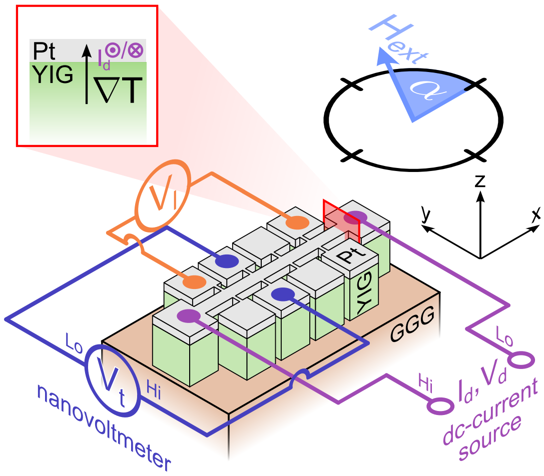

Figure 5.1: Sketch of the experimental setup for measurements of the current driven spin Seebeck effect. A Hall bar structure is patterned into a YIG/Pt bilayer on a substrate (YAG or GGG). The current I_{d} is sourced through the long stripe of the Hall bar. This induces a temperature gradient perpendicular to the YIG/Pt interface, along z (inset). An external magnetic field H_{ext} is applied in the sample plane while the transversal voltage V_{t}, and the longitudinal voltage V_{l} are measured. The spin Seebeck effect is detected via V_{t} and V_{l} is recorded for 4 terminal resistive measurements.[2]

The experimental setup is shown in Fig. 5.1. As in chapter 4, YIG(d_1)/Pt(d_2) samples were used for all measurements (d_n denotes the layer thickness), patterned into Hall bar mesa structures. A dc current I_{d} is pulled through the long strip of the Hall bar for heating, using a *Keithley K2400 Sourcemeter*, thereby generating a uniform temperature gradient ∇T at the Hall bar body, perpendicular to the YIG/Pt interface. As explained earlier in this thesis, recent spin Seebeck theories assume, that the spin Seebeck voltage is directly proportional to the difference ΔT_{me} in electron temperature in the normal metal and the magnon temperature in the ferrimagnetic insulator [106]. This temperature difference is not easily accessible in experiments. Nevertheless, one can assume, that the temperature gradient across the ferromagnet/ normal metal interface, which itself is directly proportional to the temperature increase of the Pt layer is directly proportional to ΔT_{me} [83].

[2] Figure from [84] with additional modifications by the author (of this thesis).

Following the arguments by *Xiao et al.* [106], ΔT_{me} will give rise to a spin current, perpendicular the the YIG/Pt interface. The spin current $\mathbf{j}_{\mathrm{s}}$ is converted into a charge current $\mathbf{j}_{\mathrm{c}}$ by the inverse spin Hall effect in Pt (*cf.* Sec. 2.3).
Owing to the open circuit geometry for $\mathbf{j}_{\mathrm{c}}$ used in the experiment, this can be measured as a voltage drop V_{ISH} along the Pt Hall bar. It is favorable to measure this voltage along a short "transverse" stripe of the Hall bar perpendicular to I_{d}. If the spin Seebeck voltage had been measured along the long side of the Hall bar, it would have been superimposed by a large offset voltage due to the driving current. Consequently, the spin Seebeck voltage will always be measured across two opposing contact pads in the following chapter, using a *Keithley 2182 Nanovoltmeter*.
As shown in Fig. 5.1, a magnetic field H_{ext} is applied in the sample plane. From Eq. (2.12) it follows, that the recorded voltage should be largest, if $\alpha = 0°$, since the voltage is measured perpendicular to the magnetic field H_{ext} and the temperature gradient ∇T, whereas no voltage should be recorded for $\alpha = 90°$. Two contact pads along the Hall bar were used to record V_{l}, which allows 4 terminal resistance measurements of the Pt film.

5.2.1 Pt thermometry

As discussed in Sec. 5.2, a current through the Pt is used in order to create a temperature gradient perpendicular to a YIG/Pt interface. One advantage of this technique is, that the Pt-layer can simultaneously be used for thermometry [15, 23, 33]. To calibrate the Pt thermometer first, the Pt resistance was measured as a function of the base temperature of the cryostat (*cf.* Fig. 5.2). In order to avoid heating effects, a *Linear Research LR700* AC resistance bridge, which measures the resistance employing very small driving currents, was used to perform this measurement. No magnetic field was applied during the measurement.
Two different samples were investigated: YIG(61)/Pt(11) and YIG(16.3)/Pt(2.8). For temperatures above $T = 50\,\mathrm{K}$, an almost linear dependence of the resistance as a function of the temperature is observed for both samples. The resistance decreases for lower temperatures, as expected for a metal. For temperatures below $T = 50\,\mathrm{K}$, the R vs. T curves flatten. This behavior is in agreement with the literature [61]. For the sample YIG(16.3)/Pt(2.8), a minimum in resistance can be observed at a temperatures of $T = 12\,\mathrm{K}$ (*cf.* Fig. 5.2(b)). For lower temperatures, the resistance

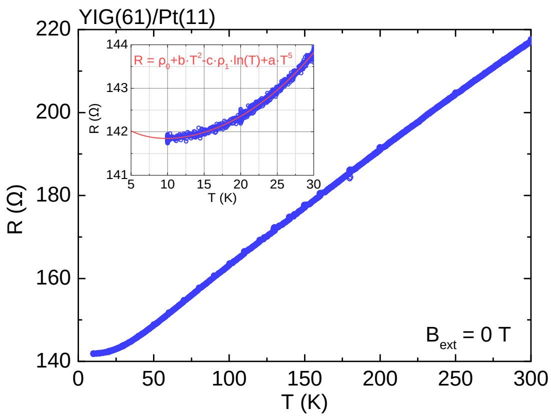

(a) Sample YIG(61)/Pt(11).

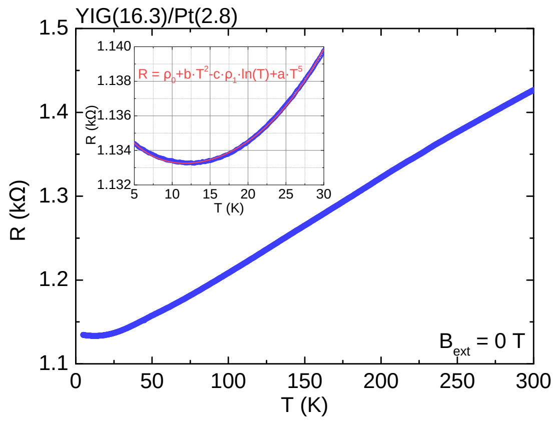

(b) Sample YIG(16.3)/Pt(2.8).

Figure 5.2: The4 terminal resistance of the Pt layer was measured as a function of the cryostat temperature with an AC resistance bridge to avoid heating effects. For high temperatures, the resistance shows almost linear dependence on the temperature and becomes smaller with decreasing temperature. For temperatures below $T = 30\,\mathrm{K}$, the decrease in resistance saturates. On the sample YIG(16.3)/Pt(2.8), a non monotonic behavior can be observed. For temperatures below $T = 12\,\mathrm{K}$, the resistance increases again [*cf.* inset in Fig. 5.2(b)].

is increasing with decreasing temperature. This behavior is not in agreement with the usual low temperature behavior of pure, bulk Pt [61]. One possible explanation for this behavior might be the *Kondo effect* [53]. The resistance as a function of the temperature is given by the following expression, if the Kondo effect is taken into account [52]:

$$\rho(T) = \rho_0 + bT^2 - c\rho_1 \log T + aT^5 \ .$$

ρ_0 is the residual resistance, $-c\rho_1 \log T$ the contribution from the Kondo effect, bT^2 is due to electron electron interaction [70] and the term aT^5 results from electron-phonon scattering at low temperatures. This expression was fitted to the measured data (red line in inset of Fig. 5.2). The agreement between theory and experiment is good. The Kondo effect is caused by localized magnetic moments in the Pt. Since the Stoner enhancement criterion [10] is fulfilled in platinum, the magnetic moments could be induced by the magnetic proximity effect [38]. However, XMCD measurements on similar YIG/Pt samples at room temperature did not show proximity polarized moments at the YIG/Pt interface [29]. On the other hand, Lu *et al.* report an enhancement of the proximity effect in YIG/Pt structures at low temperatures [58]. In order to clarify the role of interface effects, one could grow a thin platinum film on a non magnetic insulating substrate. If the effect is indeed caused by the magnetic proximity effect, it should not occur in platinum on non magnetic substrates.

5.3 Experimental results

5.3.1 Angular dependence of spin Seebeck effect

In this section, the magnetic field orientation dependence of the current driven spin Seebeck effect will be discussed. In the experiment, the orientation of the magnetic field is rotated in the sample plane as shown in Fig. 5.2. An angle α is enclosed between the magnetic field vector and the long stripe of the Hall bar. The strength of the magnetic field is $\mu_0 H = 1\,\mathrm{T}$. This field is large enough to align the magnetization of the sample always along the magnetic field vector. Thus, effects due to the remanent magnetization or magnetic anisotropy of the sample can be ruled out.

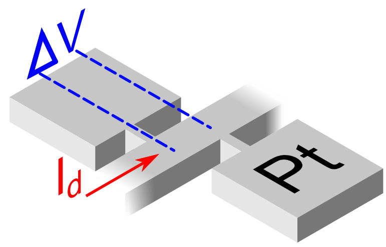

Figure 5.4: Due to a small misalignment of the feed lines of the Hall bar, a potential difference can be measured, while a current I_d flows through the Hall bar.

From the spin Hall effect, a $\cos(\alpha)$ dependence is expected for the spin Seebeck voltage (*cf.* Eq. (2.12)): $V_{\mathrm{iSSE}} \propto \cos(\alpha)$. In Fig. 5.3(a), the voltage drop along a short stripe is plotted for two different directions of the driving current I_d. It is obvious, that the measured voltage is not caused by the spin Seebeck effect alone. The angular dependence can be described as $V \propto \cos(\alpha)\sin(\alpha)$. This function was also fitted to the data and describes the measurement well. In addition, a voltage offset is observed and the sign of the voltage is changed by an inversion off the current direction. Since the spin Seebeck effect only depends on the temperature gradient caused by the current, it should not be affected by the current direction. However the measured angular dependence as well as the inversion of the voltage sign can be explained by magneto-resistive effects. The offset voltage is caused by

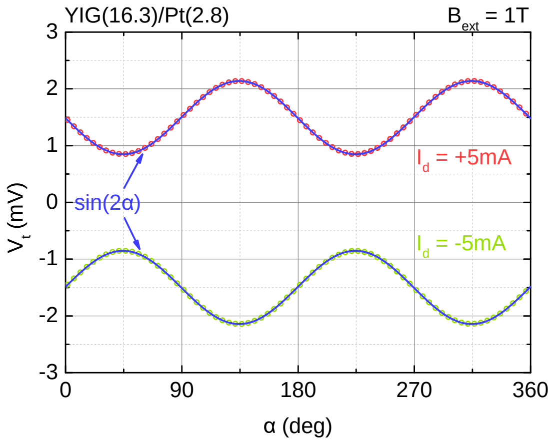

(a) voltage drop at short stripe on the sample YIG(16.3)/Pt(2.8)

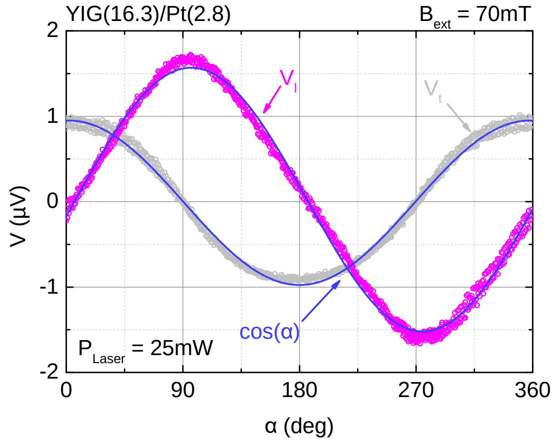

(b) spin Seebeck effect voltage due to laser heating on the sample YIG(16.3)/Pt(2.8)

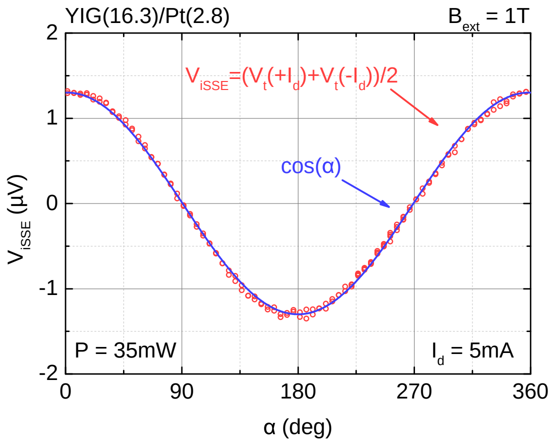

(c) spin Seebeck effect voltage due to current heating on the sample YIG(16.3)/Pt(2.8)

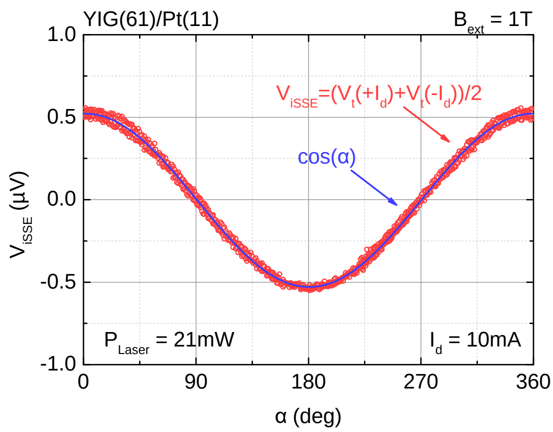

(d) spin Seebeck effect voltage due to current heating on the sample YIG(61)/Pt(11)

Figure 5.3: The spin Seebeck voltage as a function of the magnetic field orientation for a field strength of $B = 1\,\mathrm{T}$ (panel (c) and (d)). The angle α between the long stripe of the Hall bar and the magnetic field was varied while the voltage drop across the short stripes was recorded (*cf.* Fig. 5.2). A corresponding $\cos(\alpha)\sin(\alpha)$ (panel (a)) or $\cos(\alpha)$ (panel (b), (c) and (d)) dependence was fitted to the data. In addition angular dependent measurements, performed with laser heating, are plotted (panel (b)).

a small misalignment of the feed lines of the Hall bar, as shown in Fig. 5.4. Due to the finite resistance between the feed lines a potential difference will build up. The $\cos(\alpha)\sin(\alpha)$ angular dependence of the measured voltage can be explained by the recently reported spin Hall magneto resistance (SMR) effect [6, 11, 68]. This resistive effect is caused by reflection and absorption of spin currents at the YIG/Pt interface. This spin currents arise due to the spin Hall effect in the platinum. For the SMR, it is expected that the voltage changes sign by inversion of the current direction, since it is a a resistive effect.

In Fig. 5.3(b), the spin Seebeck voltage is plotted as a function of the magnetic field direction. For this measurement, a laser[3] was used to establish the temperature gradient. Thus, no magneto-resistive effects occur and the voltage is proportional to $\cos(\alpha)$. This is confirmed by corresponding fits, which show good agreement with the measured data.

The phase shift of $\pi/2$ between both measurements is cause by different measurement directions of the voltage (V_l along the long stripe of the Hall bar and V_t along a short stripe). The different magnitudes between V_l and V_t is caused by the different effective width of the Hall bar for the different measurement directions. Since the width of the Hall bar in longitudinal direction is smaller, a bigger voltage is expected. Therefore, the ration between V_l and V_t is qualitatively correct. A quantitative analysis is not possible, since the voltage depends strongly on the laser spot position on the sample surface [82].

Finally, it will be shown, that it is also possible to extract the spin Seebeck voltage from the measurement of V_t in Fig. 5.3(a). To this end, one can employ the fact, that the measured voltage is a superposition of a voltage due to the resistance of the Hall bar V_res and the spin Seebeck voltage V_iSSE:

$$V_\mathrm{t} = V_\mathrm{iSSE} + V_\mathrm{res}$$

The temperature gradient does not depend on the direction of the current I_d and consequently the spin Seebeck voltage V_iSSE does not depend on the current direction, while V_res is proportional to the current. After adding the voltages V_t, measured for both directions of the current I_d, the resistive voltage contributions

[3] The laser was not modulated, the voltage was detected DC with a Keithley K2182A Nanovoltmeter.

will cancel out[4]:

$$V_t(+I_d) + V_t(-I_d) = (V_{iSSE}(+I_d) + V_{res}(+I_d)) + (V_{iSSE}(-I_d) + V_{res}(-I_d)) \quad (5.1)$$

$$= V_{iSSE}(+I_d) + V_{res}(+I_d) + V_{iSSE}(+I_d) - V_{res}(+I_d) \quad (5.2)$$

$$= 2V_{iSSE}(+I_d) \quad (5.3)$$

The result of this procedure is shown in Fig. 5.3(c) for the raw voltage signals plotted in Fig. 5.3(a). The resulting voltage due to the spin Seebeck effect is 3 orders of magnitude smaller then the originally detected voltage V_t. It clearly shows a $\cos(\alpha)$ dependence as expected for the spin Seebeck effect/ inverse spin Hall effect. Further it agrees quantitatively with the results obtained by the laser induced spin Seebeck effect [Fig. 5.3(b)]. After normalizing the spin Seebeck voltage to the heating power, one obtains for both measurements $V_{iSSE}/P = 0.04\,\mu\mathrm{V\,mW^{-1}}$. As a control experiment, the same measurement was performed on a second sample (*cf.* Fig. 5.3(d)). Again a $\cos(\alpha)$ angular dependence of the V_{SSE} voltage, derived with Eq. (5.1), is observed.
In conclusion, the obtained angular dependence of the spin Seebeck effect on the magnetic field, measured in the current induced spin Seebeck effect setup, does agree quantitatively with results from laser induced spin Seebeck effect measurements. However, in order to avoid magneto-resistive effects, it is important to use the symmetry of the spin Seebeck effect: The spin Seebeck effect is even with respect to the direction of the heating current.

5.3.2 Magnetic field dependence of the spin Seebeck voltage

The measurements in the previous section have all been done at high fields, in magnetic saturation. However, it is also interesting to study the SSE in the low field limit. Figure 5.5(a) shows the spin Seebeck voltage as a function of the magnetic field amplitude, while the temperature gradient was induced via laser heating. The measurement was performed at an angle of $\alpha = 0°$ between the long side of the Hall bar and the external magnetic field. From Eq. (2.12) it can be concluded, that the spin Seebeck voltage follows the spin polarization vector σ and thus the external field direction. For this reason a hysteresis loop is observed. The coercive fields

[4] This procedure is known as "Doblersches addieren".

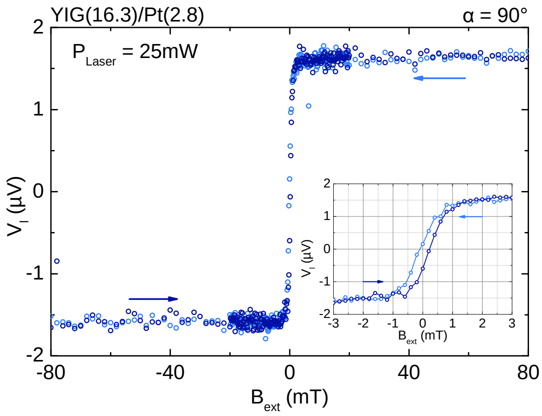

(a) spin Seebeck voltage as a function of the magnetic field magnitude due to laser heating.

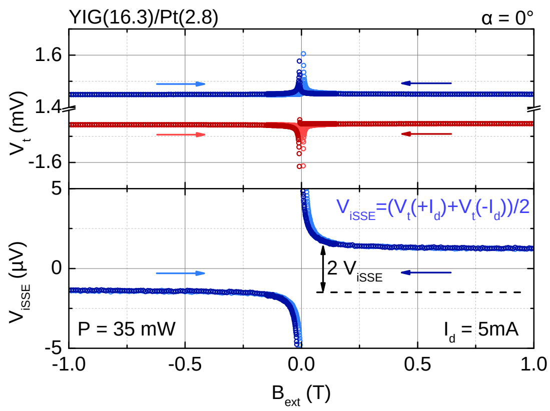

(b) spin Seebeck voltage as a function of the magnetic field magnitude due to current heating for $\alpha = 0°$.

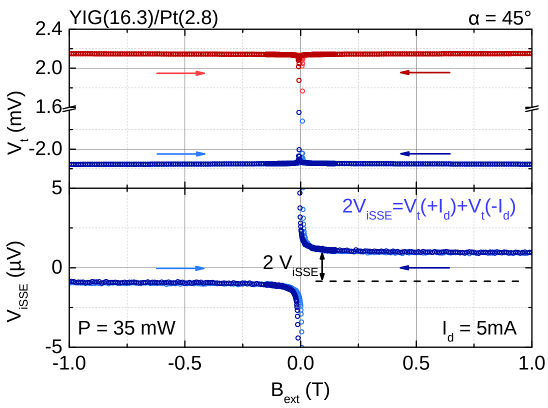

(c) spin Seebeck voltage as a function of the magnetic field magnitude due to current heating for $\alpha = 45°$.

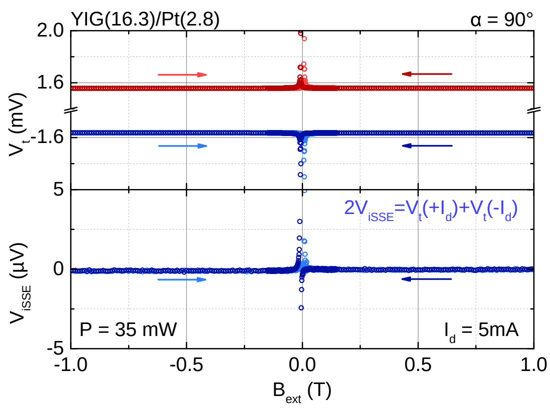

(d) spin Seebeck voltage as a function of the magnetic field magnitude due to current heating for $\alpha = 90°$.

Figure 5.5: Spin Seebeck voltage hysteresis loops on the sample YIG(16.3)/Pt(2.8). The V vs. B curves were measured for different orientations of the magnetic field in the sample plane. The magnitude of the driving current was kept constant at $I_\mathrm{d} = 5\,\mathrm{mA}$. The upper part of panels (a), (b) and (c) show the raw voltage signals, while the lower ones give the respective spin Seebeck voltages, obtained by adding the measurements at $+I_\mathrm{d}$ and $-I_\mathrm{d}$.

[inset of Fig. 5.5(a)] are rather small ($B_\mathrm{c} \approx 0.2\,\mathrm{mT}$). The sample is in the state of saturated magnetization at fields of $B_\mathrm{sat} \approx 1\,\mathrm{mT}$.
Figure 5.5(b) shows the equivalent experiment in the current heating scheme. In the upper panel of the figure, the voltage drop across the short stripe of the Hall bar is shown for both current directions. Similarly to the measurements presented

in the previous section, these raw voltage signals are dominated by resistive and geometric effects. However close to the coercive field, peaks in the voltage are observed. These peaks are hysteretic, since the peaks for up- and down sweep do not overlap and can be explained by the SMR effect [6].
The spin Seebeck voltage is obtained by adding the voltages measured for both current directions (lower panel of Fig. 5.5(b)). For magnetic fields $|B| > 200\,\mathrm{mT}$, the voltage does depend only on the direction of the magnetic field but not on the magnitude. This behavior was expected, since the sample is in full saturation at such high fields. This behavior is identical to the laser induced spin Seebeck effect, albeit saturation of the measured voltage in the latter is observed for much smaller fields already. The features observed in small fields are cause by Oersted fields, induced by the heating current and will be discussed in Sec. 5.3.6.
To verify, that the observed voltage signal in Fig. 5.5(b) can be attributed to the spin Seebeck effect, the measurement was repeated for different orientations of the magnetic field with respect to the long side of the Hall bar. For $\alpha = 45°$, the difference between the voltage for large positive and large negative magnetic fields becomes smaller. This is in good agreement with the measurements shown in Fig. 5.3. If an angle of $\alpha = 90°$ degrees is chosen, the spin Seebeck effect vanishes completely, as expected, since magnetic and electric fields are in parallel in this configuration. Only for small fields close to the coercive fields, peaks can be seen, due to induced Oersted fields.

5.3.3 Power dependence of the spin Seebeck effect

In this section the heating power dependence of the spin Seebeck voltage will be discussed. The temperature gradient is approximately linear with respect to the dissipated power in the platinum film [83]. Since the spin Seebeck voltage scales linearly with the temperature gradient [106], a linear dependence between the power and the spin Seebeck voltage is expected.
Figure 5.6(a) shows the dependence of the spin Seebeck voltage on the deposited power with the laser heating technique[5]. The voltage is measured along the long stripe (V_{long}) and along a short stripe (V_{trans}) of the Hall bar. For each value of the power, the angle α between the long side of the Hall bar and the magnetic field,

[5]Again, the laser was not modulated and the voltage was recorded with standard DC technique.

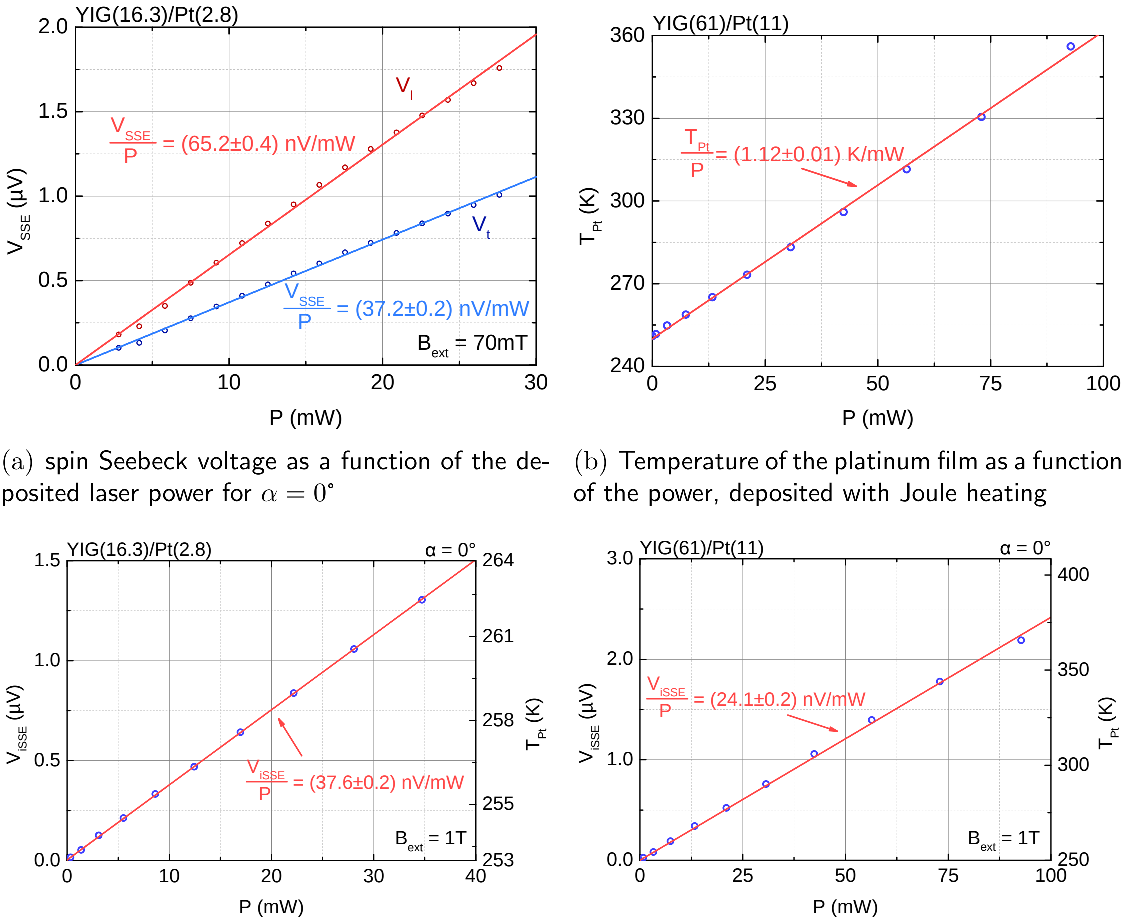

(a) spin Seebeck voltage as a function of the deposited laser power for $\alpha = 0°$

(b) Temperature of the platinum film as a function of the power, deposited with Joule heating

(c) spin Seebeck voltage and Pt temperature as a function of the power, deposited with Joule heating for $\alpha = 0°$

(d) spin Seebeck voltage and Pt temperature as a function of the power, deposited with Joule heating for $\alpha = 0°$

Figure 5.6: This figure shows, that the spin Seebeck voltage scales linearly with the heating power. For each value of the power, a measurement of $V_{\mathrm{iSSE}}(\alpha)$ was performed. By fitting, the corresponding spin Seebeck voltage was determined. In addition to the spin Seebeck voltage, the corresponding platinum temperature is plotted.

was swept from $\alpha = 0°$ to $\alpha = 360°$. By fitting a $\cos(\alpha)$ function to the data, as described in Sec. 5.3.1, the amplitude of the voltage signal was determined. Clearly, the spin Seebeck voltage is proportional to the heating power. This confirms the statement from the beginning of this section, that the temperature gradient is proportional to the deposited power.

As discussed in Sec. 5.2.1, the current induced spin Seebeck effect allows to determine the platinum temperature while the spin Seebeck effect is measured. In Fig.

5.6(b), the temperature of the platinum T_{Pt} is plotted as a function of the heating power. The platinum temperature is obtained by measuring the longitudinal platinum resistance. With the aid of the results, obtained in Sec. 5.2.1, the corresponding temperature is found. From this measurement it is possible to conclude, that the platinum temperature scales linear with the heating power, as expected.
Finally, Fig. 5.6(c) and Fig. 5.6(d) show the spin Seebeck voltage due to current heating, as a function of the heating power. It was possible to calculate the power, since the resistance was measured for each applied current:

$$P = R(T) \cdot I_{\mathrm{d}}^2 \, . \tag{5.4}$$

Again, for each value of the power, the magnetic field orientation was swept by 360° for both current directions. Adding up the results (*cf.* Eq. 5.1), a $\cos(\alpha)$ dependence was observed. The amplitude was then determined by fitting and plotted against the power (*cf.* Sec. 5.3.1).
Figure 5.6(c) and Fig. 5.6(d) confirm, that the spin Seebeck voltage is proportional to the heating power. Since the platinum temperature T_{Pt} as well as the spin Seebeck voltage V_{iSSE} are linear to the heating power, the spin Seebeck voltage V_{iSSE} must depend linearly on changes of to the platinum temperature T_{Pt} from it's usual (no heating) equilibrium value. By fitting the temperature increase with respect to the heating power, T_{Pt} can be plotted simultaneously with the measured voltage on the right axis of the Fig. 5.6(c) and 5.6(d).
Note that the power dependence of the spin Seebeck voltage measured with laser heating and current heating agrees within the error interval for the sample YIG(16.3)/Pt(2.8) [*cf.* V_t in Fig. 5.6(a) and Fig. 5.6(c)]. Further, the measurements, performed in this section agree quantitatively with the measurements shown in Sec. 5.3.1 and Sec. 5.3.2.

5.3.4 Temperature dependence of the spin Seebeck effect

In literature, the dependence of the spin Seebeck effect on the average temperature did already attract some attention [1, 62, 72, 74, 100]. *Adachi et al.* suggested an maximum of the spin Seebeck effect for low temperatures due to a mechanism, called phonon drag [1]. *Uchida et al.* indeed published temperature dependent

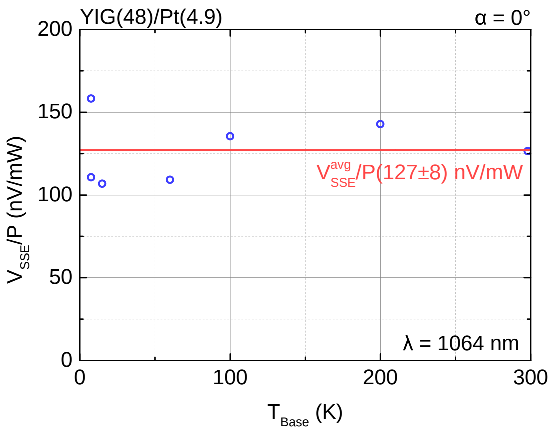

(a) Spin Seebeck voltage normalized to the laser power for different base temperatures of the cryostat on the sample YIG(48)/Pt(4.9).

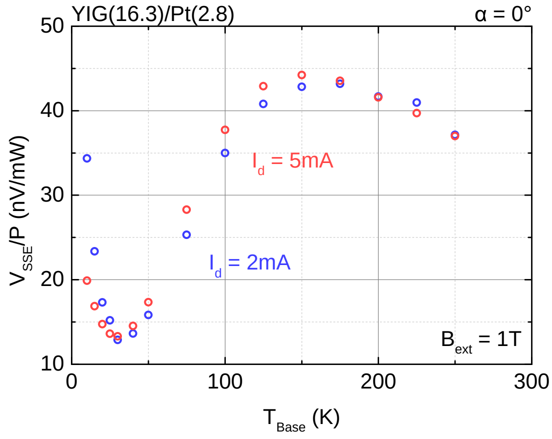

(b) Current driven spin Seebeck effect normalized to the deposited power as a function of the cryostat base temperature on the sample YIG(16.3)/Pt(2.8).

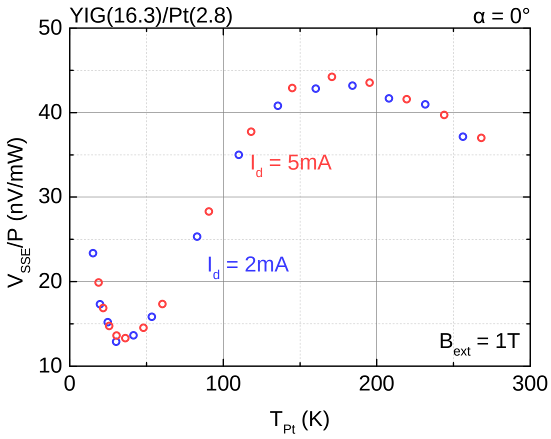

(c) Current driven spin Seebeck effect normalized to the deposited power as a function of the platinum temperature on the sample YIG(16.3)/Pt(2.8).

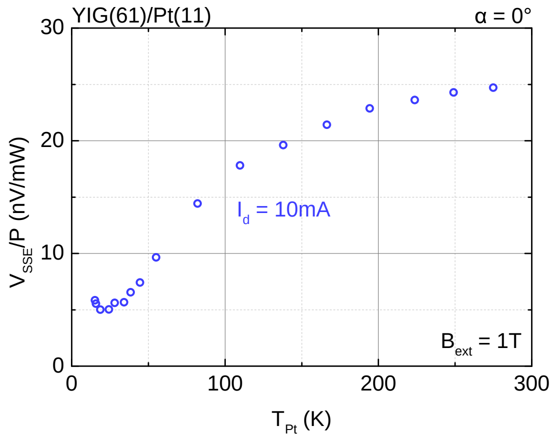

(d) Current driven spin Seebeck effect normalized to the deposited power as a function of the platinum temperature on the sample YIG(61)/Pt(11).

Figure 5.7: Temperature dependent measurements of the spin Seebeck effect, using laser heating (a) and current heating (b), (c), (d) in order to establish a temperature gradient. The wavelength of the laser was chosen below the bandgap of YIG. While the spin Seebeck voltage measured with laser heating stayed almost constant, a decrease in signal was observed in the experiments using current heating.

spin Seebeck effect measurements on single crystalline YIG, which showed a large enhancement of the spin Seebeck effect at a temperature of around 50 K [100]. For even lower temperatures, the spin Seebeck voltage vanished.

Measurements, performed by *Meier et al.* on $NiFe_2O_4$/Pt films, however did not show an enhancement of the spin Seebeck effect at low temperatures but a monotonic decrease in the spin Seebeck voltage [62]. These measurements are in agreement with the theory by *Rezende et al.* [74].
In collaboration with Yori Manzke from the *Paul Drude Institute, Berlin* a set of SSE measurements using the laser heating technique in a ^{4}He liquid flow cryostat could be performed. The obtained results will be compared to temperature dependent spin Seebeck effect measurements, using the current induced spin Seebeck setup in this section.
A laser with a wavelength of $\lambda_{\mathrm{Laser}} = 1064\,\mathrm{nm} = 1.17\,\mathrm{eV}$ was chosen for the temperature dependent measurements, which is below the band gap of YIG of about 2.8 eV [64, 105].
In order to obtain the spin Seebeck voltage as a function of the cryostat temperature, full V_{SSE} vs. H loops were recorded, as shown in Fig. 5.5(c), for 4 different laser powers. The amplitudes of the hysteresis loops was determined by a fit from which, by averaging the results, the spin Seebeck voltage normalized to the laser power is obtained. This procedure is repeated for different cryostat temperatures. The result is shown in Fig. 5.7(a).
This measurement suggest, that the spin Seebeck effect is constant as a function of the temperature plotted as the red line in Fig. 5.7(a). Some noise can be seen for the data points below $T = 100\,\mathrm{K}$ (especially the point at the lowest temperature was measured twice). This can be explained by a shift of the laser focus. The result of a constant spin Seebeck voltage is surprising, since the spin Seebeck effect depends on many parameters, which are temperature dependent themselves. For example, *Meyer et al.* reported, that the spin Hall angle decreases by $\approx 35\,\%$ from $T = 200\,\mathrm{K}$ to $T = 10\,\mathrm{K}$ [65].
Next, the temperature dependence of the current induced spin Seebeck effect will be discussed. At each measurement point, a full angular sweep of the external magnetic field orientation was recorded, as discussed in Sec. 5.3.1 with $|\mu_0 H| = 1\,\mathrm{T}$. The amplitude was determines by fitting a $\cos(\alpha)$ function to the data. Afterwards the result was normalized to the heating power. The temperature was controlled in a ^{4}He cryostat.
Figure 5.7(b) shows the spin Seebeck voltage as a function of the cryostat base temperature T_{Base} for two different heating currents on the sample YIG(16.3)/Pt(2.8).

The points for both heating currents do not overlap, even though the spin Seebeck voltage is normalized to the heating power. The reason is, that the measured temperature is not identical with the temperature at the sample (the temperature sensor is mounted a few cm away from the sample). Therefore, it is better to plot the spin Seebeck voltage as a function of the Pt temperature. This temperature is measured directly on chip, so the difference to the actual temperature should be smaller.

Consequently, in figure 5.7(c), the normalized spin Seebeck voltage is plotted as a function of the platinum temperature T_{Pt} for the same sample. Now, the normalized results of the measurements with $I_{\mathrm{d}} = 2\,\mathrm{mA}$ and $I_{\mathrm{d}} = 5\,\mathrm{mA}$ do agree. The observed temperature dependence is non monotonic. A maximum $V_{\mathrm{SSE}}^{175\mathrm{K}} = 1.2 V_{\mathrm{SSE}}^{250\mathrm{K}}$ is reached at $T_{\mathrm{Pt}} \approx 175\,\mathrm{K}$ and a minimum $V_{\mathrm{SSE}}^{30\mathrm{K}} = 0.1 V_{\mathrm{SSE}}^{250\mathrm{K}}$ is reached for $T_{\mathrm{Pt}} \approx 30\,\mathrm{K}$. For low temperatures, the spin Seebeck amplitude increases again. On the sample YIG(61)/Pt(11), a similar dependence can be observed. However, the minimum at low temperatures is not as pronounced and no maximum is observed in the measured temperature range.

These results are qualitatively different from the temperature dependence measured with laser heating (Fig. 5.7(a)). However, due to the noise in the laser measurement, a minimum at low temperatures can not be excluded. Further, the obtained temperature dependencies are also different from the results reported so far in literature. Especially the increase in signal for very low temperatures is remarkable. It has to be admitted, that the resistance of the platinum layer also has a minimum at low temperatures and is increasing for very small temperatures (compare to Sec. 5.2.1). However the minima of both measurements do not occur at the same position. Even though both investigated YIG/Pt samples show qualitatively the same behavior, they are quantitatively different. The reason could be, that the temperature dependence is influenced by the thickness of the platinum layer. Interface effects e.g. would be more pronounced in thinner samples.

The temperature dependent measurements, performed in this section, do provide some insights into the theory of the spin Seebeck effect. First of all, no phonon drag peak was observed, as reported in Refs. [1, 100]. However the results do qualitatively agree with the theory of Rezende *et al.* [74] for temperatures above 50 K, especially on the sample YIG(61)/Pt(11).

Phenomenologically the increase at low temperatures could be explained with an additional contribution from the anomalous Nernst effect due to proximity induced magnetic moments in the Pt. While no evidence of a proximity polarization in Pt was observed on very similar samples at room temperature [29], an enhancement of the proximity effect at low temperatures is reported [56, 58]. Additionally the termination of the YIG interface might play a role on whether or not a magnetization can be induced.

5.3.5 Lock in detection of the spin Seebeck effect voltage

All voltage measurements of the current induced spin Seebeck effect so far were performed with a *Keithley K2182 nanovoltmeter* using standard DC detection. However, AC current modulation and lock-in detection offers many advantages. First of all, noise can be suppressed by lock-in detection, allowing lower heating currents. Secondly, it is not necessary, to measure the voltage drop for two different current directions separately and add both voltages afterwards (*cf.* Eq. (5.1)). Since also current modulation frequencies in the kHz range are possible, the measurement time can be reduced significantly.
In order to explain the AC measurements, it is important to discuss how the deposited power hinges in the heating current, because the temperature gradient and consequently the spin Seebeck voltage is proportional to the heating power. This will be done in the following paragraph: The heating power can be written as (*cf.* Eq. (5.4)):

$$P = R(T) \cdot I_{\mathrm{d}}^2 \, . \tag{5.5}$$

The resistance itself is a function of the temperature (compare to Sec. 5.2.1). Since the temperature is proportional to the power and the power does depend on the heating current, the resistance is a function of the heating current in the end. Figure 5.8(a) shows, that the resistance changes approximately linearly with the heating current squared, $R_{\mathrm{long}} = R_0 + r \cdot I_{\mathrm{d}}^2$ for the range of I_{d} of interest here. Putting this into Eq. 5.5 gives:

$$\begin{aligned} P =& (R_0 + r \cdot I_{\mathrm{d}}^2) \cdot I_{\mathrm{d}}^2 \\ =& R_0 \cdot I_{\mathrm{d}}^2 + r \cdot I_{\mathrm{d}}^4 \ . \end{aligned}$$

Thus, there is one contribution to the heating power, which scales as I_{d}^2 and one contribution, which scales as I_{d}^4. In order to estimate the contribution of this two terms to the heating power P, a fit was made to the data in Fig. 5.8(a). The values for r and R_0 can be found in the figure. With a maximum current of $I_{\mathrm{d}} = 25\,\mathrm{mA}$ the following values for the heating power are calculated for the YIG(61)/Pt(11) sample:

$$P = \underbrace{204\,\Omega \cdot I_{\mathrm{d}}^2}_{=130\,\mathrm{mW}} + \underbrace{0.066\,\Omega\,\mathrm{mA}^{-2} \cdot I_{\mathrm{d}}^4}_{2.6\,\mu\mathrm{W}} \ .$$

Since the $\propto I^2$ term dominates the $\propto I^4$ term, the deposited power is not affected by the increase of the resistance caused by the heating, as confirmed by the fits in Fig. 5.8.

For AC detection, the driving current I_{d} is modulated with a sine wave function, using a *HP 3245A Universal Source*:

$$I_{\mathrm{d}} = I_0 \cdot \sin(2\pi f_{\mathrm{mod}} t) \ .$$

Putting this expression into Eq. (5.5) (R is assumed to be constant) gives:

$$\begin{aligned} P =& R \cdot I_0^2 \cdot \sin^2(2\pi f_{\mathrm{mod}} t) && (5.6) \\ =& R \cdot I_0^2 \cdot 0.5\,(1 - \cos(2(2\pi f_{\mathrm{mod}} t))) \ . && (5.7) \end{aligned}$$

Thus, there is one term emerging, which is constant in time and one term, which is proportional to $\cos(2\omega t)$. The second term is measured with a *Stanford research SR 830* lock-in amplifier using second harmonics voltage detection. Voltage signals, measured with second harmonics detection contain only contributions, proportional to even powers of the driving current I_{d}. Resistive effects, which are directly proportional to I_{d}, do not contribute to the second harmonics voltage.

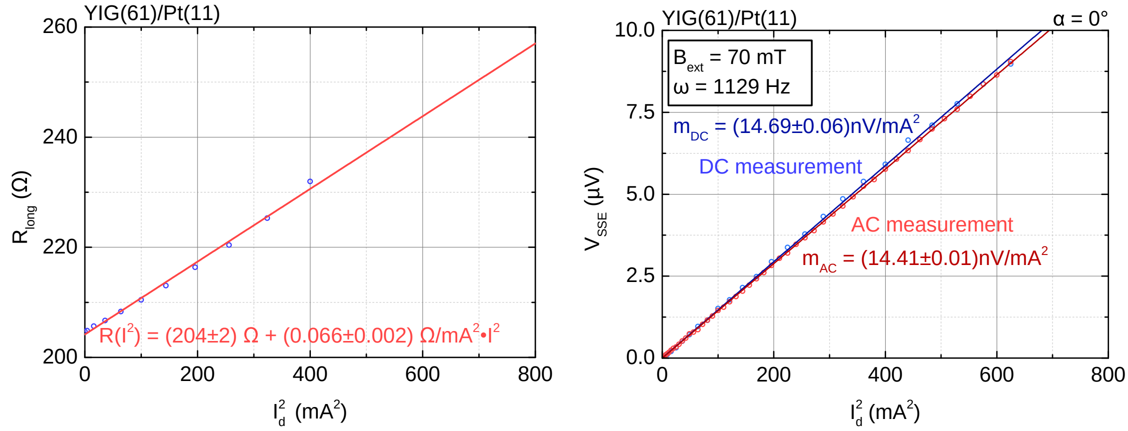

(a) Change in resistance as a function of the applied current I_d^2.

(b) Spin Seebeck voltage as a function of the applied current I_d^2.

Figure 5.8: Spin Seebeck voltage as a function of the heating current I_d^2, measured with the standard dc detection method and with lock-in detection. The modulation frequency of the current was $2\pi f = 1129\,\mathrm{Hz}$. With both measurement methods, a linear dependence between V_SSE and I_d^2 is obtained. The slope of both lines agrees well.

Figure 5.8(b) shows the AC detected spin Seebeck voltage as a function of the driving current I_d^2. As expected, the spin Seebeck voltage is proportional to the power. For comparison, the spin Seebeck voltage, measured with standard DC detection is plotted in Fig. 5.8(b) as well. The slope for both measurement techniques are essentially identical. However, it has to be mentioned that the lock-in amplifier will not measure the same voltage as compared to the voltage obtained with DC measurements, a priori. Instead, the second harmonic voltage, measured with a lock-in amplifier, has to be multiplied by a factor of $2\sqrt{2}$. The reason is, that the lock-in amplifier does not detect the amplitude of the voltage but the root mean square voltage [91], introducing a factor of $\sqrt{2}$. Another factor of 2 is contained in Eq. (5.7), due to the detection of the second harmonic voltage.

In conclusion, it is possible to reproduce the DC measurement results, using an AC current source and a lock-in. The major advantage of the lock-in measurement is that it can be conducted much faster. Measuring the voltage drop with the DC technique for two different current directions takes $\approx 5\,\mathrm{s}$, due to the time needed for the voltage to stabilize after the current direction is switched. For AC measurements performed at $f_\mathrm{mod} = 1\,\mathrm{kHz}$, a measurement time of $\approx 5\,\mathrm{ms}$ will be needed, provided 5 periods are enough for the signal to stabilize. Consequently, AC detection is more than 1000 times faster.

Further, noise is reduced by AC detection techniques [91]. Comparing the linear fits in Fig. 5.8(b) shows, that the error in the AC detection technique is a factor of 6 smaller. It has to be mentioned, that measurement time and noise suppression are not independent from each other. For longer measurement times, an even lower noise level can be archived.

5.3.6 Spin Seebeck effect in small magnetic fields

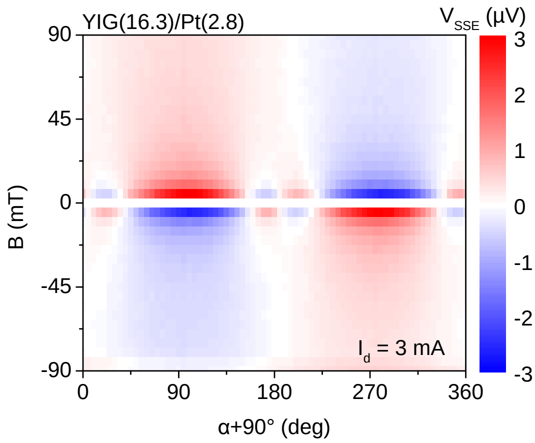

(a) False color plot of the spin Seebeck voltage as a function of the magnetic field orientation and the magnetic field magnitude.

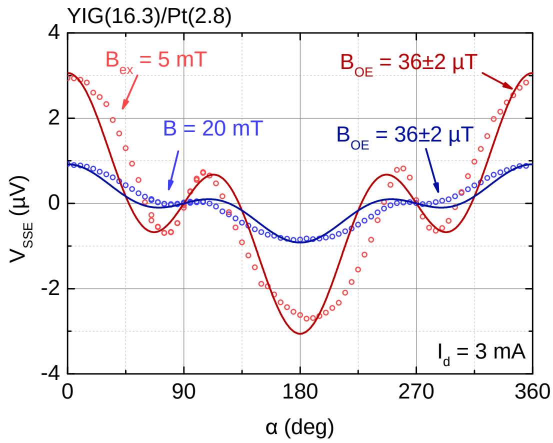

(b) Spin Seebeck voltage as a function of the magnetic field orientation for $B = 5\,\mathrm{mT}$ and $B = 20\,\mathrm{mT}$.

Figure 5.9: Spin Seebeck effect as a function of the field orientation for field magnitudes $\mu_0 H \leq 90\,\mathrm{mT}$ and a DC driving current of $I_d = 3\,\mathrm{mA}$. The solid lines represent theoretical curves with the spin Seebeck effect and the spin Hall magneto-resistance taken into account. The contribution from the spin Hall magneto-resistance in the even (with respect to current) voltage is caused by an Oersted field due to the current in the platinum layer.

Rotations of the magnetic field orientation in the sample film plane have already been discussed in Sec. 5.3.1. It was found, that the spin Seebeck voltage is proportional to $\cos(\alpha)$, where α is defined in Fig. 5.1. In Sec. 5.3.2, however, an unusual behavior of the spin Seebeck voltage in small external magnetic fields was observed. These features will be investigated in this section.

It is important the mention, that the field magnitude, applied for in plane rotation ($5\,\mathrm{mT} \leq |\mu_0 H| \leq 90\,\mathrm{mT}$) is always well above the coercive field of the YIG film (*cf.* Fig. 5.5(c)). The magnetization is already in full saturation at $\mu_0 H_{\text{ext}} = 1\,\text{mT}$. Figure 5.9(a) shows a false color plot of the spin Seebeck voltage as a function of the magnetic field orientation and the magnetic field magnitude. Again, the spin Seebeck voltage was obtained by measuring the voltage drop at the short stripe of the Hall bar for both current directions which were added up afterwards (*cf.* Eq. 5.1). For the field of $\mu_0 H_{\text{ext}} = 90\,\text{mT}$ (*cf.* Fig. 5.9(a)), the angular dependence of the spin Seebeck voltage is well described by a simple $\cos(\alpha)$. A maximum and a minimum occur, as well as two zero-crossings. For smaller fields, the magnitude of the spin Seebeck voltage at the maximum ($\alpha = 0°$) is enhanced. Further the zero-crossings become broader. At fields $B \leq 10\,\text{mT}$, additional peaks become apparent.

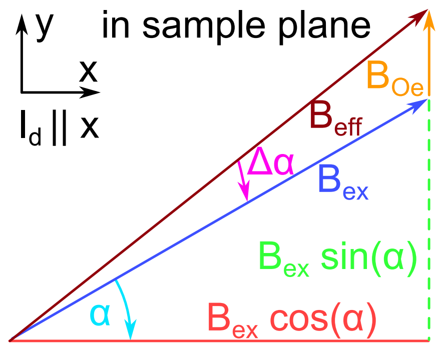

Figure 5.10: Visualization of the contribution of the Oersted field to the effective magnetic field.

In Fig. 5.9(b), the spin Seebeck voltage is plotted as a function of the magnetic field orientation for two different values of B. In this figure, it becomes obvious, that the spin Seebeck signal is superimposed by higher order terms. This behavior can be explained by Oersted fields, generated by the current in the platinum layer [35, 54]. Each static current density $\mathbf{j}_\text{d}$ generates a static magnetic Oersted field B_{Oe} (Amperes law):

$$\nabla \times \mathbf{B}_{\text{Oe}} = \mu_0\,\mathbf{j}_\text{d}. \tag{5.8}$$

The Oersted field does depend on the current density but not on the external magnetic field. The effective field B_{eff} the magnetic moments in the YIG are exposed to is a superposition of the Oersted field and the externally applied magnetic field B_{ex}:

$$B_{\text{eff}} = B_{\text{ex}} + B_{\text{Oe}}. \tag{5.9}$$

This relation is depicted in Fig. 5.10. The Oersted field B_{Oe}, does chance the angle α between the current and the effective magnetic field by an angle $\Delta\alpha$. It is

important, that the angle $\Delta\alpha$ depends on the current direction. Consequently, the total angle α_{eff} between the effective magnetic field B_{eff} and the current direction does depend on the current direction as well. This introduces contributions in the "spin Seebeck voltage" from the spin Hall magneto-resistance as will be shown in the following.
The voltage drop due to the spin Hall magneto-resistance is given as [11]:

$$V_{\mathrm{SMR}} = R_0 \cdot I_{\mathrm{d}} \cdot \cos(\alpha_{\mathrm{eff}}) \sin(\alpha_{\mathrm{eff}}) \; . \tag{5.10}$$

In Eq. (5.1) it was assumed that all contributions from the spin Hall magneto-resistance cancel out if the measured voltages for different current directions were added up. If α_{eff} is notably different from α, this is, however, not the case anymore:

$$\begin{aligned} \Delta V_{\mathrm{SMR}} &= V_{\mathrm{SMR}}(+I_{\mathrm{d}}) + V_{\mathrm{SMR}}(-I_{\mathrm{d}}) && (5.11)\\ &= R_0 I_{\mathrm{d}}[\cos(\alpha_{\mathrm{eff}}(+I_{\mathrm{d}})) \sin(\alpha_{\mathrm{eff}}(+I_{\mathrm{d}})) - \cos(\alpha_{\mathrm{eff}}(-I_{\mathrm{d}})) \sin(\alpha_{\mathrm{eff}}(-I_{\mathrm{d}}))] && (5.12) \end{aligned}$$

Since the angle α_{eff} is a function of the current, the trigonometric functions do not cancel out, as it was the case, when the Oersted fields were not considered. To evaluate the term for ΔV_{SMR}, expressions for α_{eff} have to be found. By using simple trigonometry (*cf.* Fig. 5.10), one obtains the following result:

$$\alpha_{\mathrm{eff}}(\pm I) = \arctan\left(\frac{B_{\mathrm{ex}} \sin(\alpha) \pm B_{\mathrm{Oe}}}{B_{\mathrm{ex}} \cos(\alpha)}\right) \; .$$

With this result and using the identities $\cos(\arctan(x)) = 1/\sqrt{1+x^2}$ and $\sin(\arctan(x)) = x/\sqrt{1+x^2}$, Eq. (5.12) transforms to:

$$\Delta V_{\mathrm{SMR}}(\alpha) = R_0 I_{\mathrm{d}} \left(\frac{2a\cos(\alpha)(a^2 + \cos(2\alpha))}{1 + a^4 + 2a^2\cos(2\alpha)}\right) \; .$$

Here, $a = B_{\mathrm{Oe}}/B_{\mathrm{ex}}$ is the ratio between the Oersted field magnitude and the external field magnitude. The total measured voltage (Fig. 5.9(b)) is then the sum of both the SMR contributions and the spin Seebeck voltage:

$$V_{\mathrm{tot}}(\alpha) = V^0_{\mathrm{SMR}} \left(\frac{2a\cos(\alpha)(a^2 + \cos(2\alpha))}{1 + a^4 + 2a^2\cos(2\alpha)}\right) + V^0_{\mathrm{SSE}} \cos(\alpha) \; .$$

This model was fitted to the data in Fig. 5.9(b). The only free fit parameter was the Oersted field B_{Oe}, since V_{SMR}^{0} and V_{SSE}^{0} are known from the measurements in Fig. 5.3. For the measurement with $B_{\mathrm{ex}} = 5\,\mathrm{mT}$ and $B_{\mathrm{ex}} = 20\,\mathrm{mT}$, the same Oersted field is derived with the fit. This is plausible, since the same driving current was used in both measurements. It has to be noted, that there is a small mismatch between the theoretical curve and the experimental data in Fig. 5.3. It is possible, that this mismatch is cause by spin torque effects [25, 26]. So far, these effects were not observed in ferrimagnetic insulator/ normal metal samples.

5.3.7 Spin Seebeck effect in large magnetic fields

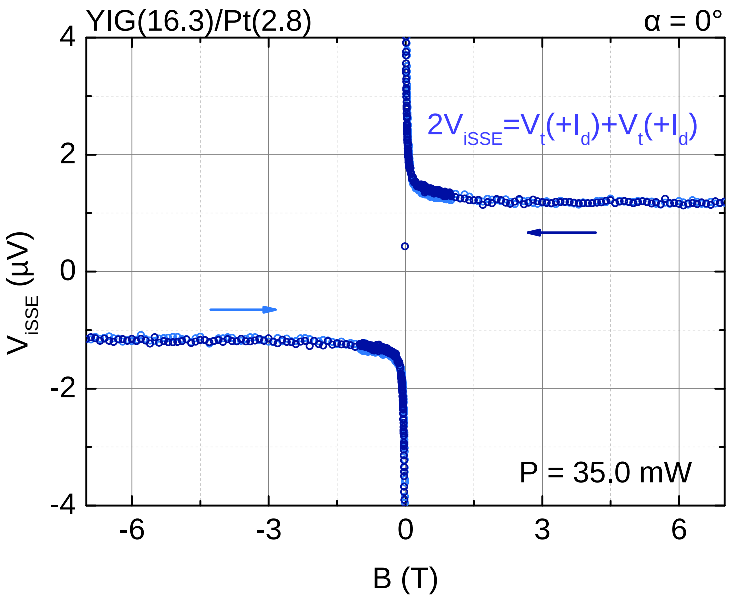

Figure 5.11: Spin Seebeck effect measurement in large magnetic fields on the sample YIG(16.3)/Pt(2.8): The spin Seebeck voltage was measured as a function of the magnetic field amplitude for an angle of $\alpha = 0°$ with the DC technique discussed in Sec. 5.3.1 for the current driven spin Seebeck effect. The heating power was $P = 35\,\mathrm{mW}$. In large magnetic fields, the spin Seebeck voltage is constant as a function of the magnetic field amplitude.

The spin Seebeck effect as a function of the magnetic field amplitude was already discussed in Sec. 5.3.2. Here, the same setup is used to perform spin Seebeck effect measurements in large magnetic fields. The results are shown in Fig. 5.11

for a heating power of $P = 35\,\mathrm{mW}$ and magnetic fields up to $\mu_0 H = 7\,\mathrm{T}$. For magnetic fields above $\mu_0 H = 1\,\mathrm{T}$, the generated spin Seebeck voltage is constant with $V_{\mathrm{iSSE}} \approx 1.2\,\mu\mathrm{V}$. Only in small fields, peaks in the spin Seebeck signal are visible, which can be explained by Oersted fields, as discussed in Sec. 5.3.6
Recently Kikkawa *et al.* [47] published data, which show a decrease of the spin Seebeck voltage in fields larger than $\mu_0 H = 1\,\mathrm{T}$. This decrease is explained by a gap in the magnon spectrum, which is induced by the large external magnetic field. It might be possible to explain the contradiction between the data presented in this thesis (Fig. 5.11) and the results by Kikkawa *et al.* by different thicknesses of the YIG film[6]. However, so far the spin Seebeck effect in high magnetic fields as a function of the YIG thickness was not discussed in literature.
On the other hand it was observed in ferromagnetic resonance experiments, that magnon decay processes, leading to an enhancement of the spin current, are suppressed in thin samples, smaller as $1\,\mu\mathrm{m}$ and magnetic fields larger as $60\,\mathrm{mT}$ [13, 55]. Of course, these results can not be compared directly to spin Seebeck experiments, since only the uniform magnetic precession mode was investigated. In Ch. 4 of this thesis, it was argued, that small wavenumber magnons do not contribute significantly to the spin Seebeck effect. However, the aforementioned publications do illustrate, that the spin currents can indeed be influenced by magnetic fields and the thickness of the YIG film.

[6]The YIG films used by Kikkawa *et al.* have a thickness of 1 mm.

5.4 Conclusions

In this chapter, a new setup for measurements of the spin Seebeck effect was presented. Here, instead of using some form of external heater (laser, Peltier element, resistive heater), the Pt layer of a YIG/Pt hybrid structure itself is used as a resistive heater. All signals, measured with this technique are superimposed by voltages due to resistive effects. However, it was shown that it is possible to separate thermal voltages and resistive voltages by adding the voltages, measured for different current directions or by using AC detection techniques.
Measurements of the spin Seebeck voltages as a function of the magnetic field amplitude (Sec. 5.3.2) and orientation (Sec. 5.3.1) were performed with the new setup. The results are qualitatively in agreement with recent publications on the spin Seebeck effect [97, 103]. Further, obtained spin Seebeck voltages are compared to spin Seebeck voltages generated with laser heating on the same sample. The results of both techniques do agree quantitatively. In Sec. 5.3.3 the spin Seebeck voltage was found to be proportional to the power, dissipated in the platinum layer as expected for a thermal effect.
Since the current driven spin Seebeck measurement is an on chip technique, it is possible to perform temperature dependent measurements, using standard magnet cryostats (Sec. 5.3.4). The spin Seebeck voltage did show a minimum at temperatures below $T = 50\,\mathrm{K}$ and an enhancement at very low temperatures. For temperatures above $T = 50\,\mathrm{K}$, the measurements agree with the theory put forward by Rezende *et al.* [74]. No phonon drag peak could be observed [1, 100]. An enhancement of the spin Seebeck voltage at low temperatures was not reported in literature so far. The magnetic proximity effect in platinum might contribute to this enhancement at very low temperatures. At room temperature, similar samples did not show proximity induced moments in the platinum [29, 30]. However, an enhancement of the proximity effect at low temperatures was reported in literature [56, 58]. In addition to DC measurements, AC experiments were performed and found to yield the same results, however, with much higher accuracy and reduced measurement time, as quantified in Sec. 5.3.5.
Rotations of the magnetic field orientation in small magnetic fields were discussed in Sec. 5.3.6. The obtained results did differ significantly from rotations in large magnetic fields. It was possible, to explain these difference with Oersted fields,

induced by the driving current. The model is consistent with expected values of the spin Hall magneto resistance and spin Seebeck effect, obtained in independent measurements.
Finally, the spin Seebeck effect was investigated in large magnetic fields (Sec. 5.3.7). The spin Seebeck voltage stayed constant up to $\mu_0 H_{\mathrm{ex}} = 7\,\mathrm{T}$. Measurements, performed by Kikkawa *et al.* [47] did show a decrease of the spin Seebeck voltage in the same measurement range. It might be possible to explain the contradicting results by a different thickness of the YIG layers, used in both experiments [13, 55].
Overall, the current driven spin Seebeck effect provides a simple approach for measurements of the spin Seebeck effect in YIG/Pt structures. Further, this approach allows measurements in a cryostat. However, one has to take care since additional effects may be induced by the driving currents, such as magneto resistive effects.

6 Summary and outlook

The spin Seebeck effect is driven by a temperature imbalance between magnons in a ferromagnet and electrons in an attached metal. However, the microscopic mechanisms leading to such an imbalance are still under discussion. Different, often contradicting, theories have been published in literature [3, 14, 37, 74, 94, 95, 106]. The experiments, performed within the framework of this thesis, aimed at uncovering these underlying mechanisms. While the time resolved SSE experiments in Ch. 4 could not directly prove one of the existing theories, it was shown that the commonly conducted macro-spin approximation [106] does not hold in the spin Seebeck effect.

The second part of this thesis introduced a new technique to measure the SSE which was developed at the WMI in collaboration with Erich Dobler [20]. Here, the platinum layer in YIG/Pt structures is used for on chip heating and thus acts not only as spin current detector but also as a heat source. This technique reduces the effort usually required for spin Seebeck effect experiments drastically. Therefore it is conducive to the field of spin caloritronics, since it allows to perform spin Seebeck effect measurements under conditions, not easily accessible with established spin Seebeck effect setups, such as low temperatures or high magnetic fields. In fact, current research at the WMI on the SSE was only made possible by this new technique.

6.1 Summary

In Ch. 4 of this thesis, the results of transient spin Seebeck effect measurements are reported. A setup, developed by Mathias Weiler und Michael Schreier at the WMI [82, 103], was refined to allow for time resolved spin Seebeck effect experiments.

As it is common for high frequency measurements, the transient spin Seebeck voltages were superimposed by resonances, which did not stem from the laser irradiation (Sec. 4.3.3). By separating even and odd contributions of the measured voltage with respect to the magnetic field, as presented in Sec. 4.3.1, these resonances could, however, be removed from the spin Seebeck voltages.
Building on the work by Kathrin Ganzhorn [28] the accessible frequency range could be extended to values typical for the interaction between magnons and phonons (Sec. 4.3.2). Electrical cutoffs of the spin Seebeck voltage were found in the low MHz regime, however, it could be shown that these were merely features of the experimental setup rather than due to any mechanism intrinsic to the spin Seebeck effect. From these measurements it is already possible to conclude, that all time constants, relevant for the spin Seebeck effect, are shorter than $\tau = 1/(2\pi f_{\mathrm{mod}}) = 3\,\mathrm{ns}$.
This was confirmed on another set of experiments in the time domain (Sec. 4.3.4) which showed the analogue behavior that could be modeled as being caused by the RC-lowpass limit of the setup.
In contrast to the original assumption by Xiao *et al.* the results presented in this thesis show, that the uniform magnetization precession mode is not important for the spin Seeebck effect (Sec. 4.4). This also calls into question the conclusion made by Agrawal *et al.* [5] in a recent plication that much longer (by at least an order of magnitude) time constants are intrinsic to the SSE.
The results obtained in this thesis are in good agreement with newer spin Seebeck effect theories which assume, that the spin Seebeck effect is driven by thermally distributed magnons [74, 94].

In Ch. 5, the current driven spin Seebeck effect was introduced. This is a new technique to measure spin Seebeck effect, which was developed at the WMI in collaboration with Erich Dobler [20]. The platinum layer in the YIG/Pt structure, originally only used for spin current detection, is here simultaneously used for on chip heating (Sec. 5.2). Since the platinum layer is uniformly heated it can, in contrast to the laser heating technique, also be used for thermometry (Sec. 5.2.1). Measurements of the current driven spin Seebeck effect are not straight forward, since the spin Seebeck voltage is superimposed by other signals. To recover the spin Seebeck signal, two approaches are presented: The voltage is measured for different current directions and added afterwards (Sec. 5.3.1) or the second harmonic voltage is recorded with a lock-in amplifier (Sec. 5.3.5). The results, obtained with different measurement approaches, are consistent.

By performing the measurements as a function of the external magnetic field orientation (Sec. 5.3.2) and the heating power (Sec. 5.3.3), it was possible to confirm, that the voltages are indeed caused by the spin Seebeck effect.

The advantage of the current driven spin Seeebeck effect is that measurements can be performed in standard magneto-transport setups rather than requiring specific devices and/or detection electronics. Therefore temperature dependent measurements in a ^{4}He magnet cryostat were conducted in this thesis (Sec. 5.3.4). While it was possible to reproduce the drop in the observed SSE voltage towards small temperatures reported in literature [74], it was found that the SSE voltage increases again at very low ($< 20\,\mathrm{K}$) temperatures. This behavior had not been reported before. In Sec. 5.3.4 it was argued, that the magnetic proximity effect in platinum [58] might contribute the observed voltage increase at low temperatures.

Finally, the spin Seebeck effect was measured in large and small magnetic fields. While the spin Seebeck effect in large fields stays constant as expected, unexpected features were observed in small fields. These additional features could successfully be modeled as being caused by stray Oersted fields.

In conclusion, a new technique for spin Seebeck effect measurements was introduced which made many experiments, not accessible to the WMI before, possible.

In the introduction of this thesis, it was stated, that spin caloritronics is a controversial topic with many unanswered questions. This thesis provides valuable results for both the theoretical modeling of the spin Seebeck effect, as well as presenting a new tool for further investigations.

6.2 Outlook

In Ch. 4, transient spin Seebeck effect measurements were performed. The frequency range up to $f_{\mathrm{mod}} = 50\,\mathrm{MHz}$ was explored, mostly limited by the measurement electronics. The range of the lock-in amplifier was 50 MHz and the digitizing card provided a sample rate of 200Msamples/s. Also the laser used in the experiments can not be modulated with more than $f_{\mathrm{mod}} = 200\,\mathrm{MHz}$. However, by using an electro-optical modulator for the laser intensity modulation and a high speed oscilloscope for data acquisition, it would be possible to measured spin Seebeck voltages in a higher frequency range. Consequently, it might be possible, to find cutoffs, intrinsic to spin Seebeck effect and thus gain better insight in the mechanisms, underlying the spin Seebeck effect.
As already mentioned in the introduction of this thesis, spin Seebeck effect and anomalous Nernst effect can not be distinguished a priori in conducting ferromagnets. Further, the anomalous Nernst effect might also be important in YIG/Pt samples, since platinum eventually could get proximity polarized[1]. The underlying physics of the anomalous Nernst effect is different from the spin Seebeck effect. Additional relaxation channels due to electron-magnon interaction exist. Consequently time constants, such as the magnon-phonon interaction time, might not play a role for the anomalous Nernst effect. Therefore it could be possible to distinguish both effects by time resolved measurements and thus determine the contribution of the anomalous Nernst effect in YIG/Pt samples as well as in ferromagnet/Pt samples unambiguously.

The current driven spin Seebeck effect is introduced in Ch. 5. One advantage is that the platinum layer can be used for thermometry. While this allowed to connect the observed voltages with a temperature increase in the Pt layer, the absolute value of the gradient across the interface can still only be approximated. However, if a sample with an additional Pt layer below the YIG could be produced this information could easily be obtained. Unfortunately, the fabrication of a Pt/YIG/Pt structure is challenging, since YIG does not grow single crystalline on platinum.

[1]This topic is still controversially discussed in literature [29, 30, 38, 47, 58]

At low temperatures, an increase in spin Seebeck voltage was clearly observed. In spin Seebeck theories, this increase was not reported yet. For further investigation it would be interesting, to measure the spin Seebeck effect at even lower temperatures. A ^{3}He cryostate would be needed for this purpose.
It was mentioned, that the anomalous Nernst effect might be an issue in a YIG/Pt structure. Therefore it could be interesting to measure the current driven spin Seebeck effect in YIG/Au samples. Here, the proximity effect can be excluded, because gold is diamagnetic. Since it is reported, that the proximity effect is enhanced at low temperatures, it is especially interesting, to measure the temperature dependence of the spin Seebeck effect in YIG/Au as a function of temperature.
In literature, a decrease in the spin Seebeck voltage in high magnetic fields was observed [47], which could not be reproduced with the current driven spin Seebeck effect. To rule out any attenuation of the spin Seebeck effect in high magnetic fields, it might be worth the measure the spin Seebeck effect in very high fields. The WMI currently possesses a magnet cryostat with the ability to produce magnetic fields up to 17 T. However, it is not clear, whether field amplitudes of 17 T are enough to observe an attenuation of the spin Seebeck voltage, since the high field dependence of the spin Seebeck effect was not addressed in literature so far.
Spin orbit torque and spin transfer torque effects gained great interest recently, especially because they allow to switch the magnetization of magnetic layers without application of external magnetic fields. However, so far spin torque effects have not been reported in literature on ferromagnetic insulator structures but only in ferromagnetic metal structures [25, 26]. The measurements, reported in Sec. 5.3.6 could be explained by Oersted fields. If samples with thinner YIG layer will be investigated, it might be possible to observe also spin torque effects in similar experiments. Since these effects are especially important for the computer industry, it would be of great interest, the explore this in more detail.
Finally it is possible, to combine time resolved measurements, reported in Ch. 4 of this thesis with the current driven spin Seebeck effect, introduced in Ch. 5. To carry out this experiments, a microwave current source has to be used. Further, it is important to take care of impedance matching. Since no laser with high modulation frequencies is necessary, this approach might be easier to implement.

Bibliography

[1] H. Adachi, K. Uchida, E. Saitoh, J. Ohe, S. Takahashi, and S. Maekawa. Gigantic enhancement of spin Seebeck effect by phonon drag. *Applied Physics Letters*, 97(25):252506, 2010. URL http://link.aip.org/link/APPLAB/v97/i25/p252506/s1&Agg=doi.

[2] H. Adachi, J. Ohe, S. Takahashi, and S. Maekawa. Linear-response theory of spin Seebeck effect in ferromagnetic insulators. *Physical Review B*, 83(9):094410, Mar. 2011. URL http://link.aps.org/doi/10.1103/PhysRevB.83.094410.

[3] H. Adachi, K. Uchida, E. Saitoh, and S. Maekawa. Theory of the spin Seebeck effect. *Reports on Progress in Physics*, 76(3):36501, 2013. URL http://stacks.iop.org/0034-4885/76/i=3/a=036501.

[4] M. Agrawal, V. I. Vasyuchka, A. A. Serga, A. D. Karenowska, G. A. Melkov, and B. Hillebrands. Direct Measurement of Magnon Temperature: New Insight into Magnon-Phonon Coupling in Magnetic Insulators. *Physical Review Letters*, 111(10), Sept. 2013. URL http://journals.aps.org/prl/abstract/10.1103/PhysRevLett.111.107204.

[5] M. Agrawal, V. I. Vasyuchka, A. A. Serga, A. Kirihara, P. Pirro, T. Langner, M. B. Jungfleisch, A. V. Chumak, E. T. Papaioannou, and B. Hillebrands. Sub-microsecond fast temporal evolution of the spin Seebeck effect. *ArXiv e-prints*, 1309.2164, Sept. 2013. URL http://arxiv.org/abs/1309.2164.

[6] M. Althammer, S. Meyer, H. Nakayama, M. Schreier, S. Altmannshofer, M. Weiler, H. Huebl, S. Geprägs, M. Opel, R. Gross, D. Meier, C. Klewe, T. Kuschel, J.-M. Schmalhorst, G. Reiss, L. Shen, A. Gupta, Y.-T. Chen, G. E. W. Bauer, E. Saitoh, and S. T. B. Goennenwein. Quantitative

study of the spin Hall magnetoresistance in ferromagnetic insulator/normal metal hybrids. *Physical Review B*, 87(22):224401, June 2013. URL http://link.aps.org/doi/10.1103/PhysRevB.87.224401.

[7] Z. An, F. Q. Liu, Y. Lin, and C. Liu. The universal definition of spin current. *Scientific Reports*, 2, May 2012. URL http://dx.doi.org/10.1038/srep00388.

[8] Axon. Coaxial Cables, 2012. URL www.axon-cable.com/publications/Coaxial-cables.pdf.

[9] G. E. W. Bauer, E. Saitoh, and B. J. van Wees. Spin caloritronics. *Nature Materials*, 11(5):391–399, May 2012. URL http://dx.doi.org/10.1038/nmat3301.

[10] S. Blundell. *Magnetism in Condensed Matter*. Oxford Master Series in Condensed Matter Physics. OUP Oxford, 2001. ISBN 9780198505914.

[11] Y.-T. Chen, S. Takahashi, H. Nakayama, M. Althammer, S. T. B. Goennenwein, E. Saitoh, and G. E. W. Bauer. Theory of spin Hall magnetoresistance. *Physical Review B*, 87(14):144411, Apr. 2013. URL http://link.aps.org/doi/10.1103/PhysRevB.87.144411.

[12] V. Cherepanov, I. Kolokolov, and V. L'vov. The saga of YIG: Spectra, thermodynamics, interaction and relaxation of magnons in a complex magnet. *Physics Reports*, 229:81–144, 1993. URL http://lvov.weizmann.ac.il/Texts-Online/012_Phys-Reps_Saga-IYG.pdf.

[13] A. L. Chernyshev. Field dependence of magnon decay in yttrium iron garnet thin films. *Physical Review B*, 86(6):60401, Aug. 2012. URL http://link.aps.org/doi/10.1103/PhysRevB.86.060401.

[14] L. Chotorlishvili, Z. Toklikishvili, V. K. Dugaev, J. Barnaś, S. Trimper, and J. Berakdar. Fokker-Planck approach to the theory of the magnon-driven spin Seebeck effect. *Physical Review B*, 88(14):144429, 2013. URL http://link.aps.org/doi/10.1103/PhysRevB.88.144429.

[15] R. J. Corruccini. Interpolation of Platinum Resistance Thermometers, 20° to 273.15°K. *Review of Scientific Instruments*, 31(6), 1960. URL http://scitation.aip.org/content/aip/journal/rsi/31/6/10.1063/1.1931274.

[16] R. O. Cunha, E. Padrón-Hernández, A. Azevedo, and S. M. Rezende. Controlling the relaxation of propagating spin waves in yttrium iron garnet/Pt bilayers with thermal gradients. *Physical Review B*, 87(18):184401, May 2013. URL http://link.aps.org/doi/10.1103/PhysRevB.87.184401.

[17] F. D. Czeschka. *Spin Currents in Metallic Nanostructures*. Phd thesis, Technical University Munich, 2011. URL http://www.wmi.badw.de/publications/theses/Czeschka_Doktorarbeit_2011.pdf.

[18] G. L. da Silva, L. H. Vilela-Leão, S. M. Rezende, and A. Azevedo. Spin current injection by spin Seebeck and spin pumping effects in yttrium iron garnet/Pt structures. *Journal of Applied Physics*, 111(7), 2012. URL http://scitation.aip.org/content/aip/journal/jap/111/7/10.1063/1.3676239.

[19] S. O. Demokritov, V. E. Demidov, O. Dzyapko, G. A. Melkov, A. A. Serga, B. Hillebrands, and A. N. Slavin. Bose-Einstein condensation of quasi-equilibrium magnons at room temperature under pumping. *Nature*, 443(7110):430–433, Sept. 2006. URL http://dx.doi.org/10.1038/nature05117.

[20] E. Dobler. *Joule Heating Induced Spin-Seebeck Effect*. Bachelor thesis, Technical University Munich, 2013.

[21] R. L. Douglass. Heat Transport by Spin Waves in Yttrium Iron Garnet. *Physical Review*, 129(3):1132–1135, Feb. 1963. URL http://link.aps.org/doi/10.1103/PhysRev.129.1132.

[22] L. Dreher, M. Weiler, M. Pernpeintner, H. Huebl, R. Gross, M. S. Brandt, and S. T. B. Goennenwein. Surface acoustic wave driven ferromagnetic resonance in nickel thin films: Theory and experiment. *Physical Review B*, 86(13):

134415, Oct. 2012. URL http://link.aps.org/doi/10.1103/PhysRevB.86.134415.

[23] M. S. V. Dusen. Platinum-Resistance Thermometry at Low Ttemperatures. *Journal of the American Chemical Society*, 47(2):326–332, Feb. 1925. URL http://dx.doi.org/10.1021/ja01679a007http://pubs.acs.org/doi/abs/10.1021/ja01679a007.

[24] M. I. D'yakonov and V. I. Perel'. Possibility of orienting electron spins with current. *JETP Letters*, 13(11):467–469, 1971. URL http://www.jetpletters.ac.ru/ps/1587/article_24366.shtml.

[25] X. Fan, J. Wu, Y. Chen, M. J. Jerry, H. Zhang, and J. Q. Xiao. Observation of the nonlocal spin-orbital effective field. *Nature Communications*, 4:1799, Apr. 2013. URL http://dx.doi.org/10.1038/ncomms2709.

[26] X. Fan, H. Celik, J. Wu, C. Ni, K.-J. Lee, V. O. Lorenz, and J. Q. Xiao. Quantifying interface and bulk contributions to spin–orbit torque in magnetic bilayers. *Nature Communications*, 5, Jan. 2014. URL http://dx.doi.org/10.1038/ncomms4042.

[27] J. Flipse, F. K. Dejene, D. Wagenaar, G. E. W. Bauer, J. Ben Youssef, and B. J. van Wees. Observation of the spin Peltier effect. *ArXiv e-prints*, 1311.4772, Nov. 2013. URL http://arxiv.org/abs/1311.4772.

[28] K. Ganzhorn. *Spatially and Temporally Resolved Spin Seebeck Experiments*. Bachelor thesis, Technical University Munich, 2012. URL http://www.wmi.badw.de/publications/theses/Ganzhorn,Kathrin_Bachelorarbeit_2012.pdf.

[29] S. Gepraegs, S. Meyer, S. Altmannshofer, M. Opel, F. Wilhelm, A. Rogalev, R. Gross, and S. T. B. Goennenwein. Investigation of induced Pt magnetic polarization in Pt/Y3Fe5O12 bilayers. *Applied Physics Letters*, 101 (26):262407, 2012. URL http://link.aip.org/link/APPLAB/v101/i26/p262407/s1&Agg=doi.

[30] S. Geprägs, S. T. B. Goennenwein, M. Schneider, F. Wilhelm, K. Ollefs, A. Rogalev, M. Opel, and R. Gross. Comment on "Pt magnetic polarization on Y3Fe5O12 and magnetotransport characteristics". *ArXiv e-prints*, 1307.4869, 2013. URL http://arxiv.org/abs/1307.4869.

[31] S. T. B. Goennenwein and G. E. W. Bauer. Spin caloritronics: Electron spins blow hot and cold. *Nature Materials*, 7(3):145–147, Mar. 2012. URL http://dx.doi.org/10.1038/nnano.2012.26.

[32] R. Gross and A. Marx. *Festkörperphysik*. Oldenbourg Wissenschaftsverlag, 2012. ISBN 9783486712940.

[33] G. C. L. Harper and A. F. A. Resistance-temperature relationship of platinum at low temperatures and its influence on precision thermometry. *British Journal of Applied Physics*, 11(5):205, 1960. URL http://stacks.iop.org/0508-3443/11/i=5/a=308.

[34] E. Hecht. *Optics*. Pearson Education, 2008. ISBN 9788131718070.

[35] R. Hertel. Oersted fields and current density profiles in spin-torque driven magnetization dynamics – Finite element modelling of realistic geometries. *ArXiv e-prints*, 0804.4010, Apr. 2008. URL http://arxiv.org/abs/0804.4010.

[36] J. E. Hirsch. Spin Hall Effect. *Physical Review Letters*, 83(9):1834–1837, Aug. 1999. URL http://link.aps.org/doi/10.1103/PhysRevLett.83.1834.

[37] S. Hoffman, K. Sato, and Y. Tserkovnyak. Landau-Lifshitz theory of the longitudinal spin Seebeck effect. *Physical Review B*, 88(6):64408, Aug. 2013. URL http://link.aps.org/doi/10.1103/PhysRevB.88.064408.

[38] S. Y. Huang, X. Fan, D. Qu, Y. P. Chen, W. G. Wang, J. Wu, T. Y. Chen, J. Q. Xiao, and C. L. Chien. Transport Magnetic Proximity Effects in Platinum. *Physical Review Letters*, 109(10):107204, Sept. 2012. URL http://link.aps.org/doi/10.1103/PhysRevLett.109.107204.

[39] S. Hunklinger. *Festkörperphysik*. Oldenbourg, 2007. ISBN 9783486575620.

[40] C. M. Jaworski, J. Yang, S. Mack, D. D. Awschalom, J. P. Heremans, and R. C. Myers. Observation of the spin-Seebeck effect in a ferromagnetic semiconductor. *Nature materials*, 9(11):898–903, Nov. 2010. URL http://www.ncbi.nlm.nih.gov/pubmed/20871608.

[41] C. M. Jaworski, J. Yang, S. Mack, D. D. Awschalom, R. C. Myers, and J. P. Heremans. Spin-Seebeck Effect: A Phonon Driven Spin Distribution. *Physical Review Letters*, 106(18):186601, May 2011. URL http://link.aps.org/doi/10.1103/PhysRevLett.106.186601.

[42] M. Johnson and R. H. Silsbee. Thermodynamic analysis of interfacial transport and of the thermomagnetoelectric system. *Physical Review B*, 35(10):4959–4972, Apr. 1987. URL http://link.aps.org/doi/10.1103/PhysRevB.35.4959.

[43] Y. Kajiwara, K. Harii, S. Takahashi, J. Ohe, K. Uchida, M. Mizuguchi, H. Umezawa, H. Kawai, K. Ando, K. Takanashi, S. Maekawa, and E. Saitoh. Transmission of electrical signals by spin-wave interconversion in a magnetic insulator. *Nature*, 464(7286):262–266, Mar. 2010. URL http://dx.doi.org/10.1038/nature08876.

[44] Y. Kajiwara, S. Takahashi, S. Maekawa, and E. Saitoh. Detection of Spin-Wave Spin Current in a Magnetic Insulator. *Magnetics, IEEE Transactions on*, 47(6):1591–1594, 2011. URL http://ieeexplore.ieee.org/iel5/20/5772170/05772199.pdf?arnumber=5772199.

[45] Y. K. Kato, R. C. Myers, A. C. Gossard, and D. D. Awschalom. Observation of the Spin Hall Effect in Semiconductors. *Science*, 306(5703):1910–1913, Dec. 2004. URL http://www.sciencemag.org/content/306/5703/1910.abstract.

[46] A. Kehlberger, R. Röser, G. Jakob, U. Ritzmann, D. Hinzke, U. Nowak, M. C. Onbasli, D. H. Kim, C. A. Ross, M. B. Jungfleisch, B. Hillebrands, and M. Kläui. Determination of the origin of the spin Seebeck effect - bulk vs. interface effects. *ArXiv e-prints*, 1306.0784, 2013. URL http://arxiv.org/abs/1306.0784.

[47] T. Kikkawa, K. Uchida, S. Daimon, Y. Shiomi, H. Adachi, Z. Qiu, D. Hou, X.-F. Jin, S. Maekawa, and E. Saitoh. Separation of longitudinal spin Seebeck effect from anomalous Nernst effect: Determination of origin of transverse thermoelectric voltage in metal/insulator junctions. *Physical Review B*, 88(21):214403, Dec. 2013. URL http://link.aps.org/doi/10.1103/PhysRevB.88.214403.

[48] T. Kikkawa, K. Uchida, Y. Shiomi, Z. Qiu, D. Hou, D. Tian, H. Nakayama, X.-F. Jin, and E. Saitoh. Longitudinal Spin Seebeck Effect Free from the Proximity Nernst Effect. *Physical Review Letters*, 110(6):067207, Feb. 2013. URL http://link.aps.org/doi/10.1103/PhysRevLett.110.067207.

[49] T. Kimura, Y. Otani, T. Sato, S. Takahashi, and S. Maekawa. Room-Temperature Reversible Spin Hall Effect. *Physical Review Letters*, 98(15):156601, Apr. 2007. URL http://link.aps.org/doi/10.1103/PhysRevLett.98.156601.

[50] A. Kirihara, K.-i. Uchida, Y. Kajiwara, M. Ishida, Y. Nakamura, T. Manako, E. Saitoh, and S. Yorozu. Spin-current-driven thermoelectric coating. *Nature Materials*, 11(8):686–689, Aug. 2012. URL http://dx.doi.org/10.1038/nmat3360.

[51] C. Kittel and E. Abrahams. Relaxation Process in Ferromagnetism. *Reviews of Modern Physics*, 25(1):233–238, Jan. 1953. URL http://link.aps.org/doi/10.1103/RevModPhys.25.233.

[52] C. Kittel and S. Hunklinger. *Einführung in die Festkörperphysik*. Einf{ü}hrung in die Festk{ö}rperphysik. Oldenbourg Wissenschaftsverlag, 2013. ISBN 9783486597554.

[53] J. Kondo. Resistance Minimum in Dilute Magnetic Alloys. *Progress of Theoretical Physics*, 32(1):37–49, July 1964. URL http://ptp.oxfordjournals.org/content/32/1/37.abstract.

[54] B. Krüger. *Current-Driven Magnetization Dynamics: Analytical Modeling and Numerical Simulation*. Phd thesis, University Hamburg,

2011. URL ediss.sub.uni-hamburg.de/volltexte/2012/5887/pdf/Dissertation.pdf.

[55] H. Kurebayashi, O. Dzyapko, V. E. Demidov, D. Fang, A. J. Ferguson, and S. O. Demokritov. Controlled enhancement of spin-current emission by three-magnon splitting. *Nature Materials*, 10(9):660–664, Sept. 2011. URL http://dx.doi.org/10.1038/nmat3053.

[56] W. L. Lim, N. Ebrahim-Zadeh, J. C. Owens, H. G. E. Hentschel, and S. Urazhdin. Temperature-dependent proximity magnetism in Pt. *Applied Physics Letters*, 102(16), 2013. URL http://scitation.aip.org/content/aip/journal/apl/102/16/10.1063/1.4802954.

[57] Z. Lin, L. V. Zhigilei, and V. Celli. Electron-phonon coupling and electron heat capacity of metals under conditions of strong electron-phonon nonequilibrium. *Physical Review B*, 77(7):75133, Feb. 2008. URL http://link.aps.org/doi/10.1103/PhysRevB.77.075133.

[58] Y. M. Lu, Y. Choi, C. M. Ortega, X. M. Cheng, J. W. Cai, S. Y. Huang, L. Sun, and C. L. Chien. Pt Magnetic Polarization on Y3Fe5O12 and Magnetotransport Characteristics. *Physical Review Letters*, 110(14):147207, Apr. 2013. URL http://link.aps.org/doi/10.1103/PhysRevLett.110.147207.

[59] J. Lunze. *Regelungstechnik 1: Systemtheoretische Grundlagen, Analyse Und Entwurf Einschleifiger Regelungen*. Number Bd. 1 in Springer-Lehrbuch. Springer Berlin Heidelberg, 2012. ISBN 9783642295324.

[60] S. Maekawa, H. Adachi, K.-i. Uchida, J. Ieda, and E. Saitoh. Spin Current: Experimental and Theoretical Aspects. *Journal of the Physical Society of Japan*, 82(10), 2013. URL http://journals.jps.jp/doi/abs/10.7566/JPSJ.82.102002.

[61] F. L. McCrackin and S. S. Chang. Simple calibration procedures for platinum resistance thermometers from 2.5 to 14 K. *Review of Scientific Instruments*, 46(5), 1975. URL http://scitation.aip.org/content/aip/journal/rsi/46/5/10.1063/1.1134255?crawler=true.

[62] D. Meier, T. Kuschel, L. Shen, A. Gupta, T. Kikkawa, K. Uchida, E. Saitoh, J.-M. Schmalhorst, and G. Reiss. Thermally driven spin and charge currents in thin NiFe2O4/Pt films. *Physical Review B*, 87(5):054421, Feb. 2013. URL http://link.aps.org/doi/10.1103/PhysRevB.87.054421.

[63] F. Meier and D. Loss. Magnetization Transport and Quantized Spin Conductance. *Physical Review Letters*, 90(16):167204, Apr. 2003. URL http://link.aps.org/doi/10.1103/PhysRevLett.90.167204.

[64] R. Metselaar and P. K. Larsen. High-temperature electrical properties of yttrium iron garnet under varying oxygen pressures. *Solid State Communications*, 15(2):291–294, July 1974. URL http://www.sciencedirect.com/science/article/pii/0038109874907601.

[65] S. Meyer, M. Althammer, S. Geprägs, M. Opel, R. Gross, and S. T. B. Goennenwein. Temperature dependent spin transport properties of Platinum inferred from spin Hall magnetoresistance measurements. *ArXiv e-prints*, 1401.7787, 2014. URL http://arxiv.org/abs/1401.7787.

[66] S. Murakami, N. Nagaosa, and S.-C. Zhang. Dissipationless Quantum Spin Current at Room Temperature. *Science*, 301(5638):1348–1351, Sept. 2003. URL http://www.sciencemag.org/content/301/5638/1348.abstract.

[67] H. Nakayama, K. Ando, K. Harii, T. Yoshino, R. Takahashi, Y. Kajiwara, K. Uchida, Y. Fujikawa, and E. Saitoh. Geometry dependence on inverse spin Hall effect induced by spin pumping in Ni81Fe19/Pt films. *Physical Review B*, 85(14):144408, Apr. 2012. URL http://link.aps.org/doi/10.1103/PhysRevB.85.144408.

[68] H. Nakayama, M. Althammer, Y.-T. Chen, K. Uchida, Y. Kajiwara, D. Kikuchi, T. Ohtani, S. Geprägs, M. Opel, S. Takahashi, R. Gross, G. E. W. Bauer, S. T. B. Goennenwein, and E. Saitoh. Spin Hall Magnetoresistance Induced by a Nonequilibrium Proximity Effect. *Physical Review Letters*, 110(20):206601, May 2013. URL http://link.aps.org/doi/10.1103/PhysRevLett.110.206601.

[69] E. Padrón-Hernández, A. Azevedo, and S. M. Rezende. Amplification of Spin Waves by Thermal Spin-Transfer Torque. *Physical Review Letters*, 107(19):197203, Nov. 2011. URL http://link.aps.org/doi/10.1103/PhysRevLett.107.197203.

[70] D. B. Poker and C. E. Klabunde. Temperature dependence of electrical resistivity of vanadium, platinum, and copper. *Physical Review B*, 26(12):7012–7014, Dec. 1982. URL http://link.aps.org/doi/10.1103/PhysRevB.26.7012.

[71] D. Qu, S. Y. Huang, J. Hu, R. Wu, and C. L. Chien. Intrinsic Spin Seebeck Effect in Au/YIG. *Physical Review Letters*, 110(6):067206, Feb. 2013. URL http://link.aps.org/doi/10.1103/PhysRevLett.110.067206.

[72] R. Ramos, T. Kikkawa, K. Uchida, H. Adachi, I. Lucas, M. H. Aguirre, P. Algarabel, L. Morellon, S. Maekawa, E. Saitoh, and M. R. Ibarra. Observation of the spin Seebeck effect in epitaxial Fe3O4 thin films. *Applied Physics Letters*, 102(7):072413, 2013. URL http://link.aip.org/link/APPLAB/v102/i7/p072413/s1&Agg=doi.

[73] E. I. Rashba. Spin currents in thermodynamic equilibrium: The challenge of discerning transport currents. *Physical Review B*, 68(24):241315, Dec. 2003. URL http://link.aps.org/doi/10.1103/PhysRevB.68.241315.

[74] S. M. Rezende, R. L. Rodriguez-Suárez, R. O. Cunha, A. R. Rodrigues, F. L. A. Machado, G. A. Fonseca Guerra, J. C. Lopez Ortiz, and A. Azevedo. Magnon spin-current theory for the longitudinal spin-Seebeck effect. *Physical Review B*, 89(1):14416, Jan. 2014. URL http://link.aps.org/doi/10.1103/PhysRevB.89.014416.

[75] H.-C. Ri, F. Kober, R. Gross, R. P. Huebener, and A. Gupta. Seebeck effect in the mixed state of epitaxial YBa2Cu3O7. *Physical Review B*, 43(16):13739–13742, June 1991. URL http://link.aps.org/doi/10.1103/PhysRevB.43.13739.

[76] J. E. Rives, G. S. Dixon, and D. Walton. Effect of Magnons on Thermal Transport in Insulators. *Journal of Applied Physics*, 40(3),

1969. URL http://scitation.aip.org/content/aip/journal/jap/40/3/10.1063/1.1657761?crawler=true.

[77] N. Roschewsky, M. Schreier, A. Kamra, F. Schade, K. Ganzhorn, S. Meyer, H. Huebl, S. Geprägs, R. Gross, and S. T. B. Goennenwein. Time resolved spin Seebeck effect experiments as a probe of magnon-phonon thermalization time. *ArXiv e-prints*, 1309.3986, Sept. 2013. URL http://arxiv.org/abs/1309.3986.

[78] E. Saitoh, M. Ueda, H. Miyajima, and G. Tatara. Conversion of spin current into charge current at room temperature: Inverse spin-Hall effect. *Applied Physics Letters*, 88(18), 2006. URL http://scitation.aip.org/content/aip/journal/apl/88/18/10.1063/1.2199473.

[79] Samtec. 50 Ohm RG 178 Cable Assemblies, 2014. URL https://www.samtec.com/ftppub/pdf/RF178.PDF?

[80] D. J. Sanders and D. Walton. Effect of magnon-phonon thermal relaxation on heat transport by magnons. *Physical Review B*, 15(3):1489–1494, Feb. 1977. URL http://link.aps.org/doi/10.1103/PhysRevB.15.1489.

[81] M. Schmid, S. Srichandan, D. Meier, T. Kuschel, J.-M. Schmalhorst, M. Vogel, G. Reiss, C. Strunk, and C. H. Back. Transverse Spin Seebeck Effect versus Anomalous and Planar Nernst Effects in Permalloy Thin Films. *Physical Review Letters*, 111(18):187201, Oct. 2013. URL http://link.aps.org/doi/10.1103/PhysRevLett.111.187201.

[82] M. Schreier. *Spatially resolved spin Seebeck experiments*. Diploma thesis, Technical University Munich, 2012. URL http://www.wmi.badw.de/publications/theses/Schreier,Michael_Diplomarbeit_2012.pdf.

[83] M. Schreier, A. Kamra, M. Weiler, J. Xiao, G. E. W. Bauer, R. Gross, and S. T. B. Goennenwein. Magnon, phonon, and electron temperature profiles and the spin Seebeck effect in magnetic insulator/normal metal hybrid structures. *Physical Review B*, 88(9):94410, Sept. 2013. URL http://link.aps.org/doi/10.1103/PhysRevB.88.094410.

[84] M. Schreier, N. Roschewsky, E. Dobler, S. Meyer, H. Huebl, R. Gross, and S. T. B. Goennenwein. Current heating induced spin Seebeck effect. *Applied Physics Letters*, 103(24), 2013. URL http://scitation.aip.org/content/aip/journal/apl/103/24/10.1063/1.4839395.

[85] G. Scott, D. Lacklison, and J. Page. Absorption spectra of Y3Fe5O12 (YIG) and Y3Ga5O12: Fe3+. *Physical Review B*, 10(3):971–986, Aug. 1974. URL http://link.aps.org/doi/10.1103/PhysRevB.10.971.

[86] T. J. Seebeck and A. Oettingen. *Magnetische Polarisation der Metalle und Erze durch Temperatur-Differenz*. Ostwalds Klassiker der exakten Wissenschaften. W. Engelmann, 1895.

[87] J. Shi, K. Pettit, E. Kita, S. S. P. Parkin, R. Nakatani, and M. B. Salamon. Field-dependent thermoelectric power and thermal conductivity in multilayered and granular giant magnetoresistive systems. *Physical Review B*, 54 (21):15273–15283, Dec. 1996. URL http://link.aps.org/doi/10.1103/PhysRevB.54.15273.

[88] J. Shi, P. Zhang, D. Xiao, and Q. Niu. Proper Definition of Spin Current in Spin-Orbit Coupled Systems. *Physical Review Letters*, 96(7):76604, Feb. 2006. URL http://link.aps.org/doi/10.1103/PhysRevLett.96.076604.

[89] J. Sinova, D. Culcer, Q. Niu, N. A. Sinitsyn, T. Jungwirth, and A. H. MacDonald. Universal Intrinsic Spin Hall Effect. *Physical Review Letters*, 92(12):126603, Mar. 2004. URL http://link.aps.org/doi/10.1103/PhysRevLett.92.126603.

[90] E. G. Spencer and R. C. LeCraw. Ferromagnetic relaxation in yttrium-iron garnet and the relation to applications. *Proceedings of the IEE - Part B: Electronic and Communication Engineering*, 109(21):66–70, 1962. URL http://ieeexplore.ieee.org/xpls/abs_all.jsp?arnumber=5244818.

[91] Stanford Research Systems. Manual: SR830 DSP Lock-In Amplifier, 2011. URL www.thinksrs.com/downloads/PDFs/Manuals/SR830m.pdf?

[92] Q.-f. Sun and X. C. Xie. Definition of the spin current: The angular spin current and its physical consequences. *Physical Review B*, 72(24):245305, Dec. 2005. URL http://link.aps.org/doi/10.1103/PhysRevB.72.245305.

[93] Q.-f. Sun, X. C. Xie, and J. Wang. Persistent spin current in nanodevices and definition of the spin current. *Physical Review B*, 77(3):35327, Jan. 2008. URL http://link.aps.org/doi/10.1103/PhysRevB.77.035327.

[94] K. S. Tikhonov, J. Sinova, and A. M. Finkel'stein. Spectral non-uniform temperature and non-local heat transfer in the spin Seebeck effect. *Nature Communications*, 4, June 2013. URL http://dx.doi.org/10.1038/ncomms2945.

[95] Y. Tserkovnyak, A. Brataas, and G. Bauer. Spin pumping and magnetization dynamics in metallic multilayers. *Physical Review B*, 66(22):224403, Dec. 2002. URL http://link.aps.org/doi/10.1103/PhysRevB.66.224403.

[96] K. Uchida, S. Takahashi, K. Harii, J. Ieda, W. Koshibae, K. Ando, S. Maekawa, and E. Saitoh. Observation of the spin Seebeck effect. *Nature*, 455(7214):778–81, Oct. 2008. URL http://www.ncbi.nlm.nih.gov/pubmed/18843364.

[97] K. Uchida, H. Adachi, T. Ota, H. Nakayama, S. Maekawa, and E. Saitoh. Observation of longitudinal spin-Seebeck effect in magnetic insulators. *Applied Physics Letters*, 97(17):172505, 2010. URL http://link.aip.org/link/APPLAB/v97/i17/p172505/s1&Agg=doi.

[98] K. Uchida, J. Xiao, H. Adachi, J. Ohe, S. Takahashi, J. Ieda, T. Ota, Y. Kajiwara, H. Umezawa, H. Kawai, G. E. W. Bauer, S. Maekawa, and E. Saitoh. Spin Seebeck insulator. *Nature materials*, 9(11):894–7, Nov. 2010. URL http://www.ncbi.nlm.nih.gov/pubmed/20871606.

[99] K. Uchida, H. Adachi, T. An, T. Ota, M. Toda, B. Hillebrands, S. Maekawa, and E. Saitoh. Long-range spin Seebeck effect and acoustic spin pumping. *Nature materials*, 10(10):737–741, Oct. 2011. URL http://dx.doi.org/10.1038/nmat3099.

[100] K. Uchida, T. Ota, H. Adachi, J. Xiao, T. Nonaka, Y. Kajiwara, G. E. W. Bauer, S. Maekawa, and E. Saitoh. Thermal spin pumping and magnon-phonon-mediated spin-Seebeck effect. *Journal of Applied Physics*, 111 (10):103903, 2012. URL http://link.aip.org/link/JAPIAU/v111/i10/p103903/s1&Agg=doi.

[101] S. O. Valenzuela and M. Tinkham. Direct electronic measurement of the spin Hall effect. *Nature*, 442(7099):176–179, July 2006. URL http://dx.doi.org/10.1038/nature04937.

[102] M. Walter, J. Walowski, V. Zbarsky, M. Münzenberg, M. Schäfers, D. Ebke, G. Reiss, A. Thomas, P. Peretzki, M. Seibt, J. S. Moodera, M. Czerner, M. Bachmann, and C. Heiliger. Seebeck effect in magnetic tunnel junctions. *Nature materials*, 10(10):742–6, Oct. 2011. URL http://www.ncbi.nlm.nih.gov/pubmed/21785418.

[103] M. Weiler, M. Althammer, F. D. Czeschka, H. Huebl, M. S. Wagner, M. Opel, I.-M. Imort, G. Reiss, A. Thomas, R. Gross, and S. T. B. Goennenwein. Local Charge and Spin Currents in Magnetothermal Landscapes. *Physical Review Letters*, 108(10):106602, Mar. 2012. URL http://link.aps.org/doi/10.1103/PhysRevLett.108.106602.

[104] M. Weiler, H. Huebl, F. S. Goerg, F. D. Czeschka, R. Gross, and S. T. B. Goennenwein. Spin Pumping with Coherent Elastic Waves. *Physical Review Letters*, 108(17):176601, Apr. 2012. URL http://link.aps.org/doi/10.1103/PhysRevLett.108.176601.

[105] S. Wittekoek, T. J. A. Popma, J. M. Robertson, and P. F. Bongers. Magneto-optic spectra and the dielectric tensor elements of bismuth-substituted iron garnets at photon energies between 2.2-5.2 eV. *Physical Review B*, 12(7):2777–2788, Oct. 1975. URL http://link.aps.org/doi/10.1103/PhysRevB.12.2777.

[106] J. Xiao, G. E. W. Bauer, K. Uchida, E. Saitoh, and S. Maekawa. Theory of magnon-driven spin Seebeck effect. *Physical Review B*, 81(21):214418, June 2010. URL http://link.aps.org/doi/10.1103/PhysRevB.81.214418.

[107] P.-Q. J. Zhang, Y.-Q. Li, and Fu-Chun. SU (2) $\times$ U (1) unified theory for charge, orbit and spin currents. *Journal of Physics A: Mathematical and General*, 39(22):7115, 2006. URL http://stacks.iop.org/0305-4470/39/i=22/a=022.

[108] S. S. L. Zhang and S. Zhang. Spin convertance at magnetic interfaces. *Physical Review B*, 86(21):214424, Dec. 2012. URL http://link.aps.org/doi/10.1103/PhysRevB.86.214424.

[109] S. S. L. Zhang and S. Zhang. Magnon Mediated Electric Current Drag Across a Ferromagnetic Insulator Layer. *Physical Review Letters*, 109(9): 96603, Aug. 2012. URL http://link.aps.org/doi/10.1103/PhysRevLett.109.096603.

[110] X. Zhou, Z. Zhang, and C.-Z. Hu. Spin continuity equation and definition of spin current. *ArXiv e-prints*, 0904.3796, Apr. 2009. URL http://arxiv.org/abs/0904.3796.

Acknowledgements

I would like to thank all people who made this work possible and who played an indispensable role for the development if this thesis.

- *Prof. Dr. Rudolf Gross* for giving me the opportunity to write my Master thesis at the Walther-Meißner-Institute.
- *PD. Dr. Sebastian Goennenwein* for accepting me as a member in the *magnetism group*, for his scientific support during the last year and for sharing his contagious enthusiasm for research.
- *Michael Schreier*, who supervised my work, tough me to work independent, never got tired, answering my questions, and who is always open for scientific discussions.
- *Akashdeep Kamra*, for sharing his deep knowledge about physics, providing important theoretical insights, sharing his experiences, contributing to the good group culture so much and being a very good friend in all situations.
- *Dr. Hans Huebl* for contributing with vulnerable ideas to every discussion and every experiment.
- *Erich Dobler, Rasmus Hollaender, Stefan Klimesch and Friedrich Witek* for the good collaboration, the friendship, the good atmosphere at the WMI and of course for sharing the *Matrix*.
- *Yori Manzke* from the *PDI* in Berlin for the good collaboration.
- The whole *magnetism group*: *Kathrin Ganzhorn, Stephan Gepraegs, Johannes Lotze, Hannes Maier-Flaig, Sybille Meyer, Matthias Opel and Matthias Pernpeintner*, for good group culture like coffe hour, Bouldering or watching the PhD movie. Especially I want to thank the people who did spend a lot of time for the sample fabrication.

- The technical and administrate staff of the WMI, who provide the stage for all the research at the WMI.
- *Johannes Mendil*, with whom I shared every good and every bad experience inside and outside of physics and who is „sockifiziert“as well.
- My family, for unlimited support during my physics studies and my entire life, no matter where in the world I am. *Jümmers.*

Erklärung

Ich versichere, dass ich diese Masterarbeit selbstständig angefertigt, sowie alle Stellen, die wörtlich oder annähernd wörtlich aus Veröffentlichungen entnommen wurden, als solche kenntlich gemacht und nur die angegebenen Hilfsmittel verwendet habe. Die Arbeit hat in dieser Form keiner anderen Prüfungsinstitution vorgelegen.

München, den 18. März 2014

(Niklas Roschewsky)